UNIVERSIDADE FEDERAL DE SANTA CATARINA
CAMPUS FLORIANÓPOLIS
PROGRAMA DE PÓS-GRADUAÇÃO EM ENGENHARIA MECÂNICA

Edemar Morsch Filho

A Coupled Irradiance - Thermal 3D Numerical Framework for Simulation of CubeSats

Florianópolis

2021

Edemar Morsch Filho

A Coupled Irradiance - Thermal 3D Numerical Framework for Simulation of CubeSats

Tese submetida ao Programa de Pós-Graduação em Engenharia Mecânica da Universidade Federal de Santa Catarina para a obtenção do título de Doutor em Engenharia Mecânica.
Orientador: Prof. Vicente de Paulo Nicolau, Dr.
Coorientadores: Laio Oriel Seman, Dr.; Prof. Talita Sauter Possamai, Dr.

Florianópolis
2021

Ficha de identificação da obra elaborada pelo autor,
através do Programa de Geração Automática da Biblioteca Universitária da UFSC.

Morsch Filho, Edemar
A Coupled Irradiance – Thermal 3D Numerical Framework for Simulation of CubeSats / Edemar Morsch Filho ; orientador, Vicente Paulo Nicolau, coorientador, Laio Oriel Seman, coorientadora, Talita Sauter Possamai, 2021.
126 p.

Tese (doutorado) – Universidade Federal de Santa Catarina, Centro Tecnológico, Programa de Pós-Graduação em Engenharia Mecânica, Florianópolis, 2021.

Inclui referências.

1. Engenharia Mecânica. 2. CubeSat. 3. Numerical Simulation. 4. Thermal radiation. 5. Temperature. I. Paulo Nicolau, Vicente. II. Oriel Seman, Laio. III. Sauter Possamai, Talita IV. Universidade Federal de Santa Catarina. Programa de Pós-Graduação em Engenharia Mecânica. V. Título.

Edemar Morsch Filho

A Coupled Irradiance - Thermal 3D Numerical Framework for Simulation of CubeSats

O presente trabalho em nível de doutorado foi avaliado e aprovado por banca examinadora composta pelos seguintes membros:

Prof. Paulo Smith Schneider, Dr.
Universidade Federal do Rio Grande do Sul

Prof. Kleber Vieira de Paiva, Dr.
Universidade Federal de Santa Catarina

Prof. Eduardo Augusto Bezerra, Dr.
Universidade Federal de Santa Catarina

Certificamos que esta é a **versão original e final** do trabalho de conclusão que foi julgado adequado para obtenção do título de doutor em Engenharia Mecânica.

ICP-Edu
Documento assinado digitalmente
Paulo de Tarso Rocha de Mendonca
Data: 19/04/2021 15:17:51-0300
CPF: 149.822.691-49
Verifique as assinaturas em https://v.ufsc.br

Prof. Paulo de Tarso Rocha de Mendonça, Dr.
Coordenador do Programa

GOV.BR
Documento assinado digitalmente
Vicente de Paulo Nicolau
Data: 19/04/2021 14:25:40-0300
CPF: 252.055.529-72
Verifique as assinaturas em https://v.ufsc.br

Prof. Vicente de Paulo Nicolau, Dr.
Orientador

Florianópolis, 12 de Abril de 2021.

Dedico esta tese a minha família, em especial a minha sobrinha Paola.

AGRADECIMENTOS

A minha esposa Arline, que me acompanhou em todas as situações e não mediu esforços para concretizarmos juntos esta etapa.

Aos meus pais, Edemar e Eliete, que garantiram o necessário para que mais essa jornada fosse finalizada. Da mesma forma, a minha irmã Janine, meu cunhado William e a minha sobrinha Paola, pelo suporte durante todo este tempo.

Ao orientador Prof. Vicente P. Nicolau, que me acolheu desde o início do mestrado e sempre garantiu todas as condições para que eu pudesse explorar as diferentes oportunidades que surgiram ao longo dessa jornada, sempre me recebendo com atenção e uma conversa agradável.

Ao meu coorientador Laio O. Seman, que contribuiu em muito para o andamento desta tese, me trouxe uma visão importante de pesquisador, e me auxiliou em diversas questões além do doutorado.

A professora Talita Sauter Possamai, que me incentivou a iniciar a pós-graduação e apresentou os caminhos para chegar até aqui.

Aos membros do Laboratório SpaceLab, local onde muitas amizades foram iniciadas e que foi fundamental para os caminhos traçados desde o início do doutorado. Agradeço o Prof. Eduardo A. Bezerra, coordenador desse laboratório, que diariamente vive o desafio de desenvolver tecnologia espacial e contribui para o envolvimento dos alunos com esse setor inspirador.

Agradeço o professor Amir Oliveira, coordenador do laboratório LabCet, e todos os demais alunos deste lugar agradável onde passei boa parte da pós-graduação e sentirei falta.

Ao professor Kleber V. Paiva, profissional diferenciado que faz a diferença na vida dos alunos.

Aos integrantes do SC2C.Aero, em especial ao professor Victor J. De Negri pela oportunidade

Ao Edevaldo B. Reinaldo, grande pessoa que o LabTermo possui, sempre disposto a ter um papo descontraído.

Aos amigos, que não cito nominalmente, saibam que todos foram essenciais em mais esta etapa.

Ao CNPq pela bolsa de doutorado, item que foi essencial ao longo destes anos.

Por fim a UFSC, que viu entrar um aluno cotista de escola pública e depois de anos o devolve para a sociedade como doutor.

”Por que a água fervente amolece a cenoura e endure o ovo?
(Rubens Alves).

RESUMO

O advento dos satélites padronizados tipo CubeSat tem possibilitado que um crescente número de universidades e empresas ao redor do mundo adentrem em projetos no segmento espacial. Entre os diversos sub-sistemas que compõem um CubeSat existe o controle térmico, responsável por manter todos os outros sub-sistemas dentro de limites aceitáveis de temperatura. Um método amplamente empregado na avaliação desse sistema é a simulação numérica, tema central desta tese. Para compor a simulação da transferência de calor, dois modelos foram desenvolvidos: irradiância e térmico. Neste trabalho, a irradiância considera que as fontes de calor, dadas pela radiação solar, albedo e emissão da terra no infra-vermelho, dependem da dinâmica orbital, além da orientação e apontamento do satélite (atitude), o que permite avaliar os diversos cenários térmicos a serem enfrentados pelo satélite ao longo do seu ciclo de operação em órbita. O modelo térmico baseia-se no Método dos Volumes Finitos (Finite Volume Method - FVM) e utiliza a irradiância como condição de contorno nas superfícies externas do domínio. Para realizar o balanço de energia nas superfícies internas utiliza-se o método de Gebhart, assim como um modelo para determinação de superfícies obstrutoras acoplado ao cálculo dos fatores de forma entre as faces. Entre os casos simulados está a avaliação do impacto da transferência interna de calor por radiação, que em alguns exemplos disponíveis na literatura é desconsiderada. Três casos de troca interna são verificados por meio da emissividade (ε) das superfícies, e incluem o caso em que a emissividade é máxima de superfície negra ($\varepsilon = 1.0$), o caso sem radiação ($\varepsilon = 0.0$) e um caso intermediário ($\varepsilon = 0.5$). Os resultados, válidos para uma geometria de CubeSat 1U (10x10x10 cm), indicam que as perturbações orbitais são essenciais para a simulação da posição do satélite e, consequentemente, o campo de radiação atuando sobre ele. Em termos de temperatura, a inclusão da transferência de calor interna modifica o campo de temperatura e deve ser considerada nas simulações. Um comparativo entre os resultados obtidos por meio do FVM e uma formulação mais simples obtida pelo método dos nós (Lumped Paramether Method - LPM) é realizada, onde verifica-se que os níveis de temperatura entre eles pode ser compatível ao se controlar a resistência térmica do LPM, ainda que este último não forneça campos tridimensionais. Ao final da tese, duas outras aplicações são demonstradas com o uso dos modelos de irradiância e térmico propostos, o que inclui a integração de tubos de calor e gerador termoelétricos em missões CubeSat.

Palavras-chaves: CubeSat, Simulação Numérica, Método dos Volumes Finitos, Irradiância, Temperatura, Radiação Térmica, Método de Gebhart.

RESUMO EXPANDIDO

Introdução

Os custos e prazos reduzidos, quando comparado à missões de grande porte tradicionais, são características atrativas que impulsionam o setor espacial com estimativas de aproximadamente 2500 novos lançamentos até 2025, incluindo missões do tipo CubeSat. Entre os diversos sub-sistemas que compõem o CubeSat existe o controle térmico, responsável por manter todos os outros sub-sistemas dentro de limites aceitáveis de temperatura. O satélite em órbita sofre variações de temperatura ao longo do seu ciclo de vida de operação, que se relacionam com a sua dinâmica orbital, além da orientação e rotação do satélite (atitude). Estes parâmetros impactam a irradiância que atinge as superfícies do satélite e, por consequência, também influenciam a temperatura. Este trabalho se propõe a desenvolver uma simulação numérica baseada no Método dos Volumes Finitos para a transferência de calor em CubeSats, além do acoplamento de um modelo de irradiância que é regido pela mecânica orbital, perturbações de órbita e atitude do satélite. As condições de contorno nas superfícies externas do satélite são descritas por este modelo de irradiância, enquanto que nas superfícies internas é utilizado o Método de Gebhart para a transferência de calor por radiação.

Objetivos

O objetivo principal deste trabalho é projetar uma estrutura de simulação — integrando irradiância e modelos térmicos — para avaliar o comportamento térmico de CubeSats e apoiar missões futuras. Seguindo este objetivo principal, os objetivos específicos são: (a) Implementar e analisar um modelo de fluxo de irradiância considerando órbita, atitude e parâmetros de radiação ao longo do ciclo de vida do CubeSat; (b) Projetar e avaliar um modelo térmico de CubeSats - empregando o método de volumes finitos - com transferência interna de calor por radiação; (c) Integrar os modelos de irradiância e térmicos apresentados anteriormente, a fim de obter uma estrutura de simulação totalmente funcional para CubeSats e analisar o resultado resultante em cenários representativos.

Metodologia

O trabalho aqui desenvolvido busca resolver a transferência de calor em um CubeSat por meio da integração de um modelo de irradiância e um modelo térmico. A irradiância fornece as condições de contorno para as superfícies externas do problema, sendo que aspectos como mecânica orbital, perturbação de órbita e atitude do satélite fazem parte deste modelo, permitindo uma avaliação dos fluxos de calor ao longo de todo o ciclo de operação do satélite. O arrasto atmosférico e o gradiente de gravidade compõem o conjunto de perturbações de órbita, cujas influências são mais expressivas na variação da altitude e do ângulo β, respectivamente. Este ângulo é medido entre o plano orbital e o vetor sol, sendo uma métrica que rege a duração da passagem do satélite sob a sombra terrestre, ocasião em que o fluxo solar, principal fonte de calor, deixa de atingi-lo. A atitude rege as projeções das superfícies externas do satélite em relação as fontes de calor, reconhecidas como o fluxo solar, o albedo e a emissão da terra no infravermelho. O modelo térmico transiente e tridimensional é desenvolvido com base no Método dos Volumes Finitos, tendo o modelo de irradiância como condição de contorno nas superfícies externas do domínio e o Método de Gebhart como formulação para a troca de calor por radiação nas superfícies internas. O sombreamento entre os componentes no interior do satélite é estimado por meio de um algoritmo, cujas obstruções auxiliam no cálculo dos fatores de forma entre as superfícies. As condições de troca de calor por radiação no interior do satélite são avaliados em função da emissividade

(ε) dessas paredes, sendo verificado o caso sem radiação ($\varepsilon = 0.0$), o caso com máxima emissividade - superfícies negras ($\varepsilon = 1.0$) e um caso intermediário ($\varepsilon = 0.5$).

Resultados e Discussão

A dinâmica orbital e do satélite são parâmetros que permitem uma avaliação preliminar da radiação térmica sobre o CubeSat e seu respectivo comportamento térmico ao longo do ciclo de vida. O campo de temperatura sofre uma variação significativa ao longo de uma órbita, atingindo os menores níveis de temperatura sob a sombra terrestre e os maiores no último instante antes de adentrar no eclipse da terra. O gradiente espacial no satélite não é desprezível, sendo que para a geometria avaliada os pontos mais quentes e frios ocorrem no centro dos painéis solares. Os componentes internos também apresentam campos transientes e tridimensionais, mas com uma variação de menor magnitude. A inclusão da transferência interna de calor por radiação impacta na temperatura dos partes internas e externas do satélite, sendo que uma condição sem radiação ($\varepsilon = 0.0$) no interior do satélite eleva a sua temperatura máxima e reduz ainda mais a temperatura mínima. No outro extremo, a máxima troca de calor interno por radiação ocorre com $\varepsilon = 1.0$, e reduz os picos de temperatura nas partes externas em virtude de que nesta condição estes componentes conseguem trocar calor nas suas duas faces opostas externa e interna. Com o objetivo de estender a aplicabilidade do modelo proposto nesta tese, também são apresentados breves resultados acerca da integração de um tubo de calor entre dois painéis do CubeSat, além de um gerador termoelétrico na simulação. No caso do tubo de calor, o impacto na temperatura dos painéis em contato com ele é evidente, sendo um meio eficaz de transferir calor entre duas partes. Por outro lado, a análise do gerador termoelétrico mostrou ser inviável a obtenção de energia extra por meio deste dispositivo.

Considerações Finais

A inclusão de aspectos como dinâmica orbital e atitude do satélite compõem o modelo de irradiância que está integrado ao modelo térmico desta tese, e consiste numa ferramenta para avaliar aspectos relacionados à temperatura de um CubeSat ao longo do seu ciclo de vida em órbita. Com o objetivo de avaliar o comportamento térmico de uma típica missão CubeSat 1U, diferentes cenários de órbita, atitude e emissividade das superfícies interna do satélite são avaliados nesta tese por meio de um único modelo integrado. Em virtude do desenvolvimento obtido até aqui, os trabalhos futuros são no sentido de: (a) Reduzir o erro no cálculo de sombreamento das partes internas do satélite através do refinamento das superfícies parcialmente sombreadas; (b) Incluir na estrutura da simulação o calor dissipado pelos diversos componentes eletrônicos do CubeSat com base no seu perfil de execução de tarefas; (c) Utilizar a estrutura da simulação em conjunto com técnicas de controle térmico ativo e passivo compatíveis com missões CubeSat, a fim de avaliar o desempenho destas tecnologias.

Palavras-chaves: CubeSat, Simulação Numérica, Volumes Finitos, Irradiância, Temperatura, Radiação Térmica, Método de Gebhart.

ABSTRACT

The advent of standardized CubeSat satellites has enabled an increasing number of universities and companies worldwide to enter projects in the space segment. Among the various sub-systems that make up a CubeSat, thermal control is responsible for keeping all other sub-systems within acceptable temperature limits. A method widely used in evaluating this system is a numerical simulation, the central theme of this thesis. To compose the heat transfer's simulation, two models were developed: irradiance and thermal. In this work, irradiance considers that the heat sources, given by solar radiation, albedo, and infrared Earth emission, dependent on the orbital dynamics, in addition to the orientation and pointing of the satellite (attitude), which allows evaluating the different scenarios thermal elements to be faced by the satellite throughout its orbit operating cycle. The thermal model is based on the Finite Volume Method (FVM) and uses irradiance as a boundary condition on the domain's external surfaces. To perform the energy balance on the internal surfaces, the Gebhart method is used, and a model for determining obstructive surfaces coupled with the calculation of the view factors between the faces. Among the simulated cases is the evaluation of the impact of the internal heat transfer by radiation, which in some examples available in the literature is disregarded. Three cases of internal exchange are verified by means of the emissivity (ε) of the surfaces, and include the case in which the emissivity is the maximum black-body surface ($\varepsilon = 1.0$), the case without radiation ($\varepsilon = 0.0$) and an intermediate case ($\varepsilon = 0.5$). The results, valid for a geometry of CubeSat 1U (10x10x10 cm), indicate that the orbital disturbances are essential for the simulation of the satellite's position and, consequently, the radiation field acting on it. In terms of temperature, the inclusion of internal heat transfer changes the temperature field and must be considered in the simulations. A comparison between the results obtained using the FVM and a simpler formulation obtained by the method of nodes (Lumped Parameter Method - LPM) is carried out, where it is verified that the temperature levels between them can be compatible when controlling the thermal resistance of the LPM, even though the latter does not provide three-dimensional fields. At the end of the thesis, two other applications are demonstrated using the proposed irradiance and thermal models, including the integration of heat pipes and thermoelectric generators in CubeSat missions.

Key-words: CubeSat, Finite Volume Method, Irradiance, Temperature, Thermal Radiation, Gebhart Method.

LIST OF FIGURES

LIST OF TABLES

LIST OF ABBREVIATIONS AND ACRONYMS

AU	Astronomical Unit
COE	Classical Orbital Element
COTS	Commercial-Off-The-Shelf
CV	Control Volume
E-0	Case with internal emissivity set to 0.0
E-1	Case with internal emissivity set to 1.0
E-1/2	Case with internal emissivity set to 0.5
FDM	Finite Difference Method
FEM	Finite Element Method
FVM	Finite Volume Method
HP	Heat Pipe
LEO	Low Earth Orbit
LPM	Lumped Parameter Method
LVLH	Local Vertical/Local Horizontal
PCB	Printed Circuit Board
PV	Photovoltaic panel
TEG	Thermoelectric Generator
TLE	Two-Line Element

LIST OF SYMBOLS

a	Diffusive term [W/K]
a_s	Semimajor axis [km]
A	Area [m^2]
b	Albedo coefficient [-]
c	Heat capacity [J/kg.K]
C_D	Dimensionless drag coefficient [-]
C_1, C_2, C_3	Constants
day	day [-]
D	Drag magnitude [N]
$\mathbf{D}$	Drag force [N]
e	Eccentricity [-]
E	Eccentric anomaly [°]
$E_{\lambda,b}$	Spectral emissive power for black-body [W/m$^2\mu$m]
E_b	Total emissive power of black-body [W/m^2]
f_E	Eclipse fraction [-]
F	View factor [-]
$\widehat{F}$	Normalized view factor [-]
G_{i-j}	Absorption factor [-]
G_e	Heat flux from Earth [W/m^2]
G_{sun}	Solar heat flux at 1 AU [W/m^2]
i	Orbit inclination [°]
$\hat{\mathbf{I}}, \hat{\mathbf{J}}, \hat{\mathbf{K}}$	Components of the geocentric equatorial plane [-]
h	Specific angular momentum [km/s]
J$_2$]	Second zonal harmonic [-]
JD	Julian day [day]
L_s	Mean longitude of the Sun [°]
m	Mass [kg]
month	month [-]
M	Mean anomaly [°]
M_s	Mean anomaly of the Sun [°]
n	Mean motion [rev/day]
$\mathbf{n}$	Initial normal surface vector [-]
n_d	Number of days since J2000 [-]
$\mathbf{N}$	Normal surface vector after rotation [-]
N	Side of CubeSat [-]
N_{TEG}	Number of semiconductors in the TEG [-]

O	Obstruction [-]
$\mathbf{p}$	Orbital perturbation [km/s^2]
$\mathbf{p}_D$	Drag perturbation [km/s^2]
p_r, p_s, p_w	Magnitude of perturbation in the LVLH frame of reference [km/s^2]
$p_{r_D}, p_{s_D}, p_{w_D}$	Magnitude of drag perturbation in the LVLH frame of reference [km/s^2]
$p_{r_{J_2}}, p_{s_{J_2}}, p_{w_{J_2}}$	Magnitude of J_2 perturbation in the LVLH frame of reference [km/s^2]
$\hat{\mathbf{p}}, \hat{\mathbf{q}}, \hat{\mathbf{w}}$	Components of the perifocal frame of reference [-]
q	Heat [W]
q''	Heat flux [W/m^2]
q''_r	Radiative heat flux [W/m^2]
Q_{alb}	Albedo irradiance [W]
Q_e	emission of the Earth in the infrared spectrum [W]
Q_{sun}	Solar irradiance [W]
Q_{tot}	Total radiation [W]
Q_r	Radiation heat [W]
$[Q]_{X\bar{x}}$	Matrix transformation from the geocentric equatorial frame to perifocal frame [-]
$[Q]_{nad}$	Matrix rotation for Nadir attitude [-]
$[Q]_{nadir,2}$	Matrix rotation for Nadir attitude with residual rotation [-]
$[Q]_{ram}$	Matrix rotation for RAM attitude [-]
$[Q]_{sun}$	Matrix rotation for Sun attitude [-]
R	Electrical resistance [Ω]
R_i, R_j	Radius circumscribing surface i, j and k [m]
R_{ijk}	Radius from the center of surface k to the line connecting i and j [m]
r	Magnitude of CubeSat's position [km]
$\mathbf{r}$	CubeSat's position in the geocentric equatorial frame of reference [km]
$\ddot{\mathbf{r}}$	Acceleration of the CubeSat [km/s^2]
$\mathbf{r}_{\bar{x}}$	CubeSat's position in the perifocal frame of reference [km]
r_{sun}	Distance from the Earth to the Sun [km]
$\mathbf{r}_{sun}$	Sun vector [km]
R_E	Earth's radius [km]
$[R_1], [R_2], [R_3]$	Euler matrix rotations [-]
$\hat{\mathbf{r}}, \hat{\mathbf{s}}, \hat{\mathbf{w}}$	Components of the LVLH frame of reference [-]
S	Source term [W/m^3]
S_u	Constant coefficient of the source term [W/m^3]
S_P	Linear coefficient of the source term [W/m^{3}K]
t	Time [s]
Δt	Timestep [s]
T	Temperature [K]
T_{ave}	Average temperature [K]

T_p	Point temperature [K]
T_{range}	Range of temeprature [K]
T_∞	Temperature of outer space [K]
T_C	Temperature at cold side of TEG [K]
T_H	Temperature at hot side of TEG [K]
UT	Universal time [hour]
$\hat{\mathbf{u}}$	Unit vector from the Earth to the Sun [-]
$\hat{u_1}, \hat{u_2}, \hat{u_3}$	Components of the unit vector from the Earth to the Sun [-]
$\mathbf{u}_{i,j}$	Unitary vector connecting surface i and j (m)
v	Velocity magnitude [km/s]
$\hat{\mathbf{v}}$	Unitary velocity vector [km/s]
V	Volume [m^3]
ΔV	Discretized volume [m^3]
$\vec{V}_{i,k}$	Vector connecting surface i to k (m)
x,y,z	Position [m]
$\delta x, \delta y, \delta z$	Length in each direction [m]
year	year [-]
Z	Thermal resistance [K/W]
α	Absorptivity [-]
α^*	Seebeck coefficient [μV/K]
β	Angle between the orbital plane and the solar vector [°]
β^*	Minimum β without eclipse [°]
γ	Angle between the normal surface and the Earth [°]
Γ	Ecliptic true solar longitude [°]
ϵ	Angle of ecliptic [°]
ε	Emissivity [-]
θ	True anomaly [°]
θ^*	Variable to select time evaluation [-]
Θ	Rotation angle [°]
κ	Thermal conductivity [W/mK]
λ	Wavelength [μm]
Λ	Ecliptic longitude [°]
μ	Earth's gravitational parameter [km^3/s^2]
ξ	Occurrence of the Earth's shadow [-]
ρ	Reflectivity [-]
ϱ	Density [kg/m^3]
σ	Stefan-Boltzmann constant [W/m^2K^4]
χ	Angle [°]
ψ	Earth's area projection towards the Sun [-]

ω	Argument of perigee [°]
Ω	Ascending node [°]
bc	boundary condition
in	incoming
out	outgoing
nb	neighbor
^{o}	old time

CONTENTS

1 INTRODUCTION

1.1 THE STANDARD CUBESAT

For several years, the space industry was based on massive platforms and vehicles that required huge engineering teams. Due to the high cost associated with development and launching, investments in the space sector were restricted to some governments and agencies with enormous budgets (POGHOSYAN; GOLKAR, 2017). A category of satellites that has transformed this sector and continuously keeps growing is the CubeSat, a standard created in 1999 in the United States (HEIDT et al., 2000). Initially conceived for educational purposes and to immerse students into real space projects, the platform has been showing great potential for scientific, technological, and commercial missions, including the emergence of an industry segment devoted to providing technological solutions off-the-shelf for small satellites (NASA, 2019).

CubeSats can be used for small experiments, or even in some cases, to replace a single large satellite through the use of constellations with more than 300 CubeSats (SELVA; KREJCI, 2012; KULU, 2019). Due to its standard dimensions based on 1U CubeSat (10x10x10 cm) and weight (1.3 kg), the configuration yield a significant reduction of costs, time for integration, as well as cheaper launches since multiple CubeSats can be carried in a single rocket (DIAZ et al., 2016). Other compositions of CubeSats are possible, as shown in Figure 1.

Figure 1 – Main CubeSats sizes

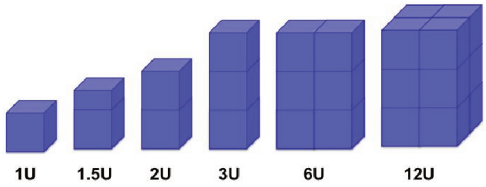

Source: NASA (2021)

The miniaturization of electronic components, the standardization, and simplification of processes, the use of COTS (Commercial-Off-The-Shelf) components with flight heritage, and the split of launching costs by multiple satellites assigned into a single launch vehicle fostered CubeSat projects with budget and deadlines below US$ 200,000 and two years, respectively (WOELLERT et al., 2011). Nowadays, CubeSat is a reality for several universities and companies interested in scientific, technological demonstration, or commercial missions, as illustrated in Figure 2. This figure shows the significant growth in the number of launched nanosatellites and estimates a considerable expansion in the next five years. Until the year 2000, 12 launches of nanosatellites occurred, while around 297 launches existed only in 2017. More than 650 launches

are expected to happen in 2021, and around 2500 new nanosatellites will be in orbit until 2025. From these new projects, around 49% of them are estimated to be from private initiatives, 32% from universities, 5% from space agencies, and 4% for military missions (KULU, 2020). A successful example of the capability of CubeSats is "Mars Cube One" (MarCO), two CubeSats 6U used to support the mission over the planet Mars (SCHOOLCRAFT; KLESH; WERNE, 2017; KRAUSE et al., 2020).

Figure 2 – Launches of nanosatellites around the world since 1998

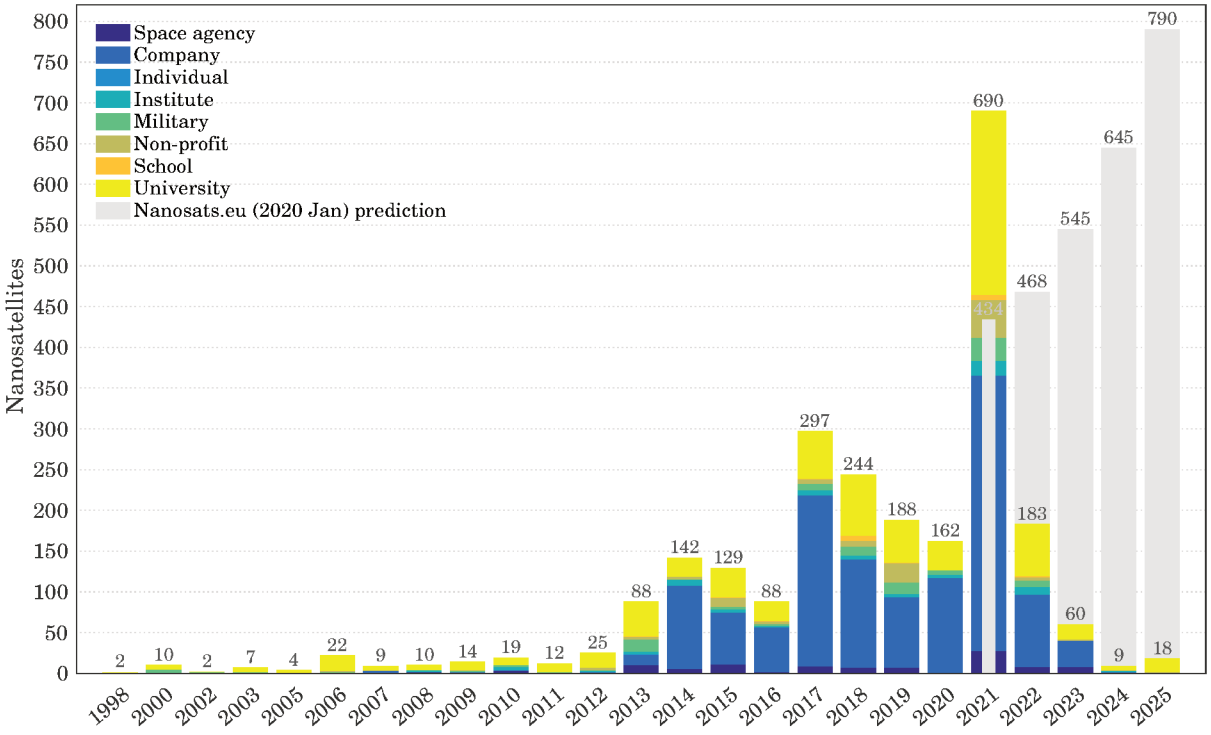

Source: Kulu (2020)

Brazil has already been inserted in this technological area, with nanosatellites missions since 2014 (SOUZA et al., 2020). The first Brazilian CubeSat, launched in 2014, is called NanosatC-Br1, a project from INPE (Instituto Nacional de Pesquisas Espaciais) and UFSM (Universidade Federal de Santa Maria). The second is AESP-14, put in orbit in 2015, and developed by ITA (Instituto Tecnológico de Aeronáutica) and INPE. In 2015 the CubeSat SERPENS-I (Sistema Espacial para Realização de Pesquisa e Experimentos com Nanosatélites) started its operation in orbit, a project from Unb (Universidade de Brasília). In 2016 was the launch of UbatubaSat, a nanosatellite from the category CanSat developed by a public school from Ubatuba - SP, with the support of INPE. ITASAT-1 is a project from ITA that was launched in 2018 and, finally, FloripaSat-I is a CubeSat from UFSC (Universidade Federal de Santa Catarina) which initiated its operation in orbit in 2019 (SOUZA et al., 2020). Figure 3 shows each one of the projects.

Like a large satellite mission, the development of a CubeSat requires a high demand for planning and analysis to address the mission objectives and requirements within a budget and

Figure 3 – Brazilian nanosatellites - CubeSats and CanSat

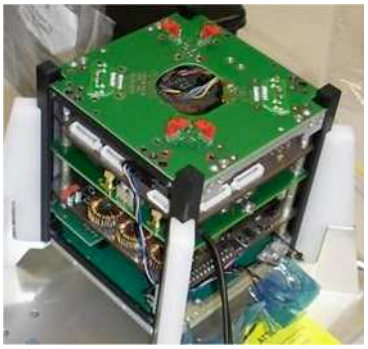

(a) NanosatC-Br1 (1U)

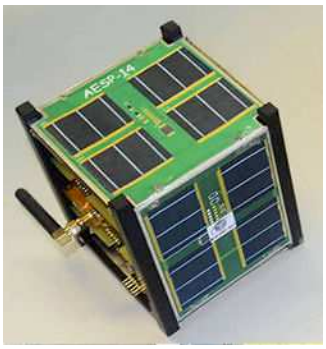

(b) ASP-14 (1U)

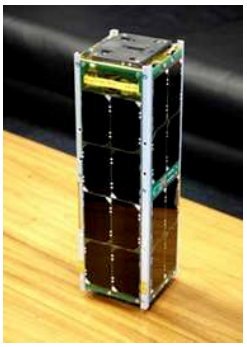

(c) SERPENS-I (3U)

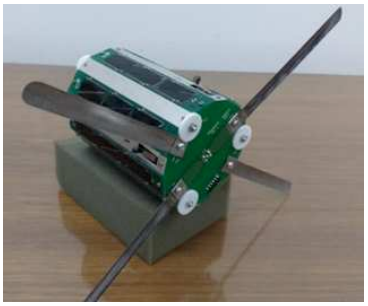

(d) UbatubaSat (CanSat)

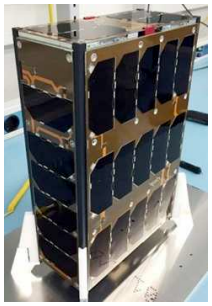

(e) ITASAT-1 (6U)

(f) FloripaSat-I (1U)

on time. Because the CubeSat is a technology that needs to survive in the space environment (vacuum, microgravity, radiation), difficult to reproduce in the laboratory, numerical modeling is an essential tool for predicting the performance of the subsystems of an orbiting spacecraft and, consequently, to support the decisions taken along the architecture's definition of the satellite. Besides that, CubeSats have limited power source, small heat capacity, limited radiator area, high-density packing of electronics, mass and volume limitations, which not necessarily results in similar scenarios of traditional medium and large satellites (SEBASTIAN; BABY, 2018). A CubeSat mission's fundamental challenge is to estimate the temperature range it will be exposed to correctly. The following section will discuss the thermal control of satellites, the main focus of this thesis.

1.2 THE THERMAL CONTROL SUBSYSTEM

A whole space mission system includes the space segment (satellite), the terrestrial segment, and the launch segment. The objective of the space segment is the operation in orbit and generation of data. The launch segment is responsible for placing the satellite in its proper orbit, while the ground station interacts with the space segment by receiving telemetry or sending telecommands (FORTESCUE; SWINERD; STARK, 2011).

The space segment can be divided into two parts: service module and payload. The payload is the mission motivation, such as a camera to take photos of the Earth's surface, a radar

to locate objects, and many other possibilities. The payload operation requires other systems to provide energy, turn it on and off, protect against the space environment, transfer the data measured with the payload, and many other tasks that are responsibilities of the service module. A typical functional breakdown of the space segment is shown in Figure 4, valid for regular satellites and CubeSats.

Figure 4 – Space segment subsystems

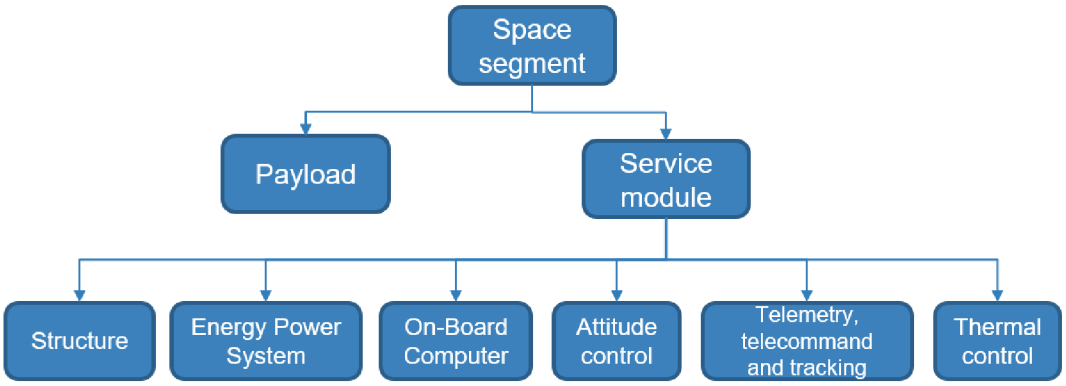

Source: Adapted from Fortescue, Swinerd and Stark (2011)

A critical subsystem in these satellites, including CubeSats, is the thermal control. It is responsible for keeping every part of the satellite within affordable ranges of temperature through its life-cycle (GILMORE; DONABEDIAN, 2002). Some examples of temperature behavior in orbit are shown in Figure 5. The oscillatory but nearly cyclic pattern comes from exposition to the Sun followed by the Earth eclipse, resulting in an orbit period of around 90 minutes for Low Earth Orbit (LEO) and eclipse of approximately 35 minutes for all the cases. Under the shadow of the Earth, these CubeSats reach the lowest temperatures due to the lack of solar radiation. These figures show significant transient and temperature gradients in orbit and different temperature levels for the same satellite. Launched in April 2007, CubeSat CP3 had a Sun-synchronous orbit, an altitude of 700 km, but no information was available regarding its spin. It can be observed that its limits of temperature for one complete orbit are more compressed a few weeks after the launch (left) than the sample valid for one year later (right). CubeSat CP3 was below 300 K in the beginning of the missions and reached more than 320 K 12 months later. A similar trend is observed in the results from two full orbits of SwissCube, with around 15 K of temperature increase between the figures that are 15 months apart. In both situations, the temperature gradient expanded between these plots and could be associated with different thermal radiation scenarios. In fact, in Figure 5c the CubeSat was rotating faster than 600 °/s, while less than 5°/ in Figure 5d, which created different exposition of its surfaces to the irradiation fluxes. The internal temperature of some parts of SwissCube and Zacube are in Figure 5e and Figure 5f and shows that the internal parts of these satellites are less susceptible to temperature variations.

As an example, Table 1 shows the recommended temperature range for the main subsystems of CubeSat 1U FloripaSat-I. Temperature levels beyond the recommended values may

Figure 5 – Temperature data from CubeSats in orbit

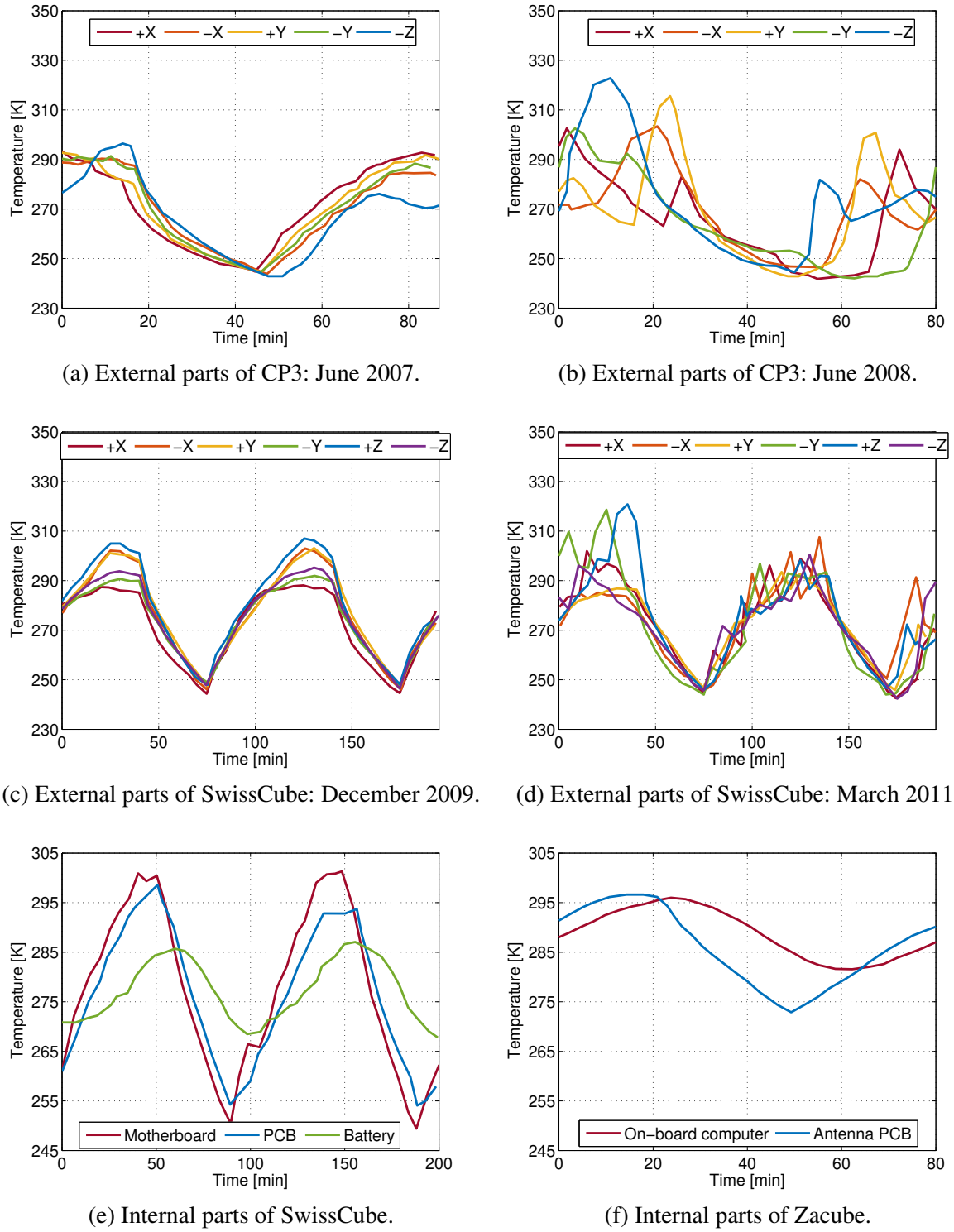

(a) External parts of CP3: June 2007.

(b) External parts of CP3: June 2008.

(c) External parts of SwissCube: December 2009.

(d) External parts of SwissCube: March 2011.

(e) Internal parts of SwissCube.

(f) Internal parts of Zacube.

Source: Adapted from Firedel (2011), Kramer (2019a), Kramer (2019b)

permanently damage the satellite, but even deviations from optimum point results in an inefficient operation (DEHBONEI; LEE; NEHRIR, 2009; CHIN et al., 2018; QIAO; RIZOS; DEMPSTER, 2013). Following a trend observed in other projects, the battery is the component that has the most restrictive range and may require thermal intervention to avoid excessively low or high

temperatures.

Table 1 – Range of temperature for the main parts of FloripaSat-I

Component	Temperature range [K]
Antenna	233 to 358
Structure	233 to 353
On-Board Computer	233 to 358
Payload	233 to 358
Battery (charge)	268 to 318
Battery (discharge)	253 to 333
Electric Power System	233 to 358
Solar panel	233 to 358

Source: SpaceLab (2017)

Therefore, even before a satellite leaves the ground, scenarios should be tested to understand the satellite's behavior in orbit and minimize failures or an inadequate operation of the satellite (LANGER; BOUWMEESTER, 2016). These acceptable practices are mostly valid for CubeSat projects, which are satellites of small physical dimensions, generally of low cost, with extensive use of COTS elements, short schedule, short operational lifetime, limited redundancy, and extensive testing focused on system-level (ESA/ESTEC, 2013). In addition to the safe operation obtained through the thermal control, it can also be used to maximize the energy generation of orbiting spacecraft mounted with photovoltaic cells (PV) due to a phenomenon of better solar cell efficiency under low temperature (DEHBONEI; LEE; NEHRIR, 2009; CHIN et al., 2018). In this case, both temperature and radiation levels are essential in numerical simulations to predict the orbit conditions and obtain more reliable outputs.

This thesis aims to contribute to CubeSat projects' thermal evaluation through a framework composed of radiation and heat transfer models.

1.3 MOTIVATION

In LEO, the main external heat sources over spacecraft have origin in the direct emission of radiation by the Sun near the visible wavelength, the reflection of sunlight by Earth, and radiation emission by Earth in the infrared wavelength. For practical applications dealing with heat transfer on satellites, these sources may be assumed constant throughout the orbit. However, the satellites' position and orientation may not be, and both orbital parameters and attitude will define the amount of irradiance reaching surfaces, duration of the eclipse, which sides are shadowed by nearby neighborhood and, consequently, the temperature field.

A good irradiance estimation is helpful for hardware in the loop simulators like the "Sun simulator" presented in Marcelino et al. (2020), where the authors connected LEDs to LabView in order to emulate the orbit conditions in their experiments or the procedures to

emulate solar panels and batteries described in Slongo et al. (2018), both focusing on FloripaSat-I. As stated in Corpino and Stesina (2014), through the case study of the e-st@r-I CubeSat, the hardware in the loop is an essential process for verifying the functional requirements of CubeSats. Another example of the hardware in the loop approach was implemented in the development of the CubeSat MOVE-II to simulate the space environment in real-time during on-ground tests (KIESBYE et al., 2019). Their work emulated a solar array's electrical behavior through a voltage-current characteristic curve, a function of illumination level and temperature of the array's photovoltaic cells.

In the work of Knap, Vestergaard and Stroe (2020), the authors dedicate to review the environmental conditions and their impact on typical batteries used in CubeSat missions. For low values of temperature, usually below -20°C and 0°C for discharge and charge conditions, respectively, there is a rapid degradation of its performance. The same tendency of low efficiency exists for high values of temperature. The levels of irradiation and its accumulation through the orbit lifetime reduce the battery's performance, especially when shielding is absent. Aung et al. (2020) developed and conducted experimental tests regarding the state-of-charge estimation for the battery of satellites, totally dependent on the power generation capacity of the photovoltaic cells. However, the authors did not assess it considering typical transient irradiance and temperature profiles found in orbit. Thermal simulations of CubeSats are found in Corpino et al. (2015), Claricoats and Dakka (2018), Kovács and Józsa (2018), Bonnici et al. (2019), Filho et al. (2020), where the authors solve the transient temperature of critical components of the satellite, like the battery or some electronic component of a payload, to understand if the thermal operational limits of the satellite are satisfied. Other examples of temperature critic areas in CubeSats include power harvesting with active thermal control (POSIELEK, 2018), thermo-mechanical structural failure (BEDNOVA; YUMASHEV, 2018), thermoelectric generators (OSTRUFKA et al., 2019), and biological experiments in orbit (PADGEN et al., 2020). Therefore, thermal simulation is a crucial tool to project reliable and efficient CubeSat missions.

Wherefore, this research is justified by these initial observations that reveal a gap for thermal simulation of CubeSats, which includes the simulation itself based on the solution of the energy equation, but also the modeling of the boundary conditions, namely the irradiance sources that are functions of orbit mechanics and attitude of the satellite, or that related to the internal heat transfer by radiation. Therefore, this research intends to develop and integrate both irradiation and thermal models dedicated to solving CubeSats' temperature field.

1.4 OBJECTIVES

This work's main objective is to design a simulation framework — integrating irradiance and thermal models — to evaluate the thermal behavior of CubeSats and support future missions. Following this primary goal, the specific objectives are:

- Specific Objective 1:
  To implement and analyze an irradiance flux model considering orbit, attitude, and radiation parameters along the CubeSat life-cycle;

- Specific Objective 2:
  To design and evaluate a thermal model of CubeSats – employing finite volume method – with internal heat transfer by radiation;

- Specific Objective 3:
  To integrate the previously presented irradiance and thermal models in order to obtain a fully-working simulation framework for CubeSats, and analyze the resulting outcome in representative scenarios.

1.5 MAIN CONTRIBUTION AND STRUCTURE OF THE THESIS

The main contributions of this thesis are divided in three chapters:

- *Chapter 2:* An irradiance model to estimate the radiation over each side of CubeSats in LEO. Three main models are integrated to estimate the irradiation flux, namely an orbit, an attitude, and a radiation source model, including solar, albedo, and infrared emitted by the Earth. The orbit model has an atmospheric drag and gravitational gradient as perturbations; therefore, the user can perform analysis for the satellite's entire operational life-cycle until its reentry in the atmosphere. The attitude formulation mimics the satellite's spin for typical missions, linking the rotation of the satellite and the area projection to the irradiation sources.

- *Chapter 3:* A transient thermal simulation of a typical CubeSat 1U mission is deisgned considering the Finite Volume Method (FVM). The boundary conditions include the external and internal heat transfer by radiation. The external ones come from the irradiation model, while the Gebhart method computes the internal heat exchange through successive reflections, and an obstruction model supports the estimation of surface view factors. Three boundary conditions inside of CubeSat are tested through the control of the surface emissivity (ε): without internal heat transfer by radiation ($\varepsilon = 0.0$), with intermediate internal heat transfer by radiation ($\varepsilon = 0.5$), and maximum internal heat transfer by radiation ($\varepsilon = 1.0$). A simpler Lumped Parameter Method is introduced to compare its results and those from the FVM.

- *Chapter 4:* The results from the integrated irradiance and thermal models start by assessing the impact of the internal heat transfer by radiation, which evidences its importance in the temperature field of both inner and outer parts of the satellite. Therefore the internal heat

transfer by radiation should not be ignored in numerical simulations regarding CubeSats. Good agreement of transient temperature is found between the FVM and LPM when a single point on each side of the satellite is monitored. However, three-dimensional effects are significant and highlight the necessity of numerical models to predict the transient and spatial temperature gradient appropriately. Further possibilities of these models are illustrated and include the integration of a heat pipe connecting two opposite solar panels and the electrical performance of a thermoelectric generator (TEG).

These chapters result from a collection of scientific journals (published or submitted for publication) developed along the doctoral studies of this author, which in totality they are:

- A. Ostrufka, E. Filho, A. Borba, A. Spengler, T. Possamai, K. Paiva, Experimental evaluation of thermoelectric generators for nanosatellites application, Acta Astronautica 162 (2019) 32 – 40. URL: <https://doi.org/10.1016/j.actaastro.2019.05.053>;
- E. M. Filho, L. O. Seman, C. A. Rigo, V. P. Nicolau, R. G. Ovejero, V. R. Q. Leithardt, Irradiation flux modelling for thermal–electrical simulation of CubeSats: Orbit, attitude and radiation integration, Energies 13 (2020). URL: <https://www.mdpi.com/1996-1073/13/24/6691>;
- E. Morsch Filho, V. P. Nicolau, K. V. Paiva, T. S. Possamai, A comprehensive attitude formulation with spin for numerical model of irradiance for cubesats and picosats, Applied Thermal Engineering 168 (2020) 114859. URL: <https://doi.org/10.1016/j.applthermaleng.2019.114859>;
- C. A. Rigo, L. O. Seman, E. Camponogara, E. Morsch Filho, E. A. Bezerra, Task scheduling for optimal power management and quality-of-service assurance in CubeSats, Acta Astronautica 179 (2021) 550 – 560. URL: <https://doi.org/10.1016/j.actaastro.2020.11.016>;
- S. Vega Martinez, E. M. Filho, L. O. Seman, E. A. Bezerra, V. P. Nicolau, R. G. Ovejero, V. R. Q. Leithardt, An integrated thermal-electrical model for simulations of battery behavior in cubesats, Applied Sciences 11(2021). URL:<https://doi.org/10.3390/app11041554>;
- Rigo, C. A.; Seman, L. O.; Camponogara, E.; Morsch Filho, E.; Bezerra, E. A.. A nanosatellite task scheduling framework to improve mission value using fuzzy constraints. Expert Systems with Applications (2021), doi:<https://doi.org/10.1016/j.eswa.2021.114784>;
- E. Morsch Filho, L. O. Seman, V. P. Nicolau, Numerical simulation of a CubeSat based on the Finite Volume Method with internal obstructing radiatibe heat transfer, Applied Thermal Engineering[1].

[1] Submitted but without final decision from editor

The main publications of the author in congress related to this thesis are:

- E. Morsch Filho, R. SANTIAGO, M. M. B. COSTA, K. V. PAIVA, T. S. POSSAMAI, R. Oba, G. B.HUGHES, Preliminary studies of the impact on temperature of a high-power laser on-board a 6U CubeSat, in: II CubeSats and NanoSats for Remote Sensing, San Diego, California, EUA, 2018;
- MORSCH FILHO, S. V. MARTINEZ, L. K. SLONGO, E. A. BEZERRA, T. S. POSSAMAI, V. P. Nicolau, Preliminary results for energy harvesting maximization with focus on heater control of batteries in nanosatellites, in: III IAA Latin American CubeSat Workshop, Ubatuba, SP, 2018;
- C. A. RIGO, O. L. Seman, E. Camponogara, E. MORSCH FILHO, L. K. SLONGO, E. A. BEZERRA, Mission plan optimization strategy to improve nanosatellite energy utilization and tasks QoS capabilities,in: IV IAA Latin American Cubesat Workshop, 2020. IAA LACW, Virtual.

2 IRRADIATION FLUX MODELING

A numerical tool to explore typical irradiation scenarios for CubeSat missions is the main goal of this chapter. Such a tool can provide the input estimation for software and hardware in the loop analysis for a given initial condition and predict it along with the satellite's lifespan. Three main models will be developed to estimate the irradiation flux over a CubeSat, namely an orbit, an attitude, and a radiation source model.

2.1 LITERATURE REVIEW OF IRRADIANCE SOURCES

A spacecraft design's dynamic performance should include kinetic, attitude, electrical, thermal, and communication performances. However, not all real effects can be included in the system model, and simplifications are introduced (RAIF; WALTER; BOUWMEESTER, 2010). Two areas of great concern in CubeSat applications are power generation and temperature, both closely related to irradiance input. Figure 6 shows the primary irradiation sources for a satellite in LEO.

Figure 6 – The irradiance sources for satellites in LEO

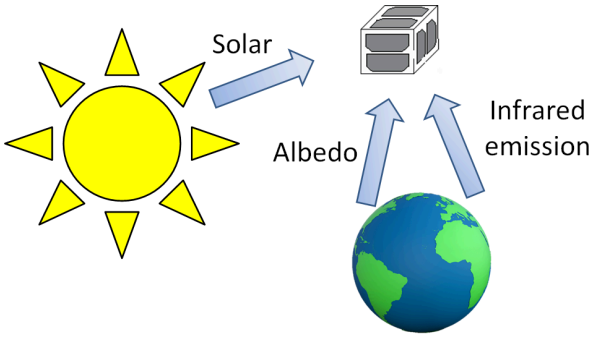

Source: The author

For the two cases of power generation and temperature field, solar radiation is the main source. Due to the distance between the Earth and the Sun, the solar rays are practically parallel when they reach the CubeSat. The recommended value for the flux of radiation by the Sun at the distance of 1 AU (astronomical unit) is $G_{sun} = 1367$ W/m^2, equivalent to a black-body at the effective average temperature of 5500°C, although there are slight variations due to the cyclic activity of the Sun every 11 years and the elliptic orbit of the Earth (1322 W/m^2-1414 W/m^2) (GILMORE; DONABEDIAN, 2002). The solar spectral distribution has a peak around 0.5 μm, whose energy distribution is 7% in the ultraviolet, 46% in the visible, and 47% near the infrared.

A second important source of irradiation for photovoltaic and thermal problems of CubeSats in LEO is a consequence of the reflection of solar rays by the Earth, called albedo

(GILMORE; DONABEDIAN, 2002). There is not a unique and accurate model valid for satellite applications because it is a function of a great diversity of parameters, as atmospheric conditions, clouds, and the ground surfaces (BERG et al., 2020; CUI; MITOMI; TAKAMURA, 2009). Continental areas have a higher albedo coefficient than the ocean, so do lands covered by snow and sand. The global annual average, widely accepted for satellites in LEO, is $b = 0.3$ (LYLE; LEACH; SHUBIN, 1971; RODRIGUEZ-SOLANO; HUGENTOBLER; STEIGENBERGER, 2012). The Earth's surface and atmosphere behave like a Lambertian surface; therefore, the reflected radiation can be represented by a phase function (RODRIGUEZ-SOLANO; HUGENTOBLER; STEIGENBERGER, 2012), whose reflectance increases with a reduction in the solar elevation angle. In other words, the albedo is maximum below the subsolar point, which is the point on the surface whose Sun is upright, and vanishes at the line between the shined and shadowed sides of the Earth (GILMORE; DONABEDIAN, 2002; LYLE; LEACH; SHUBIN, 1971; ROMÁN et al., 2010). The albedo's spectral distribution has significant variation within 0.29 to 5.00 μm (LYLE; LEACH; SHUBIN, 1971; GOODE et al., 2001). After the direct solar radiation, the diffuse albedo radiation is the most significant load for a PV, even though there are shifts and gaps in its spectrum compared to the direct solar radiation (BRENNAN et al., 2014).

Another source of irradiation for satellites in LEO assumed in this work is the infrared radiation emitted from the Earth, useful for thermal problems but neutral for the photovoltaic effect as it is a much longer wavelength than the Sun's emission ($> 4\mu m$). Warmer surfaces of the Earth will emit more radiation than colder, but dense clouds can block it before it hits the satellite, reason for significant variations worldwide, although much less severe than albedo (GILMORE; DONABEDIAN, 2002; LYLE; LEACH; SHUBIN, 1971). This infrared radiation is usually higher near the subsolar point, while it is lower near the poles and at night, a consequence of the surface's temperature. Although there are these variations, an average and constant value usually assumed in the literature is a flux of $G_e = 237$ W/m^2 based on the effective average temperature -18°C for the Earth's surface (LYLE; LEACH; SHUBIN, 1971; GILMORE; DONABEDIAN, 2002). In this context, another final irradiation is from the cosmic microwave background, corresponding to black-body radiation at 2.7 K, although its magnitude is minuscule compared to the previous sources mentioned above. By modeling these radiation sources, traditional satellites and nanosatellites are thermally tested. For example, the Chinese GF-4 satellite had a difference between the predicted and measured temperatures around 3°C for most of the components (LI; WANG; ZHANG, 2020). FloripaSat-I (FILHO et al., 2020), PiCPoT (CORPINO et al., 2015), UoMBSat-1 (BONNICI et al., 2019), and SMOG-1 (KOVÁCS; JÓZSA, 2018) are examples of CubeSat missions with thermal simulations.

One preliminary way to visualize the general radiation environment that a satellite in orbit is exposed to can be done through the orbit β angle, which defines the minimum angle between the orbit plane and the solar vector (GILMORE; DONABEDIAN, 2002), as shown in Figure 7.

Figure 7 – The β angle

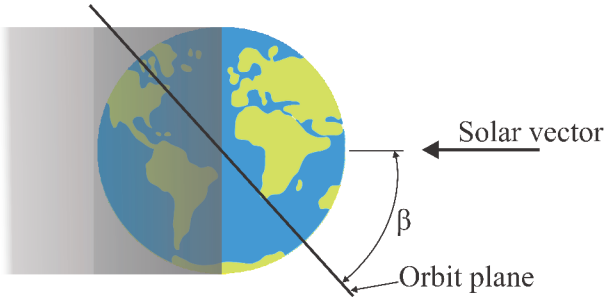

Source: The author

For an angle $\beta = 0°$, the orbit has the longest eclipse caused by the Earth, and the albedo is maximum whenever the satellite passes below the subsolar point, which is when the same solar ray passes through the satellite and the center of the Earth. For any value different than $0°$, the eclipse is shorter, the peak of albedo reduces, and, as β increases, the eclipse decreases until a point where it vanishes, depending on the altitude. At exactly $\beta = 90°$, the albedo is null. Therefore, a high value for β may be interesting for the photovoltaic cells; however, it may not be in terms of heat transfer if the satellite must keep low temperatures. β is nearly constant along the months only for Sun-synchronous orbit, a special case where, for satellites in LEO, the orbit inclination is around $98°$. Over several months, keeping a constant β angle requires thrusters in the spacecraft to counterbalance the orbit's perturbations. For the remaining cases, it is expected a significant variation of β within days, but limited to $\beta = \pm(\epsilon + |i|)$, where ϵ is the ecliptic angle (around $23.4°$) and i the orbit inclination. Therefore, it is important to recognize that the CubeSat's missions may be exposed to different β, so it is indispensable to understand the orbit behavior to predict its future positions. The importance of the parameter β with the irradiation sources cited above has already been used for temperature estimation and comparison with experimental temperature data of the International Space Station (ISS), obtaining good consistency of the results (ZHENG et al., 2020). The CubeSat CIIIASat also presents temperature results and its relation with β (REYES et al., 2020).

Fundamental is also to inform the initial state. It is common to use the standard Two-Line Elements (TLE), which comprehends a set of orbital parameters obtained from satellite tracking observations, for example, available at the CelesTrak database[1]. The CelesTrak database is a helpful platform to initialize orbit simulations with real input if the user wishes to run real orbit conditions. In its catalog, the user can find the TLE of more than 16,000 objects, including CubeSats and their historical data (HANEVEER, 2017). The use of TLE is encouraged because it is open-access and worldwide spread. Nevertheless, it is valid to mention that the TLE is a picture of the current orbit and is not valid for future orbits due to the natural perturbations presented in every orbit.

[1] www.celestrak.com

The following figure shows a TLE sample format, which includes more data than necessary for orbital simulation, for example, the identification of a satellite, a date, and other parameters.

Figure 8 – Two-line Element Set Coordinate System

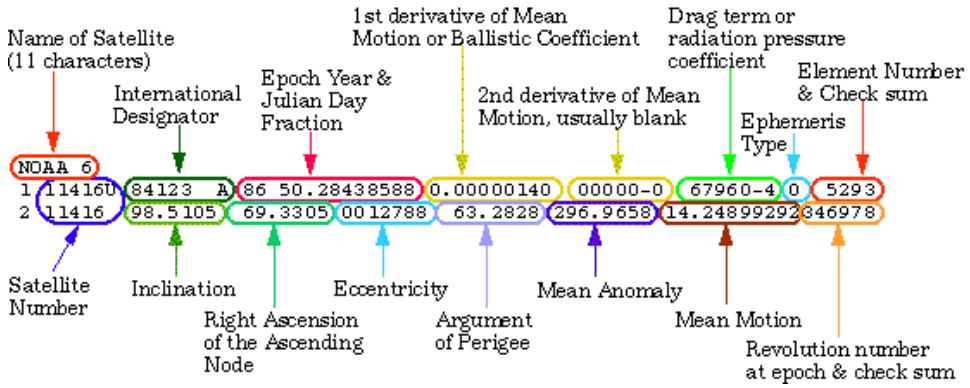

Source: NASA (2020)

The actual trajectory of a satellite does not strictly follow the ideal Keplerian orbit. In more or less sense, every orbit is subject to perturbations, which is the effect that causes the deviation from the Keplerian orbit. The non-spherical central body, atmospheric drag, solar radiation pressure, thrust, and gravitational interactions with celestial bodies are the most common perturbations for the orbit. For satellites in LEO, especially below 600 km, which is most of the CubeSat missions, the major perturbations originate from the atmospheric drag and gravitational perturbations (CURTIS, 2014; CAPDEROU, 2014). An overview of these perturbations is in Figure 9.

The space environment is not a perfect vacuum. Eventually, the satellite will hit molecules of gas, which will decrease its velocity and retard the satellite's motion (MCCLAIN; VALLADO, 2001). The probability of hitting these molecules decreases with the altitude, but it is not zero. The density of the atmosphere is around 10^{-6} kg/m^3 at 100 km of altitude, a reference value where space begins, then it decreases to 10^{-11} kg/m^3 at 400 km, which is close to the altitude of the ISS (CURTIS, 2014). As a consequence of this drag, elliptic orbits are circularized, the angular momentum decreases, and so does the orbit altitude until the satellite reenters the atmosphere if no booster acts. Atmospheric density is a critical factor for correctly predicting this perturbing force (ATALLAH, 2018; HANEVEER, 2017), which is a reason for a great variety of models with diverse accuracy and computational costs in the literature. The models from the families Jacchia, MSIS, and DTM are usually preferred because they have good accuracy and computational cost, notably NRLMSISE-00 (VALLADO; FINKLEMAN, 2014; PICONE et al., 2002).

The Earth does not have perfect mass distribution, neither is it a perfect sphere (CURTIS, 2014). For these reasons, the gravitational field varies with latitude, longitude, and radius. Due to the oblateness of the Earth (radius at the equator is bigger than in the poles), the right ascension

Figure 9 – Perturbation accelerations as function of the altitude

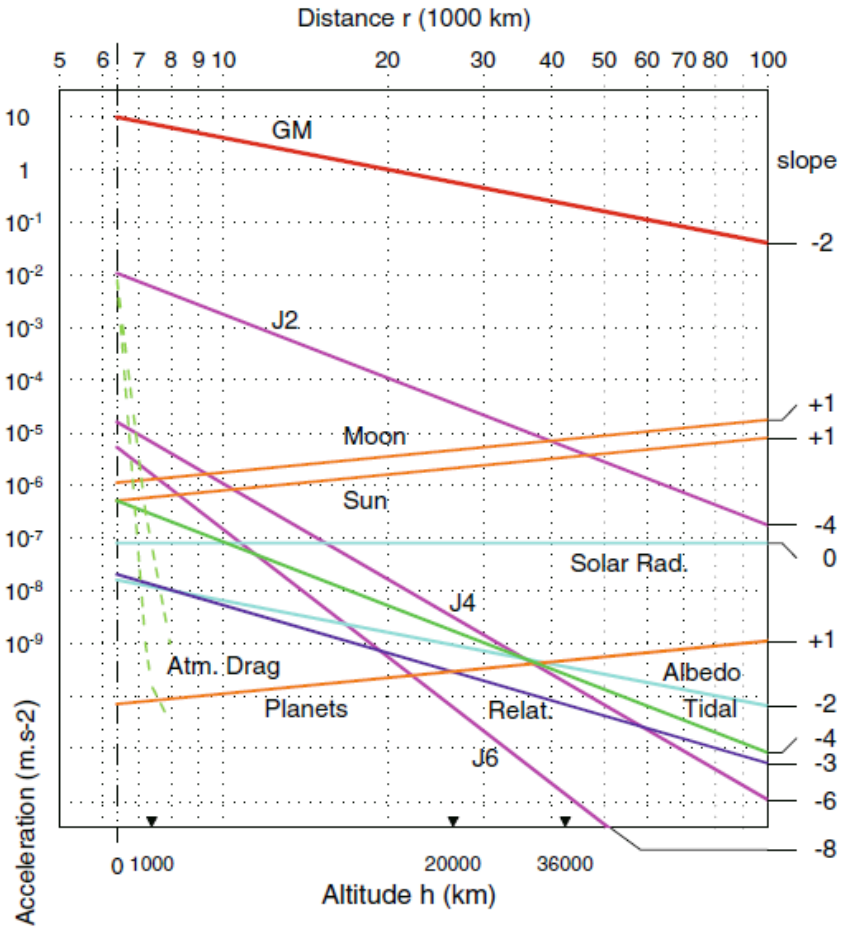

Source: Capderou (2014)

angle (Ω), and the argument of perigee (ω) of an orbit suffer significant variation with time. Satellites take advantage of this feature to work in specific orbit inclination (i), as the Sun-synchronous ($i \approx 98°$) and Molniya ($i \approx 63°$), whose orbital plane makes a constant angle with the Sun and the apse line remains constant, respectively. The equation to describe this perturbation is given by an infinite series, which depends on zonal harmonics (J_k) of the Earth and Legendre polynomials. The zonal harmonic J_2 is the biggest one for LEO, and it is usually the only term considered in the simulations without significant loss of accuracy. This perturbation's primary effect is the precession of Ω and ω (HANEVEER, 2017).

Indeed, perturbations are always present, and their suppression introduces meaningful errors in estimating the satellite's position or even the planetary positions. However, it is impractical to include all known perturbations and use very small timesteps without a huge computational time (HANEVEER, 2017). In order to propagate the perturbed orbits, three techniques arise: special (numerical method), general (analytical method), and semi-analytical (combination of numerical and analytical) (MCCLAIN; VALLADO, 2001). The first case is based on direct numerical integration rather than analytical expressions for perturbation, resulting in greater

accuracy if a sufficient small timestep is applied, with lower complexity for special perturbations; reason for its great application (BATE; MUELLER; WHITE, 1971; HANEVEER, 2017). Within the special perturbation, there are three techniques: Cowell, Encke, and Variation-of-elements. Cowell's method is the simplest and basically permits all the perturbations to be added linearly in the equation of motion and then numerically integrated (MCCLAIN; VALLADO, 2001). This great advantage of simplicity brings drawbacks as the necessity of tiny time steps, depending on the perturbing force's magnitude. On the other hand, Encke's method integrates the difference between the perturbation and the unperturbed motion, requiring rectifications along this process. It is a much faster technique than Cowell; however, current processors' computational cost minimizes this drawback. The Variation-of-elements was developed by Euler in 1748 and relies on the expression of rates of any consistent set of six orbital parameters, condition to describe a two-body orbit, as the trajectory of satellites. By numerically integrating these analytical rates, the state-vector of the satellite is then found. Since these parameters vary much slower than the state-vector itself, a bigger timestep still provides precise results (BATE; MUELLER; WHITE, 1971). For many orbit estimation applications based on numerical integration, a fourth-order Runge-Kutta (RK4, single-step) method is sufficient (MCCLAIN; VALLADO, 2001; SHUSTER, 2017).

One last parameter of concern and fundamental for irradiance analysis is the satellite's attitude. Issues related to communication, thermal control, and power generation are all impacted by a satellite's dynamic in orbit. When dealing with small satellites as CubeSats, this becomes more critical as the available space to comport typical engineering solutions is very small, as the available external area for photovoltaic cells (FILHO et al., 2020). Usually, publications without the focus on control theory idealize the spin of a CubeSat only in a single axis, generally with one face towards the Earth, with an attitude model not versatile enough to reproduce different scenarios (PARK; MIYATA; NAGANO, 2017; MASON et al., 2018; KOVÁCS; JÓZSA, 2018; LEE et al., 1999; FARHANI; ANVARI, 2014). The researchers who deal with attitude control use different approaches to describe the satellite's rotation, as Euler angles, quaternions, and Direction Cosine Matrix (ROLDUGIN; TESTANI, 2014; XING et al., 2010; AURET; STEYN, 2011). Euler angles are more intuitive to visualize than quaternion or Direct Cosine Matrix, but quaternion is the only free of singularities.

2.2 METHODOLOGY

The methodology to estimate the transient irradiance field of this work bases on:

- An algorithm to estimate the orbit of a satellite and its position, valid for elliptical and circular orbits subject to perturbations caused by the atmospheric drag and the effect of the Earth oblateness, available at Curtis (2014);
- A simplified algorithm developed by the authors herein to mimic the attitude of the satellite;

- A model to project a CubeSat's surfaces towards the irradiance sources, namely solar, albedo, and infrared radiation of the Earth.

Therefore, this problem will be described by three main models to be further detailed in the next section: Orbit, Attitude, and Irradiation source.

2.2.1 Orbit Model

The objective here is to estimate the position of the CubeSat in orbit. A generic view of a CubeSat is shown in Figure 10 with some of the parameters required to define it completely.

Figure 10 – The orbit and position of a CubeSat

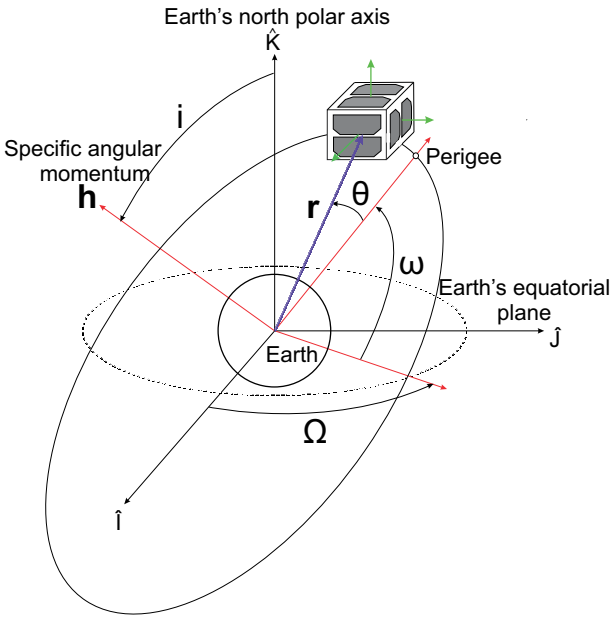

Source: The author

The constants of the model are:

- Earth's gravitational parameter: $\mu = 398600$ km^3/s^2;
- Earth's radius: $R_E = 6378$ km;
- Second zonal harmonics J$_2$= 1.08263×10^{-3} [-].

To initiate the simulation, the first thing needed is the vector of Classical Orbital Elements (COE) [h_0,e_0,Ω_0,i_0,ω_0,θ_0], where the subscript 0 means the value at the beginning of the simulation t_0. To obtain the COE at t_0, the algorithm will rely on TLE data so that the user can test with real CubeSat's orbit information. However, only six parameters from the whole TLE will have to be declared by the user, namely:

- i: orbit inclination [°];

- Ω: right ascension of the ascending node [°];
- e: eccentricity [-];
- ω: argument of perigee [°];
- M: mean anomaly [°];
- n: mean motion [rev/day];

The specific angular momentum (h [km/s]) and the true anomaly (θ [rad]) are not readily available from TLE, so they are calculated by Equations (2.1)—(2.4), where a_s is the semimajor axis [km] and E is the eccentric anomaly [rad] (CURTIS, 2014).

$$a_s = \sqrt[3]{\frac{\mu}{n^2}} \tag{2.1}$$

$$h = \sqrt{a_s \mu \left(1 - e^2\right)} \tag{2.2}$$

$$E - e \sin\left(E\right) = M \tag{2.3}$$

$$\theta = 2 \tan^{-1}\left[\sqrt{\frac{1+e}{1-e}} \tan\left(\frac{E}{2}\right)\right] \tag{2.4}$$

It is crucial to transform the mean motion units to rad/s and all the angles to radians. The eccentric anomaly is solved by some iterative method, for example, the Newton-Raphson. The user also has to inform the day, month, and year in the beginning of the simulation to estimate Sun's position, as will be shown later.

To find the position of the CubeSat in orbit, there are three reference frames. The inertial Cartesian reference frame called geocentric equatorial frame, shown in Figure 11, is defined in terms of the right-handed triad unitary vector $[\hat{\mathbf{I}}, \hat{\mathbf{J}}, \hat{\mathbf{K}}]$ and located at the center of the Earth (Figure 10). The component $\hat{\mathbf{I}}$ points to the vernal equinox direction, $\hat{\mathbf{K}}$ is the axis of rotation of the Earth, while $\hat{\mathbf{J}}$ is orthogonal to them and forms the Earth's equatorial plane.

The second reference frame is the perifocal frame of reference, not shown in Figure 11. It is fixed in space, centered at the focus of the orbit and defined by $[\hat{\mathbf{p}}, \hat{\mathbf{q}}, \hat{\mathbf{w}}]$. $\hat{\mathbf{p}}$ points to the periapsis (nearest point of the orbit to the Earth), $\hat{\mathbf{q}}$ is 90° true anomaly from the periapsis, and $\hat{\mathbf{w}}$ is normal to the plane of the orbit. The true anomaly is measured from this $\hat{\mathbf{p}}$ axis of the perifocal frame of reference (Figure 12). The position of the CubeSat in the perifocal frame of reference ($\mathbf{r}_{\bar{x}}$) may be expressed as:

$$\mathbf{r}_{\bar{x}} = r \begin{bmatrix} \cos\left(\theta\right) \\ \sin\left(\theta\right) \\ 0 \end{bmatrix} = \frac{h^2}{\mu} \frac{1}{1 + e\cos\left(\theta\right)} \begin{bmatrix} \cos\left(\theta\right) \\ \sin\left(\theta\right) \\ 0 \end{bmatrix} \tag{2.5}$$

where r is the magnitude of the position [km].

Figure 11 – Geocentric equatorial frame of reference

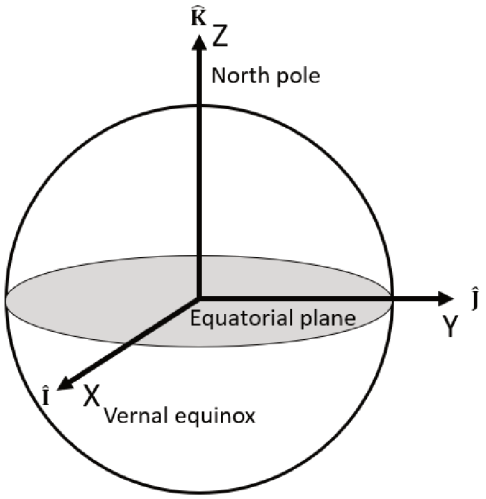

Source: Adapted from Curtis (2014)

Figure 12 – Perifocal frame

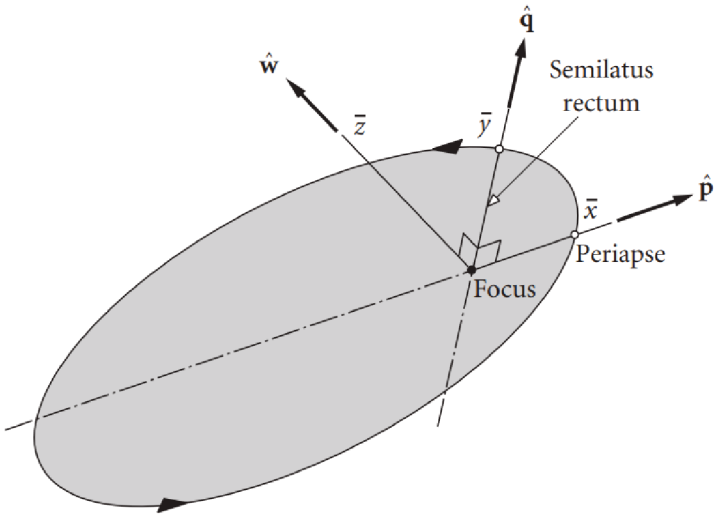

Source: Curtis (2014)

The transformation from the perifocal frame into the geocentric equatorial frame is done by the classical Euler sequence shown in Equation (2.6).

$$[Q]_{X\bar{x}} = [R_3(\omega)][R_1(i)][R_3(\Omega)] \tag{2.6}$$

The angles Ω, ω and i are known as the Euler angles, and the matrices in previous

equation are:

$$[R_3(\Omega)] = \begin{bmatrix} \cos(\Omega) & \sin(\Omega) & 0 \\ -\sin(\Omega) & \cos(\Omega) & 0 \\ 0 & 0 & 1 \end{bmatrix} \tag{2.7a}$$

$$[R_1(i)] = \begin{bmatrix} 1 & 0 & 0 \\ 0 & \cos(i) & \sin(i) \\ 0 & -\sin(i) & \cos(i) \end{bmatrix} \tag{2.7b}$$

$$[R_3(\omega)] = \begin{bmatrix} \cos(\omega) & \sin(\omega) & 0 \\ -\sin(\omega) & \cos(\omega) & 0 \\ 0 & 0 & 1 \end{bmatrix} \tag{2.7c}$$

The matrix in Equation (2.6) is orthogonal, so the position of the CubeSat in the equatorial frame may be finally calculated by:

$$\mathbf{r} = [Q]^{\mathsf{T}}_{X\bar{x}}\mathbf{r}_{\bar{x}} \tag{2.8}$$

The initial position of the satellite can be already found with the TLE input. For an ideal orbit without perturbation, the user would utilize a timestep, the information of mean motion (n) and the mean anomaly (M) to find the next true anomaly (θ), then the position of the CubeSat. However, for the case with perturbation, there are few more steps in this process.

Equation (2.9) is valid for the motion in an inertial reference frame with the presence of perturbation ($\mathbf{p}$), where the first term on the right side originates from the Keplerian orbit while the second is the perturbation. Ignoring the second term gives the origin of the ideal motion without perturbation briefly discussed above.

$$\ddot{\mathbf{r}} = -\mu\frac{\mathbf{r}}{r^3} + \mathbf{p} \tag{2.9}$$

where $\ddot{\mathbf{r}}$ is the acceleration of the CubeSat [km/s^2].

Before introducing more equations, a new reference frame is used, called local vertical/local horizontal (LVLH). It is non-inertial, represented by the triad $[\hat{\mathbf{r}}, \hat{\mathbf{s}}, \hat{\mathbf{w}}]$; $\hat{\mathbf{r}}$ is the unit vector of $\mathbf{r}$ and follows the position of the satellite in orbit, $\hat{\mathbf{w}}$ is the same of the perifocal frame, therefore normal to the orbit plane, and $\hat{\mathbf{s}}$ is the resulting cross product between these vectors. The components of a perturbation force in the LVHL reference frame are given by Equation (2.10).

$$\mathbf{p} = p_r\hat{\mathbf{r}} + p_s\hat{\mathbf{s}} + p_w\hat{\mathbf{w}} \tag{2.10}$$

The perturbing forces considered in this work will be the drag and the gravitational perturbation J_2 because the cases to be studied here are below 600 km of altitude, a region where these forces are of greater magnitude. Their components will relate to the Equation (2.10) through:

$$p_r = p_{r_D} + p_{r_{J_2}} \tag{2.11a}$$

$$p_s = p_{s_D} + p_{s_{J_2}} \tag{2.11b}$$

$$p_w = p_{w_D} + p_{w_{J_2}} \tag{2.11c}$$

2.2.1.1 Drag

The drag ($\mathbf{D}$) is a force acting opposite to the satellite's velocity $\mathbf{v}$. If the velocity of the atmosphere due to the rotation of the Earth is ignored, one can write:

$$\mathbf{D} = -D\hat{\mathbf{v}} = \frac{1}{2}\varrho v^2 C_D A \hat{\mathbf{v}}, \tag{2.12}$$

where D is the drag magnitude, $\hat{\mathbf{v}}$ is the unitary velocity vector, ϱ is the atmospheric density, v is the velocity's magnitude, C_D is the dimensionless drag coefficient, and A is the satellite's frontal area. Usually, for C_D is assumed the constant value of 2.2 over the entire orbital lifetime, though the theory agrees it is variable (HANEVEER, 2017). Dividing the previous equation by the mass of the spacecraft, the drag acceleration is:

$$\mathbf{p}_D = \mathbf{D}/m = -\frac{1}{2}\varrho v \left(\frac{C_D A}{m}\right)\mathbf{v}, \tag{2.13}$$

where the parameter between parenthesis is also recognized as the ballistic coefficient, and m is the mass of the CubeSat.

The components of a perturbation with magnitude p_D aligned with the velocity vector of the satellite in the LVLH reference frame are (CURTIS, 2014):

$$p_{r_D} = p_D \frac{\mathbf{v}}{v}.\hat{\mathbf{r}} = \frac{p_D}{v} v_r = \frac{p_D}{v}\frac{\mu e \sin(\theta)}{h} \tag{2.14a}$$

$$p_{s_D} = p_D \frac{\mathbf{v}}{v}.\hat{\mathbf{s}} = \frac{p_D}{v} v_s = p_{s_D} = \frac{p_D}{v}\frac{h}{r} \tag{2.14b}$$

$$p_{w_D} = p_D \frac{\mathbf{v}}{v}.\hat{\mathbf{w}} = 0 \tag{2.14c}$$

Recognizing that the drag perturbation is also tangent to the orbit and opposite to the velocity vector, the parameter p_D is:

$$p_D = -\frac{1}{2}\varrho v^2 \left(\frac{C_D A}{m}\right) \tag{2.15}$$

where the magnitude of the velocity is (CURTIS, 2014):

$$v = \frac{\mu}{h}\sqrt{\left(\sin\left(\theta\right)\right)^2 + \left(e + \cos\left(\theta\right)\right)^2} \tag{2.16}$$

Therefore, the components of the drag perturbation in the LVLH are:

$$p_{r_D} = -\frac{1}{2h}\mu e \varrho v \left(\frac{C_D A}{m}\right)\sin\left(\theta\right) \tag{2.17a}$$

$$p_{s_D} = -\frac{1}{2r} h \varrho v \left(\frac{C_D A}{m}\right) \tag{2.17b}$$

$$p_{w_D} = 0 \tag{2.17c}$$

2.2.1.2 Gravitational perturbation

The components of the J_2 gravitational perturbation in the LVLH components are given by Equation (2.18). Further details can be found in Curtis (2014).

$$p_{r_{J2}} = -\frac{3}{2}\frac{J_2 \mu R_E^2}{r^4}\left[1 - 3\sin^2\left(i\right)\sin^2\left(\omega + \theta\right)\right] \tag{2.18a}$$

$$p_{s_{J2}} = -\frac{3}{2}\frac{J_2 \mu R_E^2}{r^4}\sin^2\left(i\right)\sin\left[2\left(\omega + \theta\right)\right] \tag{2.18b}$$

$$p_{w_{J2}} = -\frac{3}{2}\frac{J_2 \mu R_E^2}{r^4}\sin\left(2i\right)\sin\left(\omega + \theta\right) \tag{2.18c}$$

2.2.2 Gauss's variational equations

The model used in this work for the dynamic behavior of the Classical Orbital Elements bases on Gauss's variational equations (BATE; MUELLER; WHITE, 1971; CURTIS, 2014). The development can be found in Curtis (2014), and basically consists of obtaining the COE from the state-vector and then finding the rates. The rate equations are:

$$\frac{dh}{dt} = r p_s \tag{2.19a}$$

$$\frac{de}{dt} = \frac{h}{\mu}\sin\left(\theta\right)p_r + \frac{p_s}{\mu h}\left[\left(h^2 + \mu r\right)\cos\left(\theta\right) + \mu e r\right] \tag{2.19b}$$

$$\frac{d\theta}{dt} = \frac{h}{r^2} + \left[\frac{h^2\cos\left(\theta\right)}{\mu e h}p_r - \left(r + \frac{h^2}{\mu}\right)\frac{\sin\left(\theta\right)}{eh}p_s\right] \tag{2.19c}$$

$$\frac{d\Omega}{dt} = \frac{r}{h\sin\left(i\right)}\sin\left(\omega + \theta\right)p_w \tag{2.19d}$$

$$\frac{di}{dt} = \frac{r}{h}\cos\left(\omega + \theta\right)p_w \tag{2.19e}$$

$$\frac{d\omega}{dt} = -\frac{1}{eh}\left[\frac{h^2}{\mu}\cos(\theta)\,p_r - \left(r + \frac{h^2}{\mu}\right)\sin(\theta)\,p_s\right] - \frac{r\sin(\omega+\theta)}{h\tan(i)}p_w \tag{2.19f}$$

Notice that singularities arise when $e = 0$ or $i = 0°$, the consequence of assuming that the position vector used in the above equations is the solution of an elliptic orbit (SCHAUB; JUNKINS, 2014).

The orbit model is a problem of initial value, essentially summarized by Equations (2.5), (2.6), (2.8) and (2.19), whose ordinary differential equations of COE are of first order. Therefore, one can write:

$$\dot{\mathbf{c}} = \mathbf{f}(t, \mathbf{c}) \tag{2.20}$$

where $\mathbf{c}$ and $\dot{\mathbf{c}}$ are the COE vector and its derivative, respectively. The COE at the initial time (t_0) is given by the user, as explained previously. The user still has to inform the timestep (Δt) between iterations and the final time (t_f) of the simulation.

2.2.2.1 Position of the Sun

Before proceeding to the attitude model, the position of the Sun has to be calculated. It does not impact orbit determination, but it will be necessary to define specific attitudes and compute the eclipse caused by the Earth. To compute the solar vector $\mathbf{r}_{sun}$, the following equations will be used, available at Curtis (2014).

$$JD = 367\text{year} - \left\lfloor\frac{7\text{year} + \left\lfloor\frac{\text{month}+9}{12}\right\rceil}{4}\right\rceil + \left\lfloor\frac{275\text{month}}{9}\right\rceil + \text{day} + \frac{UT}{24} + 1,721,013.5 \tag{2.21a}$$

$$n_d = JD - 2,451,545 \tag{2.21b}$$

$$M_s = 357.529° + 0.98560023 n_d \tag{2.21c}$$

$$L_s = 280.459° + 0.98564736 n_d \tag{2.21d}$$

$$\Lambda = L_s + 1.915°\sin(M_s) + 0.0200°\sin(2M_s) \tag{2.21e}$$

$$\epsilon = 23.439° - 3.56 \times 10^{-7} n_d \tag{2.21f}$$

$$\hat{u} = \cos(\Lambda)\,\hat{I} + \cos(\epsilon)\sin(\Lambda)\,\hat{J} + \sin(\epsilon)\sin(\Lambda)\,\hat{K} \tag{2.21g}$$

$$r_{sun} = [1.00014 - 0.01671\cos(M_s)] - [0.000140\cos(2M_s)]\,AU \tag{2.21h}$$

$$\mathbf{r}_{sun} = r_{sun}\hat{\mathbf{u}} \tag{2.21i}$$

The idea is to initially compute the Julian day number (JD) using the date input, and the universal time of the initial of the simulation. The next equation gives the number of days since J2000 (n_d). M_s and L_s are the mean anomaly and mean longitude of the Sun, respectively. Λ is the ecliptic longitude, ϵ is the obliquity. Finally, $\hat{u}$ is the unit vector from the Earth to the Sun, and the magnitude of the distance is r_{sun}, where $AU = 149,597,870.691$ km is the astronomical distance.

2.2.3 Attitude model

The attitude model aims to mimic the rotation of the satellite around its axis. For a typical CubeSat 1U, without deployable solar panels, there are six normal vectors that describe the orientation of each side k.

In this work, the initial orientations of these surfaces in the perifocal frame of reference are:

$$\mathbf{n}_{1_0} = [-1, 0, 0] \tag{2.22a}$$

$$\mathbf{n}_{2_0} = [+1, 0, 0] \tag{2.22b}$$

$$\mathbf{n}_{3_0} = [0, -1, 0] \tag{2.22c}$$

$$\mathbf{n}_{4_0} = [0, +1, 0] \tag{2.22d}$$

$$\mathbf{n}_{5_0} = [0, 0, -1] \tag{2.22e}$$

$$\mathbf{n}_{6_0} = [0, 0, +1] \tag{2.22f}$$

To define the attitude, the user will have to write the rotation matrices, which are functions of an angle and axis of rotation, and combine them for different scenarios. The initial set of rotations are executed in the perifocal frame of reference and, if necessary, later translated to the geocentric frame of reference. For all of them, $\mathbf{N}_k$ means the final orientation of surface k after all the rotations performed at instant t, in the geocentric reference frame. Some examples to be explored and discussed in this work are illustrated in Figure 13.

Exactly these specific attitudes are difficult to obtain without a precise active attitude control, but yet they are close to typical operation modes as Earth imaging missions, reduced tumbling rate along one major axis, or safe modes where one or more solar panels are exposed to the Sun for battery's recharge (XIAO et al., 2015; PHAM et al., 2015).

2.2.3.1 Nadir

In this case, the satellite always keeps the same attitude towards the Earth's center (Figure 13a). For this case, the satellite only rotates around the $\hat{\mathbf{w}}$ axis, whose angle of rotation is the same as the true anomaly θ:

$$[Q]_{nad} = \begin{bmatrix} \cos(\theta) & \sin(\theta) & 0 \\ -\sin(\theta) & \cos(\theta) & 0 \\ 0 & 0 & 1 \end{bmatrix} \tag{2.23}$$

Therefore, as the satellite must follow the orbit inclination, it is necessary to transform from the perifocal to the geocentric reference frame:

$$\mathbf{N}_k = [Q]^{\intercal}_{X\bar{x}} [Q]_{nad} \mathbf{n}_{k_0} \tag{2.24}$$

Figure 13 – Attitude scenarios

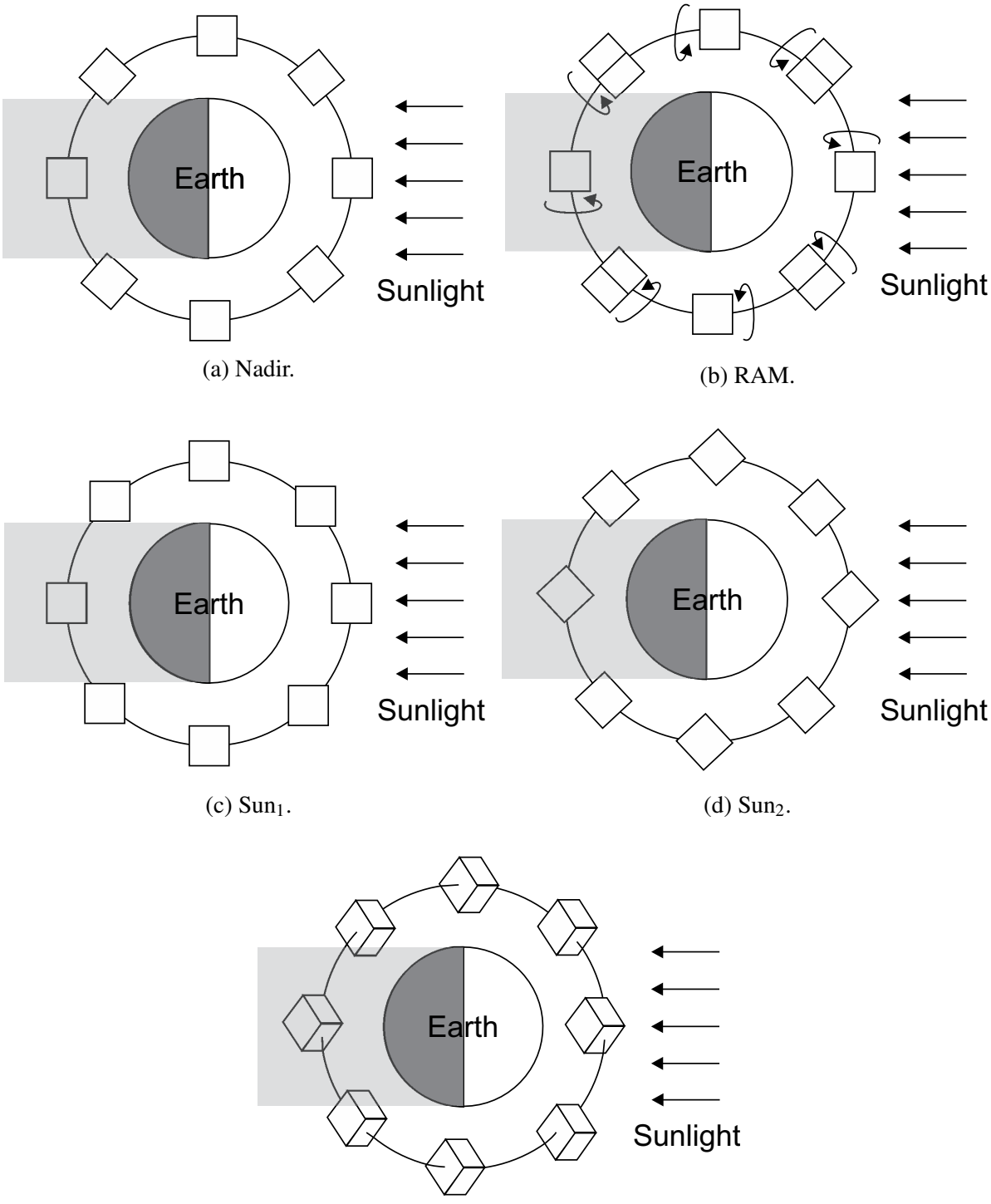

(a) Nadir.

(b) RAM.

(c) Sun_1.

(d) Sun_2.

(e) Sun_3.

Source: The author

If the satellite keeps the same face towards the Earth, but has a residual rotation Θ that

causes a detumbling, the rotation matrix can be:

$$[Q]_{nadir,2} = [Q]_{nad} \begin{bmatrix} 1 & 0 & 0 \\ 0 & \cos(\Theta) & \sin(\Theta) \\ 0 & -\sin(\Theta) & \cos(\Theta) \end{bmatrix} \tag{2.25}$$

Therefore, the orientation is:

$$\mathbf{N}_k = [Q]^{\intercal}_{X\bar{x}} [Q]_{nadir,2} \mathbf{n}_{k_0} \tag{2.26}$$

2.2.3.2 RAM

Another example with the nadir matrix is the RAM attitude (Figure 13b). In this case, the satellite keeps one of its axis aligned with the satellite's velocity vector, or in other words, it will rotate around the $\hat{\mathbf{w}}$ axis once per orbit, as in the nadir attitude. If the satellite has a residual angular speed Θ along its velocity vector, the resulting rotation matrix is:

$$[Q]_{ram} = [Q]_{nad} \begin{bmatrix} \cos(\Theta t) & 0 & -\sin(\Theta t) \\ 0 & 1 & 0 \\ \sin(\Theta t) & 0 & \cos(\Theta t) \end{bmatrix} \tag{2.27}$$

Again, the satellite must follow the orbit inclination, so:

$$\mathbf{N}_k = [Q]^{\intercal}_{X\bar{x}} [Q]_{ram} \mathbf{n}_{k_0} \tag{2.28}$$

2.2.3.3 Sun-fixed

Another option is to keep the attitude fixed in the space, for example, towards the Sun, an important case to maximize the photovoltaic energy generation through solar panels of the satellite. In this case, diverse scenarios may be interesting. For example, only one side of the CubeSat (Sun_1), two (Sun_2) or three (Sun_3) equally exposed to the Sun, as shown in Figure 13c, 13d and 13e, respectively. For all of these scenarios, the rotation matrix is constant, and the transformation from the perifocal to the geocentric reference frame is not necessary.

The first step is to find a unitary vector perpendicular to the Sun, in the Earth's equatorial plane, by performing a rotation of components $\hat{u}_1$, $\hat{u}_2$ (Equation (2.21)) and $\hat{u}_3 = 0$ around the $\hat{K}$ axis, resulting in the vector $\hat{u}_\perp$. After that, the CubeSat's normal vectors are rotated around the $\hat{u}_\perp$ by the angle Θ_1 through the formulation of a rotation matrix around an arbitrary axis (FILHO et al., 2020):

$$\Theta_1 = \cos^{-1}\left(\frac{\hat{u}_3.\hat{K}}{\hat{u}}\right) + \Theta_{s,1} \tag{2.29}$$

The first part on the right side is the angle between the solar vector and the $\hat{K}$ axis to place the sides of the CubeSat parallel to the Earth's equatorial plane. The second term ($\Theta_{s,1}$) tilts the CubeSat even more if the user wants to. The following step is to rotate the CubeSat's normal around the $\hat{K}$ axis and angle Θ_2 to orientate it towards the Sun. The angle is between $\hat{u}_{\perp,1}$ axis and $\hat{I}$:

$$\Theta_2 = \cos^{-1}\left(\frac{\hat{u}_{\perp_1}.\hat{I}}{\hat{u}_{\perp}}\right) \tag{2.30}$$

Finally, the last rotation will be around the $\hat{J}$ axis, by the angle $\Theta_{s,3}$. The above procedure will result in one face towards the Sun, two equally projected or three equally projected, valid for the attitude here called Sun_1, Sun_2 and Sun_3, respectively, as shown in Figure 13. The values for $\Theta_{s,1}$ and $\Theta_{s,3}$ in each condition are:

- Sun_1: $\Theta_{s,1} = 0°$, $\Theta_{s,3} = 0°$;
- Sun_2: $\Theta_{s,1} = 0°$, $\Theta_{s,3} = 45°$;
- Sun_3: $\Theta_{s,1} \approx 35.2643°$, $\Theta_{s,3} = 45°$;

$$\mathbf{N}_k = [Q]_{sun}\,\mathbf{n}_{k_0} \tag{2.31}$$

2.2.4 Irradiance model

2.2.4.1 Thermal radiation

Every object above the absolute temperature (0 K) emits thermal radiation, an electromagnetic phenomenon where the heat transfer that nor require material to exist neither a thermal gradient, opposed to the convection and conduction heat exchange (BERGMAN et al., 2011). The emission of radiation is spectral, or in other words, depends on the wavelength, as illustrated in Figure 14. The thermal radiation comprehends mostly the interval between 0.1 to 100 μm, a range that affects the temperature of matter (BERGMAN et al., 2011).

The thermal radiation also can be directional, with angle dependence, so the object can have surface properties with preferable directions related to heat transfer by radiation, as illustrated by Figure 15.

Equation (2.32) is the Planck Distribution and gives the spectral emissive power for a black-body ($E_{\lambda,b}$), the superior limit of radiation that a body can emit. In this equation, C_1 and

Figure 14 – Spectrum of electromagnetic radiation

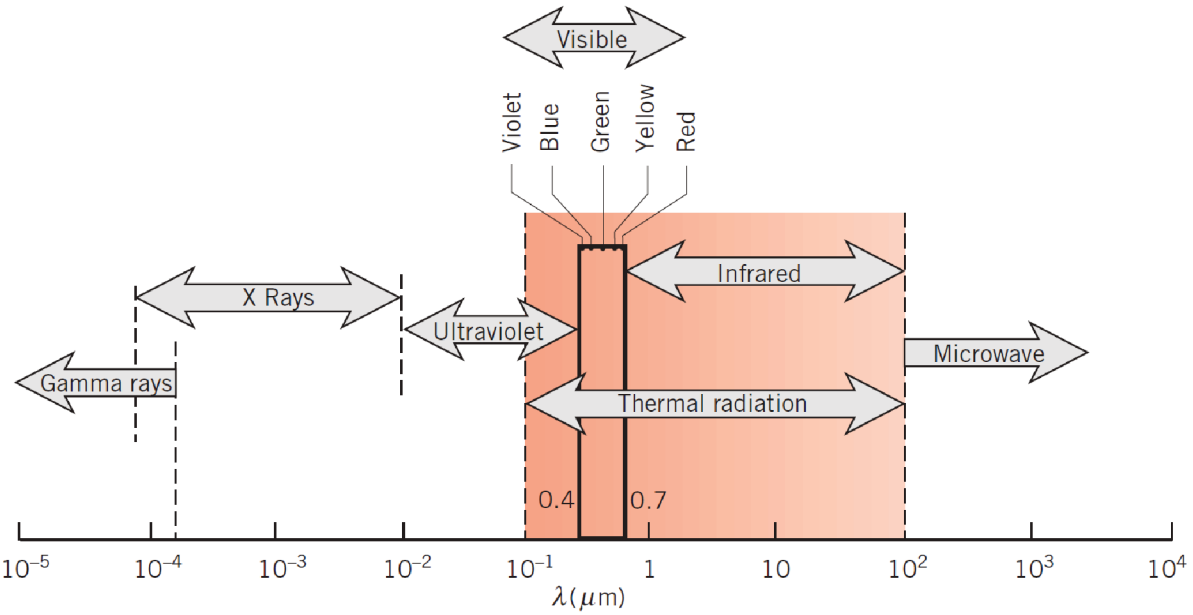

Source: Bergman et al. (2011)

Figure 15 – Directional distribution

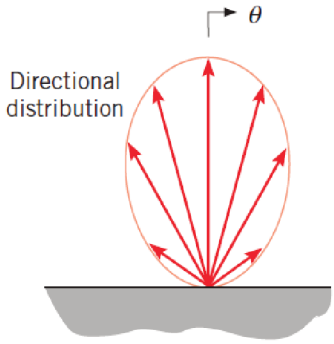

Source: Bergman et al. (2011)

C_2 are constants, λ is the wavelength and T is the temperature. It is important to mention that the black-body is an idealization and absorbs all the incident radiation in all directions by definition.

$$E_{\lambda,b}(\lambda, T) = \frac{2\pi C_1}{\lambda^5 \left(\exp^{\frac{C_2}{\lambda T}} - 1\right)} \tag{2.32}$$

This equation's plot is in Figure 16, where it is shown that each temperature has a peak of emission. The rise of temperature reduces the magnitude, while the peak wavelength shifts to the right.

The maximum value of Equation (2.32) can be obtained through Equation (2.33), also

Figure 16 – Spectral blackbody emissive power

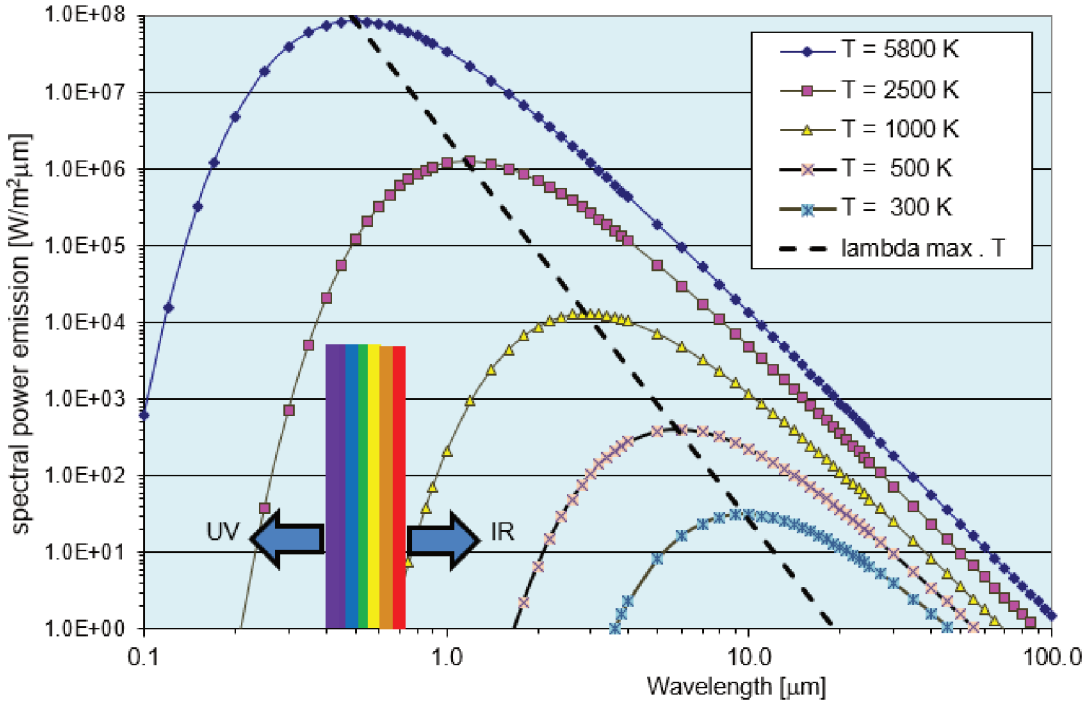

Source: The Author

known as Wien's Displacement Law.

$$\lambda_{max} T = C_3 \tag{2.33}$$

where C_3=2898 μmK. Therefore, the solar emission under 5800 K has a peak of 0.5 μmK, while the Earth emits around 255 K, and the peak is 11.4 μmK.

The integration of Equation (2.32) over all the wavelengths originates the total emissive power of a black body:

$$E_b(T) = \int_0^\infty E_{\lambda,b}(\lambda, T)\, d\lambda = \sigma T^4 \tag{2.34}$$

where σ is the Stefan-Boltzmann constant. This equation estimates the amount of radiation emitted in all directions and all wavelengths by a black-body at temperature T.

Nevertheless, real bodies can not absorb or emit the radiation totally, only a fraction of it. A surface without transmissivity is opaque. For a condition where the emission and absorption are independent of the wavelength, the surface is named gray. A surface without direction dependence is known as diffuse. In this work, the surfaces will be opaque and diffuse, and their radiative properties will be described by:

- Absorptivity α: Absorbed radiation over total incident radiation;

- Reflectivity ρ: Reflected radiation over total incident radiation;
- Emissivity ε: Emitted radiation over the black-body emission.

2.2.4.2 Irradiation sources

For CubeSats in LEO, the main irradiance sources are from the Sun (Q_{sun}), the albedo (Q_{alb}), and the Earth (Q_e) (GILMORE; DONABEDIAN, 2002).

The solar irradiance reaching the external surfaces k of the CubeSat is:

$$Q_{sun_k} = G_{sun} A_k F_{k \to sun} \xi \tag{2.35}$$

The parameter G_{sun} is the solar flux (1367 W/m^2), A_k is the area of the surface k, $F_{k \to sun}$ is the view factor of surface k towards the Sun, and ξ is a variable to express the shadow of the earth. The dot product estimates the view factor:

$$F_{k \to sun} = \mathbf{N}_k \cdot \frac{\mathbf{r}_{sun}}{|\mathbf{r}_{sun}|} \tag{2.36}$$

To compute the shadow of the Earth, one initial task is to locate the Sun's vector ($\mathbf{r}_{sun}$), already performed in Equation (2.21). Once the Sun's vector is determined, Equation (2.37) is used to verify if the CubeSat is under the Earth's shadow, based on Figure 17. Notice the shadow is assumed to have a cylindrical shape.

Figure 17 – Diagram to estimate the shadow

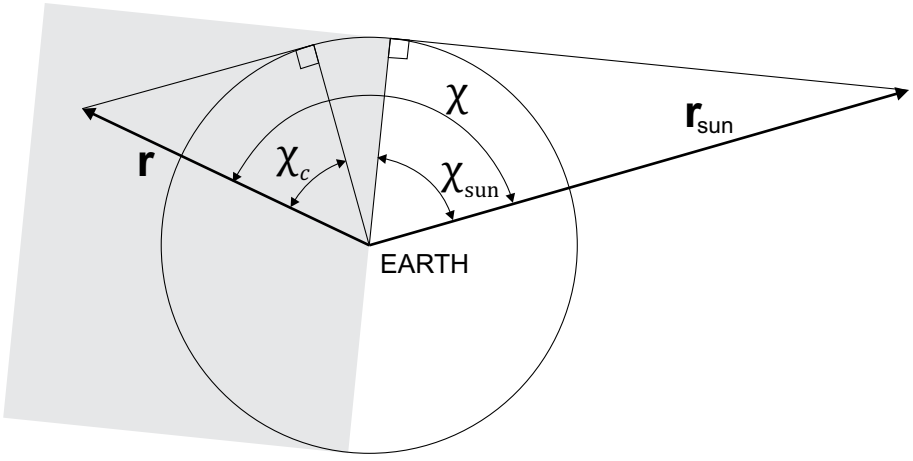

Source: The author

$$\chi_c = \cos^{-1}\left(\frac{R_E}{|\mathbf{r}|}\right) \tag{2.37a}$$

$$\chi_{sun} = \cos^{-1}\left(\frac{R_E}{|\mathbf{r}_{sun}|}\right) \tag{2.37b}$$

$$\chi = \cos^{-1}\left(\frac{\mathbf{r}.\mathbf{r}_{sun}}{|\mathbf{r}||\mathbf{r}_{sun}|}\right) \tag{2.37c}$$

$$\xi = \begin{cases} 0, & \chi_c + \chi_{sun} \leq \chi \\ 1, & \text{otherwise} \end{cases} \tag{2.37d}$$

The equation for the albedo irradiation is:

$$Q_{alb_k} = bG_{sun}A_kF_{k\to e}\psi \tag{2.38}$$

b is the albedo coefficient, $F_{k\to e}$ is the view factor of surface k towards the Earth, calculated by Equation (2.39) and based on Figure 18, and ψ the Earth's area projection towards the solar rays.

Figure 18 – Geometry to estimate $F_{k\to e}$

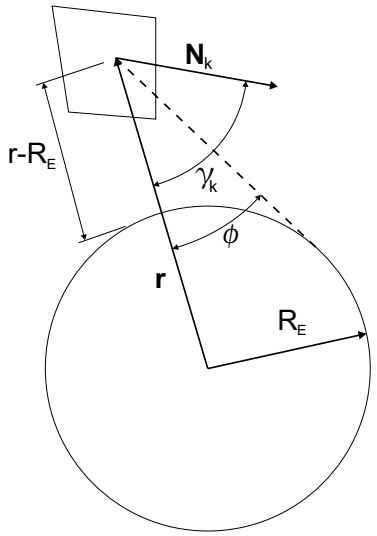

Source: Adapted from Richmond (2010)

$$F_{k\to e} = \begin{cases} \frac{\cos(\gamma_k)}{H^2}, & \gamma_k \leq \pi/2 - \phi \\ \frac{1}{2} - \frac{2}{\pi}\left(W_1 - W_2\right), & \frac{\pi}{2} - \phi \leq \gamma_k \leq \frac{\pi}{2} + \phi \\ 0, & \text{otherwise} \end{cases} \tag{2.39a}$$

$$\gamma_k = \cos^{-1}\left(-\frac{\mathbf{N}_k.\mathbf{r}}{|\mathbf{N}_k|\,|\mathbf{r}|}\right) \tag{2.39b}$$

$$\phi = \sin^{-1}\left(\frac{1}{H}\right) \tag{2.39c}$$

$$H = \frac{r}{R_E} \tag{2.39d}$$

$$W_1 = \frac{1}{2}\left[\sin^{-1}\left(\frac{\sqrt{H^2-1}}{H\sin(\gamma_k)}\right)\right] \tag{2.39e}$$

$$W_2 = \frac{1}{2H^2}\left\{ \cos(\gamma_k)\cos^{-1}\left[-\sqrt{H^2-1}\cot(\gamma_k)\right]\right\} - \frac{1}{2H^2}\left\{\sqrt{H^2-1}\sqrt{1-H^2\left[\cos(\gamma_k)\right]^2}\right\} \tag{2.39f}$$

The parameter ψ in Equation (2.38) models the Earth's area projection towards the solar rays, as summarized by Equation (2.40).

$$\psi = \begin{cases} \cos(\chi), & \chi \in [0, \pi/2] \\ 0, & \chi > \pi/2 \end{cases} \tag{2.40}$$

The other source of irradiation comes from the Earth, calculated by Equation (2.41), where G_e is the heat flux from the Earth (237 W/m^2).

$$Q_{e_k} = G_e A_k F_{k\to e} \tag{2.41}$$

Therefore, the sum of all main irradiation is:

$$Q_{tot} = \sum_{k=1}^{6} Q_{sun_k} + Q_{alb_k} + Q_{e_k} \tag{2.42}$$

It is important to highlight that this is the total amount of radiation reaching the satellite. However, it may not be totally converted into heat if the satellite absorbs only a fraction of it. The parameter α is the absorption of thermal radiation, and in the following chapters, its value will be introduced.

To summarize, the procedure explained in this work is dedicated to the following scenarios:

- Orbit around the Earth;
- Non-circular and non-equatorial orbits;
- Orbits in LEO, below 600 km, since only the drag and gravitational perturbations are assumed;
- Constant ballistic coefficient;
- CubeSat geometry of any size, without deployable parts.

2.2.4.3 β angle

As seen before, the Sun is the most important source for satellite's thermal problems. Adding the fact that satellites may spend a fraction of the orbit under the Earth's shadow, the orientation of the orbit towards the Sun is an important parameter to predict the temperature in

orbit. This is accomplished by the β angle, which defines the minimum angle between the orbit plane and the solar vector, according to the next equation (GILMORE; DONABEDIAN, 2002):

$$\beta = \sin^{-1}\left(\cos\left(\Gamma\right)\sin\left(\Omega\right)\sin\left(i\right) - \sin\left(\Gamma\right)\cos\left(\epsilon\right)\cos\left(\Omega\right)\sin\left(i\right) + \sin\left(\Gamma\right)\sin\left(\epsilon\right)\cos\left(i\right)\right) \quad (2.43)$$

where Γ is the ecliptic true solar longitude, Ω is the right ascension angle of the orbit, ϵ is the ecliptic, and i the orbit's inclination.

The orbit has the longest eclipse when $\beta = 0°$ and none for $\beta = 90°$. However, an orbit without eclipse is achieved even below 90°, as calculated by the following equation for the eclipse fraction (GILMORE; DONABEDIAN, 2002):

$$f_E = \begin{cases} \frac{1}{180°}\cos^{-1}\left[\frac{\sqrt{(r-R_E)^2+2R_E(r-R_E)}}{r\cos(\beta)}\right], & \text{if } |\beta| < \beta^* \\ 0, & \text{otherwise} \end{cases} \quad (2.44)$$

where r is the magnitude of the vector from the Earth's center to the satellite's center, and β^* is:

$$\beta^* = \sin^{-1}\left(\frac{R_E}{r}\right) \quad (2.45)$$

2.3 CASE STUDY

To demonstrate the capabilities of the proposed methodology, this work will simulate the two TLEs of Table 2. They were obtained from the Celestrak database, valid for the CubeSat PropCube-2 (TLE1) launched from ISS and the CubeSat NORBI (TLE2). The beginning of the simulation starts at 00:00 am, in 1st of January 2015.

Table 2 – TLE input for simulation

Case	i	Ω	e	ω	M	n
TLE1	51.63	142.83	0.00026	168.63	191.47	15.451
TLE2	97.66	233.92	0.00187	147.99	212.25	15.033

Source: The author

The orbit dynamic of these TLEs will be tested with two atmospheric models: the *US Standard Atmosphere 1976* (CURTIS, 2014) and the *NRLMSISE-00* (MAHOOTI, 2010), here referred as USSA76 and NRLMSISE-00, respectively. Finally, the simulations consider the five scenarios of attitude shown in Figure 13. For the attitude RAM, the speed around the velocity vector will be four rotations per orbit. Finally, the results are valid for a CubeSat geometry with solar panels covering all the external surfaces of the satellite, without deployable parts.

2.3.1 Results

To highlight the importance of β angle, or in other words the orbit orientation, Figure 19 summarizes the average irradiance flux and eclipse fraction as a function of the β, for two altitudes. As expected, the lowest value of β gives the minimum flux and the most significant amount of eclipse. However, the maximum irradiance flux is not at $\beta = 90°$ because it results from solar and albedo radiation, this last reducing as the CubeSat moves away from the subsolar point. The irradiance peak occurs at the minimum β without eclipse, at $\beta = 77.7°$ and $\beta = 68.2°$ for the altitude of 150 km and 500 km, respectively. The influence of altitude in the total average irradiance flux is more evident at lower β values because the eclipse fraction is greater, although the view factor also slightly increases.

Figure 19 – Irradiance sources and eclipse fraction as function of β. The solid lines (—) are valid for the altitude of 500 km and the dashed lines (- -) are for altitude of 150 km

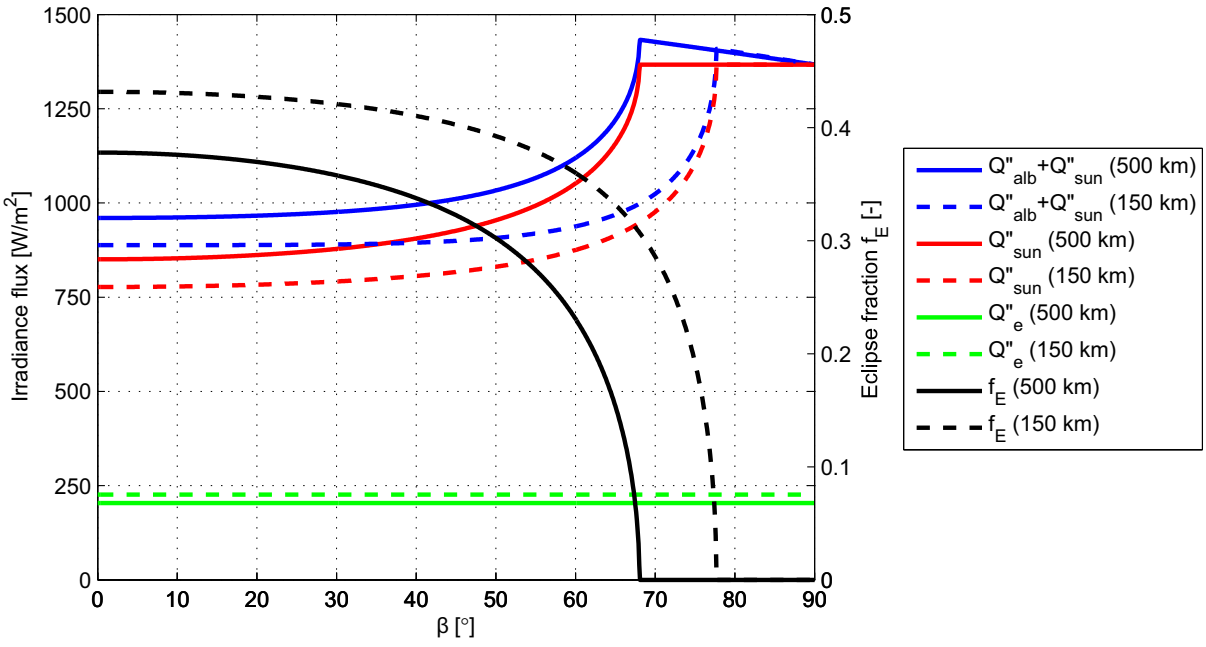

Source: The author

For such scenarios of average irradiance, it is also possible to have an idea of the overall satellite's temperature as a function of β. Figure 20 shows the average temperature for different ratios of absorptivity and emissivity (α/ε), and two altitudes. In this case, it was assumed a hypothetical geometry whose half of the external surface could absorb the incoming radiation. The average temperature increases with β because the eclipse fraction decreases up to the point of $\beta = 77.7°$ and $\beta = 68.2°$, where it vanishes for altitude 150 km and 500 km, respectively. Beyond these points, the temperature slightly reduces because the albedo load decreases as the satellite moves away from the subsolar point. The temperature increases with altitude for a given β because the eclipse fraction is smaller at higher altitudes. This graph also shows that big ratios of α/ε increase the temperature since the satellite easily absorbs the radiation while it poorly

rejects. The opposite happens for low values of α/ε, where the emission of radiation is more significant than its absorption, resulting in lower temperature values.

Figure 20 – Average temperature as function of ratio α/ε and β. The solid lines (—) are valid for the altitude of 500 km and the dashed lines (- -) are for altitude of 150 km

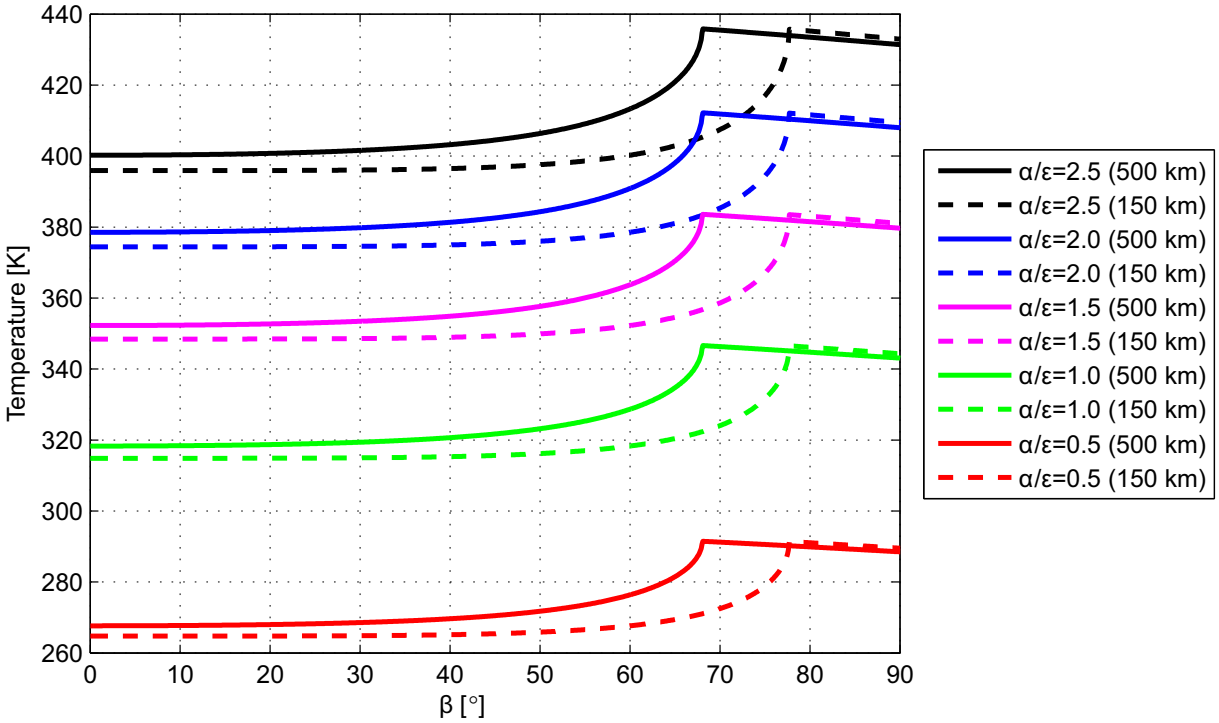

Source: The author

Figure 21 shows the altitude estimation of TLE1 exposed to four different perturbation models. "No perturbation" neglect any form of perturbation, and its result reproduces a perfect horizontal plot, hard to see because it is behind the model "Drag:-,J_2", this without any drag perturbation and only J_2 gravitational perturbation. This last case creates wobbles in the altitude, but the CubeSat does not reduce its altitude permanently. This oscillation is a consequence of short-period variations in the COE, not shown here. When the drag perturbation is introduced, the decay appears. While the orbit's apogee and perigee are noticeable at the beginning of the simulation, around 196 days after and closer to the reentry, the orbit is almost totally circularized. Finally, with the density model NRLMSISE-00, the simulation shows that the CubeSat's lifespan is longer than the previous model, taking 305 days to achieve an altitude of 100 km. This last model is coherent with the orbit life of typical CubeSats launched from the ISS.

The altitude variation of the different perturbation models of this case would have a minor impact in the average irradiance field showed in Figure 19; however, Figure 22 shows that β is strongly affected through the lifespan of the CubeSat. The influence of J_2 perturbation is evident, essentially because it impacts in the rate of the ascending node (Ω), presented in the formulation of β (Equation (2.43)). On the other hand, the influence of drag and, consequently, the altitude decay is negligible.

Figure 21 – Altitude evolution for TLE1 under different perturbation models

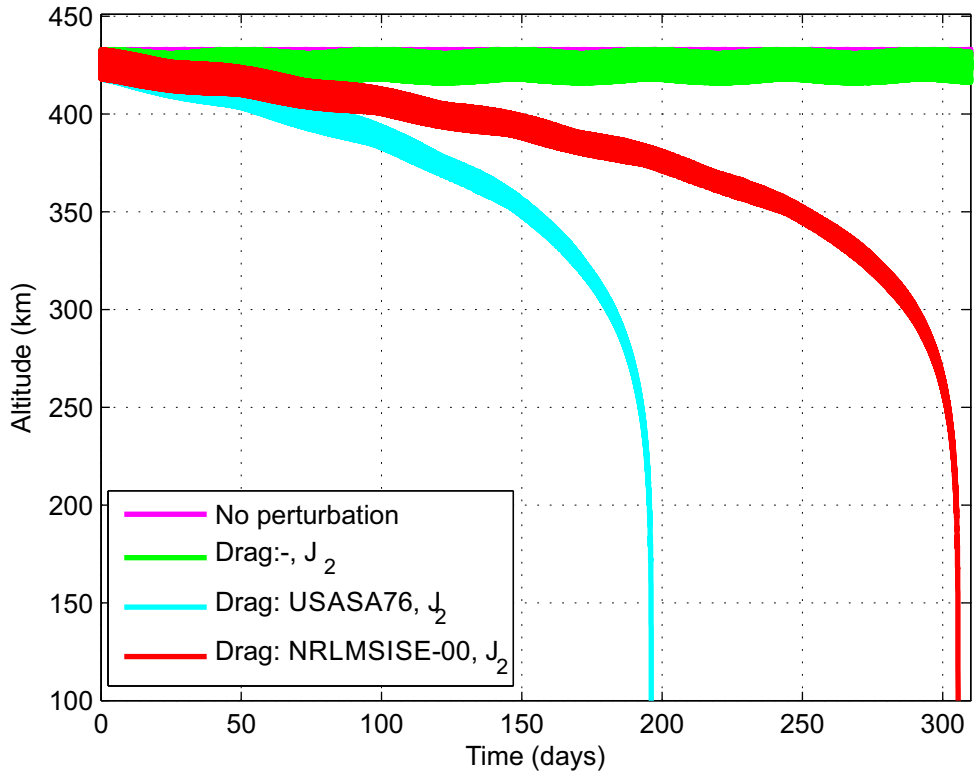

Source: The author

Figure 22 – β angle along one year for TLE1, with different perturbation models

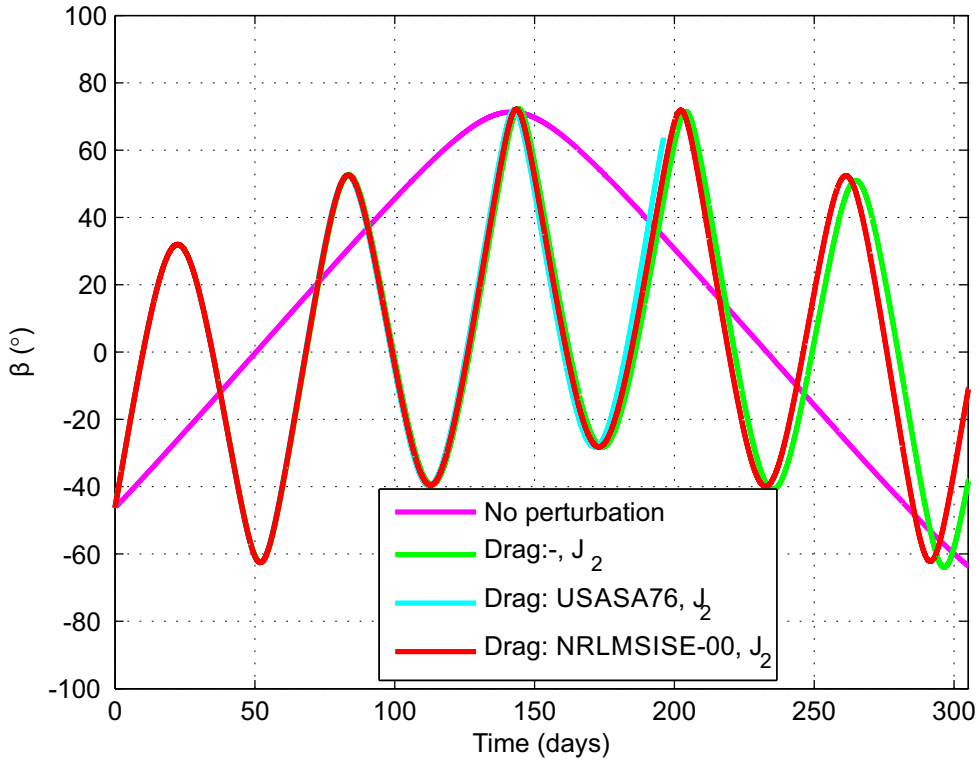

Source: The author

Figure 23 shows the altitude for TLE2 under different scenarios of perturbations and atmospheric models. This case starts with more than 100 km higher than the previous example, and its orbit is even more eccentric. The perigee is still higher than the apogee of TLE1; therefore, this satellite is less exposed to the atmospheric drag in the beginning of the simulation. As a consequence, the total lifespan is greater when compared to the results of TLE1. Again, the atmospheric model based on NRLMSISE-00 results in a longer lifespan than the model USSA76, around 3400 days and 1750 days, respectively.

Figure 23 – Altitude evolution for TLE2 under different perturbation models

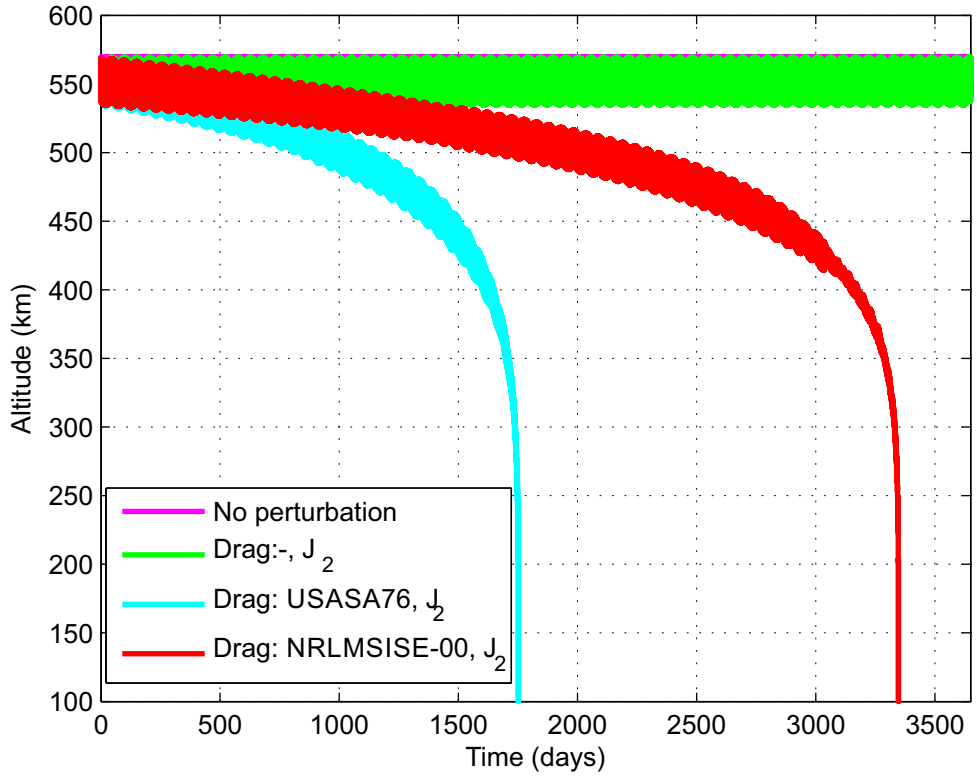

Source: The author

The TLE2 comes from a CubeSat launched into a Sun-synchronous orbit, and the simulations are valid for a CubeSat without thrusters capable of correcting its position. The consequence of this configuration is in Figure 24, where the satellite keeps β around 40° for a year, and then this angle shifts towards other values for all the cases. The cyclic pattern for the case without perturbation highlights the importance of them for Sun-synchronous orbit, a condition where the mission should keep a constant β. When the perturbation J_2 is included, the β variation reduces dramatically and evidences the use of this perturbation to have Sun-synchronous orbits. However, a shift upwards can be explained by the fact that the orbit is eccentric. The orbit inclination that locks β into a single value is a function of altitude, but since the altitude is not constant for this simulation (eccentric orbit), the orbit slowly drifts and changes the β to other ranges. The requirement for correction of the Sun-synchronous mission is even more evident when the drag perturbation is included. In these situations, the altitude's variation

is even more remarkable, and β deviates more from its initial value as far it is from its initial altitude.

Figure 24 – β angle along one year for TLE2, with different perturbation models

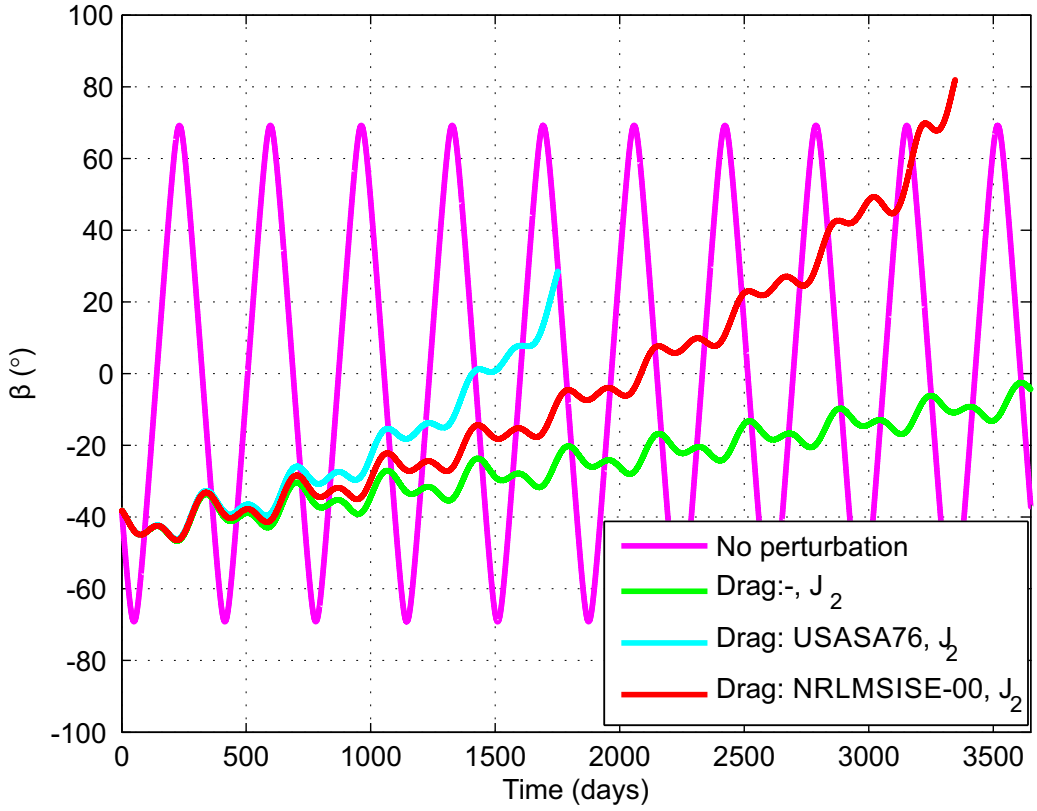

Source: The author

The results from TLE1 obtained with the atmospheric model NRLMSISE-00 will be used in the next results because it brings better relations of accuracy and computational cost (VALLADO; FINKLEMAN, 2014; PICONE et al., 2002). For a particular orbit period with $\beta = 0$ and attitude of Nadir, the total irradiance on each side N_k of a CubeSat defined in Section 2.2.3 is plotted in Figure 25. The gap in the middle of the figure results from the Earth's eclipse, where only the infrared radiation emitted by the Earth hits the surfaces exposed to it. This attitude has a low irradiance level at surfaces N_5 and N_6, a consequence of none solar radiation over them. The sides N_5 and N_6 have the same behavior, and for this reason only one appear in the plot. The opposite sides N_3 and N_4 have the greatest peaks, while the opposite sides N_1 and N_2 would also have it if the eclipse did not cut it from N_2.

This total thermal irradiance is the sum of the incoming solar, albedo, and infrared emission by the Earth. Figure 26 shows the contribution of each one in the sides of the CubeSat, where it is evident the most significant magnitude of the solar radiation, although some sides are not exposed to the Sun. The contribution of albedo may reach around 370 W/m^2 on side 2, a value that can also be significant for photovoltaic simulations because their wavelengths are similar to the solar emission.

Figure 25 – Total irradiance flux for each side of the CubeSat. Orbit with TLE1, $\beta = 0°$, date 10/01/15, 00:00 am, attitude Nadir and perturbation "Drag: NRLMSISE-00, J_2"

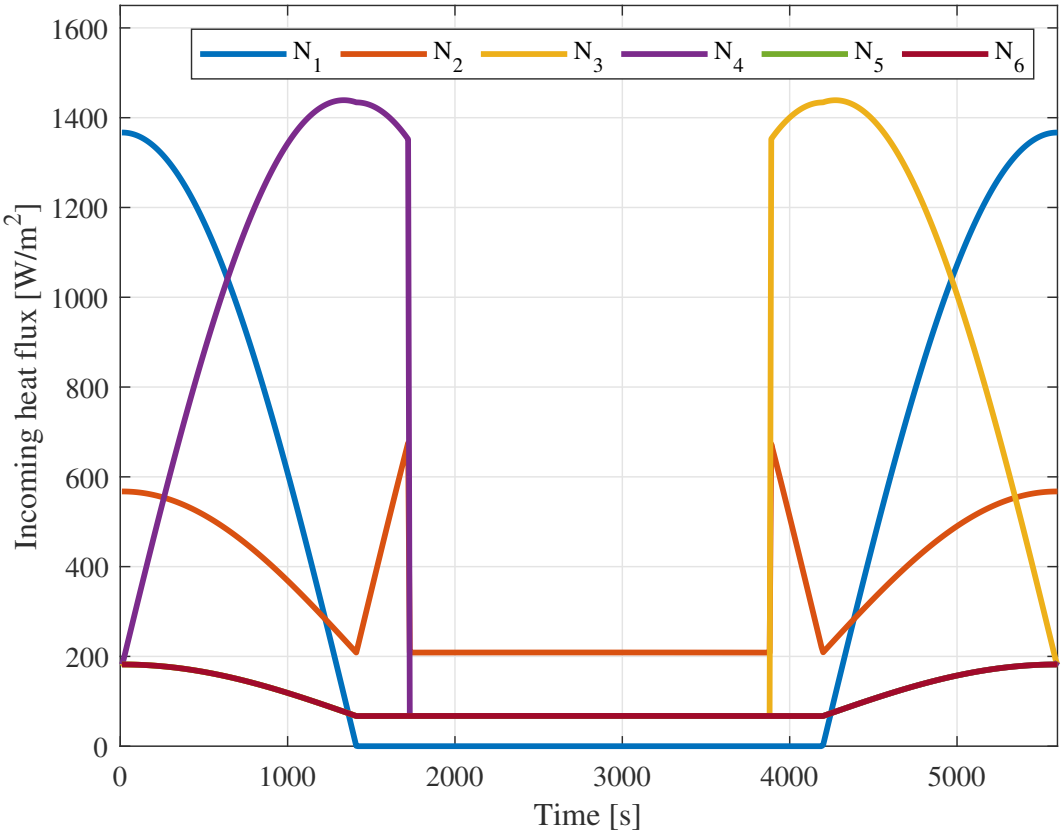

Source: the author

The total irradiance flux in the entire CubeSat is shown in Figure 27a and 27b for the five attitude models discussed earlier, and the extreme conditions of $\beta = 0°$ and maximum $|\beta| = 72°$. Here the importance of β is evident, resulting in the maximum eclipse and absence of it for the same initial COE. The case with $\beta = 0°$ has the greatest peak and variation of irradiation, for a given attitude, compared to the case without an eclipse, consequence of albedo radiation through the orbit. In both scenarios of β, the maximum amount of irradiation is obtained for the attitude Sun_3, where three sides of the CubeSat are equally exposed to the Sun constantly, while the minimum is for attitude Sun_1, where only one surface sees the Sun.

The temperature (T) for the steady-state of a CubeSat 1U with $\alpha/\varepsilon = 1.0$ is plotted in Figure 28, for the same conditions of previous Figure 27. In both cases of β, the temperature follows the total irradiance trend, as it should be specifically for the case of steady-state. The range of values is between 190 K to 325 K, with the minimum only achieved for the orbit with eclipse.

Table 3 summarizes the average temperature values for the entire orbit. Notice that other values are found in Figure 20 for $\beta = 0°$ (318 K for both altitudes) and $\beta = 72°$ (326 K at the

Figure 26 – Irradiation sources on the sides of the CubeSat

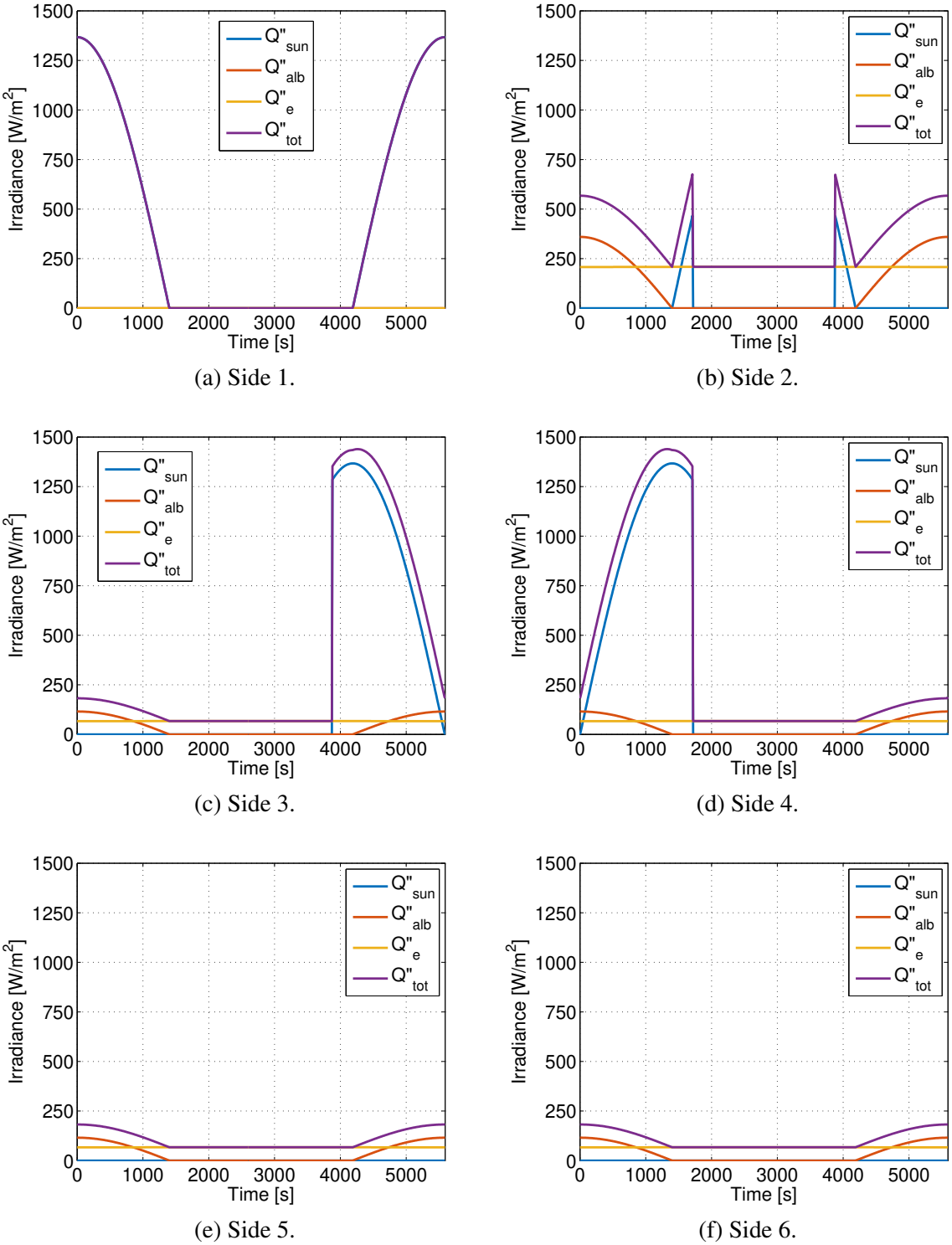

(a) Side 1.

(b) Side 2.

(c) Side 3.

(d) Side 4.

(e) Side 5.

(f) Side 6.

Source: The author

altitude of 150 km and 346 K at 500 km). The reason for such discrepancy relies on the fact that Figure 20 ignores the view factor of surfaces towards the irradiation sources and assumes that half of the satellite's external surface receives radiation; therefore, it overestimates the targeted area regardless of any attitude model. On the other hand, in Figure 28, the area projection is ruled

Figure 27 – Total irradiance flux for each attitude, with TLE1 and perturbation "Drag: NLMSISE-00, J_2"

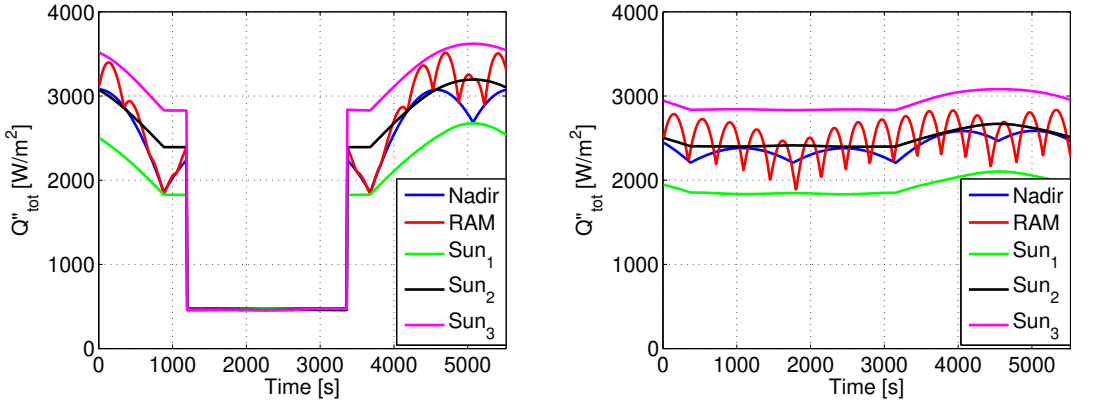

(a) $\beta = 0°$, at 10 days after the initial orbit. (b) $\beta = 72°$, at 143 days after the initial orbit.

Source: The author

Figure 28 – Average temperature at steady-state for each attitude, with TLE1 and perturbation "Drag: NLMSISE-00, J_2"

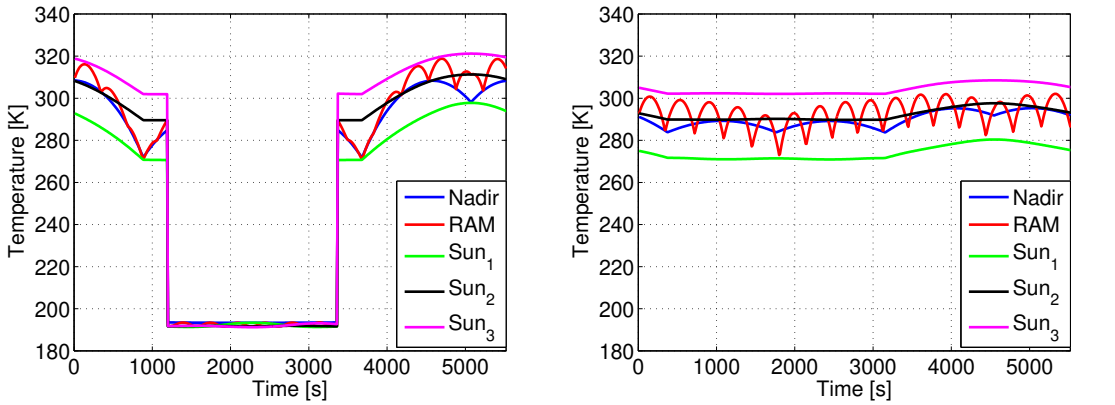

(a) $\beta = 0°$, at 10 days after the initial orbit. (b) $\beta = 72°$, at 143 days after the initial orbit.

Source: The author

by the view factors described earlier for a CubeSat geometry and the corresponding attitude model. Nevertheless, the reader should pay attention that the average temperature in Figure 28 ignored the transient term, an essential parameter for the proper prediction of the temperature along an orbit.

Table 3 – Average temperature of the entire orbit for different attitudes and β

β [°]	Nadir [K]	RAM [K]	Sun_1 [K]	Sun_2 [K]	Sun_3 [K]
0	256	258	248	259	265
72	289	293	274	292	304

Source: The author

2.4 CONSIDERATIONS

Considering the need for engineers to simulate, understand the satellite's behavior in orbit, and minimize failures or an inadequate satellite operation, this chapter presented a numerical tool to explore typical irradiation scenarios for CubeSat missions combining state-of-the-art models. In this sense, three main models were considered to estimate the irradiation flux over a CubeSat, namely an orbit, an attitude, and a radiation source model, including solar, albedo, and infrared emitted by the Earth.

Results showed that the altitude impacts the average irradiance sources; however, the influence of β is more remarkable, especially near before the end of the eclipse. As a consequence of irradiation, the average temperature follows this same tendency, with larger absorptivity over emissivity ratios resulting in hotter scenarios, as expected. A case study for a typical CubeSats' TLE, different perturbations, and five attitudes were presented to illustrate the tool's abilities. Results showed that drag was essential to predict the decay of the satellite with atmospheric model NRLMSISE-00. The inclusion of the J_2 was essential to obtain the orbit orientation towards the Sun through the satellite's lifespan, consequently the solar and albedo flux. The attitude models originated different irradiance scenarios for the CubeSat, reinforcing the importance of this parameter for irradiation estimation, for example, the heat transfer and energy harvesting of satellites. Therefore, from the previous results, it is evident that the orbit dynamic's and attitude proper estimation are crucial.

3 THE FINITE VOLUME METHOD FOR CUBESATS

In this chapter, a code based on the Finite Volume Method for temperature field estimation of a CubeSat 1U is developed. The external boundary conditions of the problem were discussed in the previous chapter, and in this section, the internal heat transfer by radiation will be detailed, as well as the computation of obstructing surfaces and the consequent view factors.

3.1 LITERATURE REVIEW OF THERMAL SIMULATION

Analytical formulations are typical for the initial stages of a CubeSat's development, where a quick estimation of the overall temperature field is obtained and updated repeatedly as more information about the inputs of the model is available. Inevitably, idealizations make it a cheap and fast approach at the expense of accuracy. However, nonlinear terms make it difficult to obtain the analytical solution, and several linearization techniques have been proposed. Intrinsically to analytical solutions is the use of single nodes, a Lumped Parameter Method (LPM) approach, to represent the satellite's entire subsystems and reduce the complexity of heat transfer estimation. Consequently, the conductive and radiative heat transfer among those parts and their interaction are oversimplified by the model's terms. Examples of thermal studies involving CubeSat's heat transfer with analytical approaches are Tsai (2004), Pérez-Grande et al. (2009), Bulut and Sozbir (2015), Anh et al. (2016).

Simulations, on the other hand, provide further insights into the details of the satellite by quite accurate solutions, at the cost of execution time and complexity for implementation (TSAI, 2004). Three of the most known numerical techniques are the Finite Difference Method (FDM), Finite Element Method (FEM), and Finite Volume Method (FVM) (MOUKALLED; MANGANI; DARWISH, 2015). Reyes et al. (2020) present an example of CubeSat's thermal simulation where they develop an algorithm in MATLAB ® based on the FDM and compare the results with the commercial software Thermal Desktop. Kovács and Józsa (2018) conduct a thermal analysis of a nanosatellite through a thermal network approach and the commercial software ANSYS® Workbench built on FEM. Bonnici et al. (2019) has a thermal model based on LPM to study the UoMBSat-1 PocketQube, whose results are compared with the commercial software Ansys® formulated as FEM. Escobar, Diaz and Zagal (2016) also use FEM to explore the best thermal control configuration. Corpino et al. (2015) is another example FEM simulation, implemented by the authors in MATLAB®, where they assess the worst hot and cold orbit. The authors use the Absorption Factors Method for the internal boundary condition, also known as the Gebhart Method (GEBHART, 1961). Filho et al. (2020) simulated different attitudes in the commercial software CFX/ANSYS built on FVM for the worst cold and hot scenarios of a CubeSat 1U.

From all of these thermal simulations, only Corpino et al. (2015) considered radiation heat transfer at the CubeSat's internal boundary condition. However, in their in-house code, the Printed Circuit Boards (PCBs) and the battery were modeled as lumped nodes and therefore did not account for thermal gradients either their geometry. Internally, the information about components' dimensions and position is essential for estimating obstructing surfaces and, consequently, proper heat transfer calculation. Except for the previous work of Filho et al. (2020), none of the mentioned papers have solved the CubeSat temperature through the FVM. One of the main attractions of the FVM is the integration of the governing equation over finite control volumes and its conversion into a system of algebraic equations; therefore, the discretized solution naturally follows the conservative balance (VERSTEEG; MALALASEKERA, 2007).

3.2 METHODOLOGY

CubeSat's temperature results from the radiation loads that it faces in orbit, therefore a function of orbital parameters, attitude, the geometry of the satellite, material, and surface properties. In this chapter, the equations to perform the thermal simulation of a CubeSat will be presented. The focus here is to obtain the CubeSat's transient temperature field through an in-house code valid for a typical CubeSat 1U and based on the FVM. For thermal problems of orbiting spacecraft, a good approximation is a perfect vacuum, so the energy balance does not have the convective term. In this work, the thermodynamic properties are constant, the radiation heat transfer occurs on external and internal satellite surfaces, and heat transfer by conduction exists through the CubeSat's components.

Considering the above, the energy equation is:

$$\varrho c \frac{\partial T}{\partial t} - \kappa \nabla . (\nabla T) - S = 0 \tag{3.1}$$

where ϱ is the density [kg/m^3], c is the heat capacity [J/kg.K], T is the temperature [K], t is the time [s], κ is the thermal conductivity [W/m.K] and S is the source term [W/m^3]. Equation (3.1) is the fundamental equation to be solved in order to find the temperature field, independent of the method to be used. In this work, initially a simple formulation based on the Lumped Parameter Method will be discussed, and later the Finite Volume Method.

3.2.1 Lumped Parameter Method (LPM)

The methodology presented in this section is dedicated to solve Equation (3.1) based on the Lumped Parameter Method (LPM). In the LPM formulation, single points represent each of the CubeSat's main parts, as shown in Figure 29. This model will be applied to solve the temperature field of a CubeSat geometry composed of six solar panels and a battery; for this reason, there are seven points. The thermal radiance modeled in the previous chapter reaches

the external surfaces of the satellite, which are the solar panels. For the internal surfaces of the CubeSat, the heat transfer by conduction and radiation are simplified by a thermal resistance Z. The heat exchange among the solar panels is neglected.

Figure 29 – Domain for the LPM

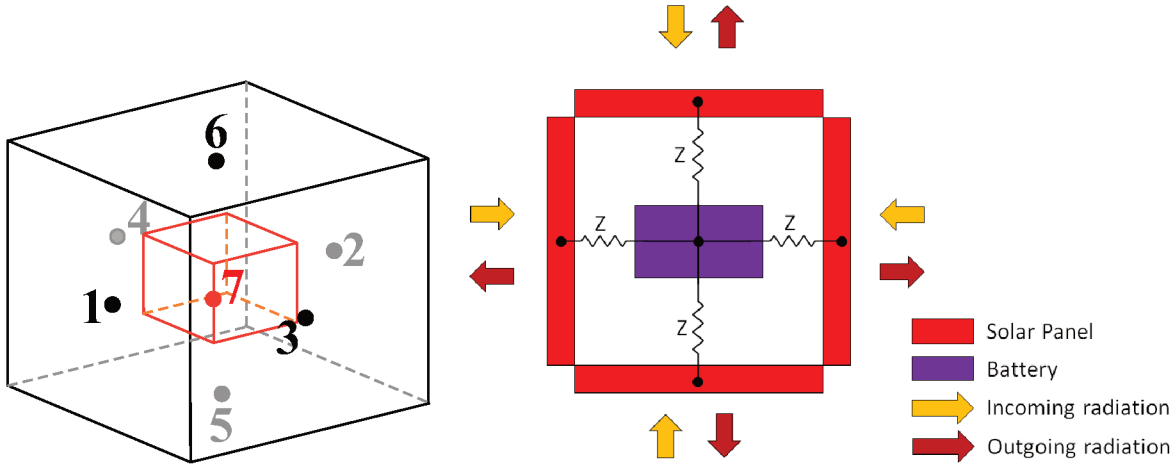

(a) Nodal parts (b) Bi-dimensional view and thermal diagram

Source: The author

To develop the equations, the following assumptions will be assumed in this work:

- The CubeSat has seven main parts, each represented by a subindex w. Solar panels are represented from 1 to 6, while 7 is the battery;
- A photovoltaic panel covers each external side;
- The battery is suspended in the center of the CubeSat;
- Every panel exchanges heat with the battery;
- The solar panels do not exchange heat among themselves;
- The heat transfer by radiation and conduction between the solar panels and battery is proportional to the temperature difference between them and inversely to their thermal resistance Z, according to the Equation (3.4);
- Every Z between the solar panel and battery is identical and constant;
- The value for Z is arbitrary and does not distinguish between radiative or conductive heat transfer;
- Material and surface properties are constant;
- None internal heat generation;

- The irradiance over the external surfaces of the domain comes from the irradiance model developed in the previous chapter.

Over the domain of Figure 29, the classical energy balance (Equation (3.1)) is performed along the CubeSat's orbit, for each node w of the model, resulting in:

$$Q_{r_w} + Q_{Z_w} - \varrho_w V_w c_w \frac{dT_w}{dt} = 0 \tag{3.2}$$

where Q_r is the incoming and outgoing thermal radiation over the nodes, Q_Z the net heat transfer between the solar panel and battery [W], and V is the volume [m^3].

The formulation of incoming radiation for the outer sides of the CubeSat relies on the previous chapter of irradiance modeling, which includes the solar, albedo and infrared radiation of the Earth given by Equations (2.35), (2.38) and (2.41). Only one additional equation is required to close the external boundary condition, given by (BERGMAN et al., 2011):

$$Q_{r_{\text{out}_k}} = \varepsilon_k \sigma A_k \left(T_k^4 - T_\infty^4\right) \tag{3.3}$$

This is the satellite heat exchange by radiation of the external surfaces with the outer space, where ε_w is the emissivity, σ is the Stefan-Boltzmann constant, T_k is the satellite's surface temperature, and T_∞ is the outer space temperature, corresponding to black-body radiation at 2.7 K.

The battery is inside the CubeSat, therefore $Q_{r_7} = 0$. The net heat transfer between parts may occur by conduction and radiation, but this term will be simplified by the following linear equation.

$$Q_{Z_w} = \begin{cases} \frac{T_7 - T_w}{Z} & \text{if } w \leq 6 \\ \sum_{w=1}^{6} \frac{T_w - T_7}{Z} & \text{if } w = 7 \end{cases} \tag{3.4}$$

The time derivative term will be evaluated according to the following finite difference scheme, where Δt is the timestep and "it" the iteration.

$$\frac{dT_w}{dt} \approx \frac{T_w(it) - T_w(it-1)}{\Delta t} \tag{3.5}$$

The Newton-Raphson method can solve the nonlinear system summarized by Equation (3.2), and the user only needs to inform the initial condition and the balance convergence criteria to obtain the solution.

3.2.2 The Finite Volume Method (FVM)

In the FVM, the conservation law ruled by the partial differential (Equation (3.1)) in the continuum domain is integrated over finite control volumes and time. The main advantage of FVM over the LPM formulation is the conservative nature of the integral solution since the flux entering a given volume is identical to leaving the adjacent volume, and the discretization of the domain in more parts (MOUKALLED; MANGANI; DARWISH, 2015).

In this method, the problem's domain is discretized into a finite number of volumes adjacent to each other where the conservation's equations are solved, resulting in three-dimensional solutions rather than single values obtained for each part of the LPM's formulation. By doing that, the numerical solution retains the conservative principle of the physics phenomena.

The integrating of Equation (3.1) over a Control Volume (CV) results in:

$$\int_{CV} \varrho c \frac{\partial T}{\partial t} dV - \int_{CV} \kappa \nabla . \left(\nabla T \right) dV - \int_{CV} S dV = 0 \tag{3.6}$$

The Gauss's divergence theorem transform a volume integral into an area integral, as follows:

$$\int_{CV} \nabla . \vec{L} dV = \int_{A} \vec{L} . d\vec{A} \tag{3.7}$$

where $\vec{L}$ can be any vector.

Therefore, it may be written that:

$$\int_{CV} \varrho c \frac{\partial T}{\partial t} dV - \int_{A} \kappa \nabla T . d\vec{A} - \int_{CV} S dV = 0 \tag{3.8}$$

The integral over time of energy equation energy will result in the next equation, whose challenge is to evaluate each of the terms:

$$\int_{\Delta t} \frac{\partial}{\partial t} \left(\int_{CV} \varrho c T dV \right) dt - \int_{\Delta t} \int_{A} \kappa \nabla T . d\vec{A} dt - \int_{\Delta t} \int_{CV} S dV dt = 0 \tag{3.9}$$

3.2.2.1 The mesh

Before the discretized solutions of the previous integral equation are explained, further details about the discretization are introduced. The domain of this problem is the CubeSat, and the energy conservation rules the physical phenomena of interest. An overview of the domain is in Figure 30. In this case, further details can be added, such as a structure, PCBs, and bolts. The boundary conditions on the external surfaces are the irradiance model of the previous chapter and the satellite's emission of radiation. Simultaneously, there is heat exchange by radiation among the inner surfaces and heat transfer by conduction among the parts.

Figure 30 – Domain for the FVM simulation

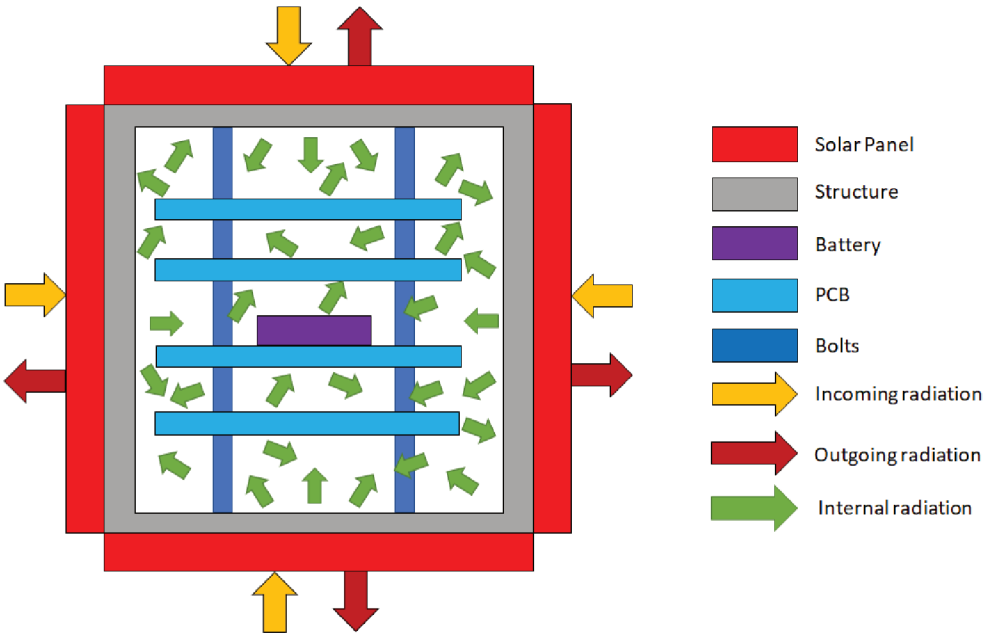

Source: The author

The numerical procedure to solve this problem requires the distribution of nodes in different domain positions, where the dependent variable will be evaluated through a set of algebraic equations that couple every node to its neighbors. Therefore, instead of an exact solution obtained from the partial differential equation, the user will have the discrete answer in specific points. This group of nodes forms the mesh, also referred to as grid (MOUKALLED; MANGANI; DARWISH, 2015).

Figure 31 shows a Control Volume (CV) used to explain the discretization of the equations of this work.

In this three-dimensional orthogonal volume, there are six surfaces identified by north (n), south (s), east (e), west (w), top (t) and bottom (b). The variable of interest (temperature) is located at the center of this volume and represented by P. The neighbor points N, S, E, W, T, B are in the direction of north, south, east, west, top and bottom, respectively.

In this work, the mesh is structured, so each volume has the same quantity of neighbors, and their organization follows a natural order (MALISKA, 2004). The volumes are hexahedral, and they do not overlap. Each node of the mesh is identified by the index i, j and k, for the x, y and z coordinate directions, resulting in a mesh with N_i, N_j and N_k nodes in the index directions i, j and k, respectively (MOUKALLED; MANGANI; DARWISH, 2015).

It is not easy to obtain the intended geometry with a single mesh in some situations, circumstances where the multi-block approach is helpful. For such cases, more meshes are used, and the information among them is transferred to each other through their adjacent boundary conditions along with the iterations, resulting in a multi-block mesh (MALISKA, 2004). In this

Figure 31 – Control volume for application of conservation equations

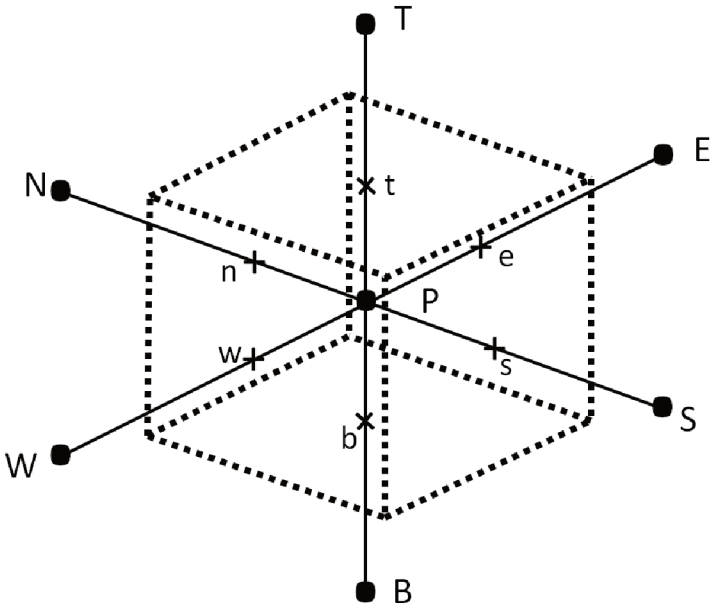

Source: Adapted from Versteeg and Malalasekera (2007)

work, the technique based on non-coincident volumes is applied to exchange the meshes' data. It is assumed that the closest node of the second mesh is the neighbor of node P. Figure 32 illustrates the non-coincident volumes, where the point 2 of Block 1 would be used to exchange information with point P from Block 2, because they have have the shortest distance.

Figure 32 – Non-coincident meshes

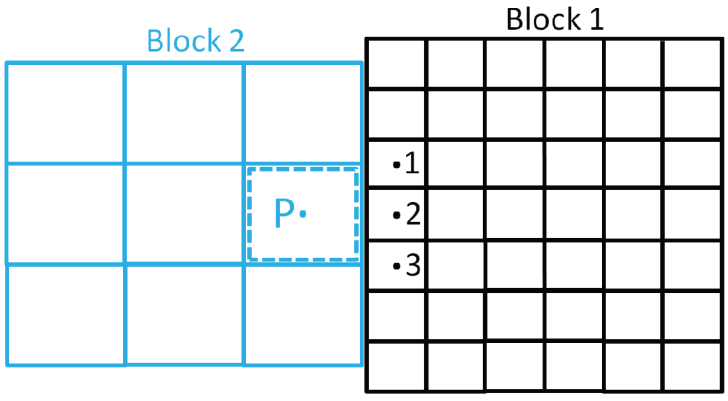

Source: Adapted from Maliska (2004)

Familiarized with these concepts, we can now return to the analysis of Equation (3.9).

3.2.2.2 Equation discretization

The transient term, which represents the time variation of temperature in Equation (3.9), can be written as:

$$\int_{\Delta t} \frac{\partial}{\partial t} \left(\int_{CV} \varrho c T dV \right) dt = \varrho c \left(T_P - T_P^o \right) \Delta V \tag{3.10}$$

The superscript "^{o}" is dedicated to a variable at time t, while the term without it means a variable at time $t + \Delta t$.

The evaluation of remaining terms can be made by two ways: explicit or implicit. For a generic procedure, the time integration may be:

$$I_L \left(T \right) = \int_{\Delta t} l \left(T \right) dt = \left[\theta^* L \left(T \right) + \left(1 - \theta^* \right) L \left(T^o \right) \right] \Delta t \tag{3.11}$$

For $\theta^* = 0$, the model is explicit, and the terms are assessed at time t. For $\theta^* = 1$ the model is fully implicit and the integration occurs for variables at $t + \Delta t$. For any value $0 < \theta^* < 1$, the model is implicit, and the evaluation occurs from a composition of both instants. Specifically for $\theta^* = 1/2$, the model is known as Crank-Nicholson. A model usually applied and used in this work is the fully implicit method because it does not have limits in timestep, although not every timestep will reproduce the correct response (MALISKA, 2004).

The integration over the diffusive term will result in the following equation:

$$\int_{\Delta t} \int_A \left(\kappa \nabla T \right) . d\vec{A} dt = \left[\left(\kappa A \nabla T \right)_e - \left(\kappa A \nabla T \right)_w + \left(\kappa A \nabla T \right)_n - \left(\kappa A \nabla T \right)_s + \right.$$
$$\left. + \left(\kappa A \nabla T \right)_t - \left(\kappa A \nabla T \right)_b \right] \Delta t \tag{3.12}$$

To assess these gradients, the unidimensional volume of Figure 33 is used to explain the central differencing approach.

For this case, the gradients at sides *e* and *w* can be written as:

$$\left(\kappa_e A_e \frac{\partial T}{\partial x} \right) = \frac{\kappa_e A_e}{\delta x_{EP}} \left(T_E - T_P \right) \tag{3.13a}$$

$$\left(\kappa_w A_w \frac{\partial T}{\partial x} \right) = \frac{\kappa_w A_w}{\delta x_{PW}} \left(T_P - T_W \right) \tag{3.13b}$$

In a similar way, the remaining gradients are:

$$\left(\kappa_n A_n \frac{\partial T}{\partial y} \right) = \frac{\kappa_n A_n}{\delta y_{NP}} \left(T_N - T_P \right) \tag{3.14a}$$

Figure 33 – Unidimensional volume and its neighbors

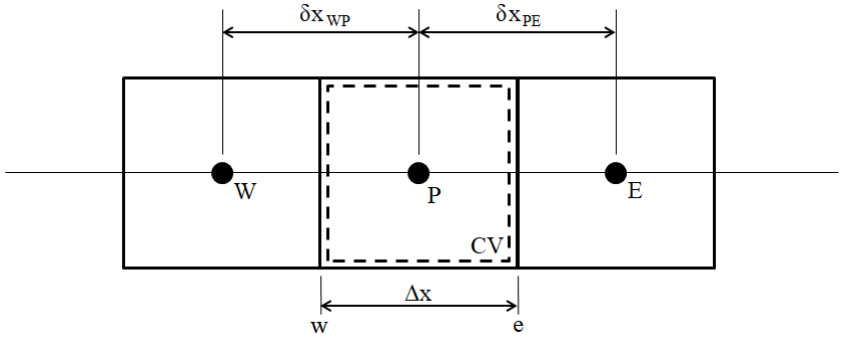

Source: Adapted from Maliska (2004)

$$\left(\kappa_s A_s \frac{\partial T}{\partial y}\right) = \frac{\kappa_s A_s}{\delta y_{PS}} \left(T_P - T_S\right) \tag{3.14b}$$

$$\left(\kappa_t A_t \frac{\partial T}{\partial z}\right) = \frac{\kappa_t A_t}{\delta z_{TP}} \left(T_T - T_P\right) \tag{3.14c}$$

$$\left(\kappa_b A_b \frac{\partial T}{\partial z}\right) = \frac{\kappa_b A_b}{\delta z_{PB}} \left(T_P - T_B\right) \tag{3.14d}$$

Finally, the source term for the fully implicit scheme is described by the following linear equation:

$$\int_{\Delta t} \int_{CV} S dV dt = \bar{S} \Delta V = \left(S_u + S_P T_P\right) \Delta t \tag{3.15}$$

The description of this term as a linear equation improves the convergence of the model (MALISKA, 2004).

By using a central differencing approach for the face fluxes and a fully implicit method, the previous differential of the energy conservation Equation (3.9) becomes the next algebraic equation:

$$\begin{aligned} \varrho c \frac{\Delta V}{\Delta t} \left(T_P - T_P^o\right) - \frac{\kappa_e A_e}{\delta x_{EP}} \left(T_E - T_P\right) + \frac{\kappa_w A_w}{\delta x_{PW}} \left(T_P - T_W\right) - \frac{\kappa_n A_n}{\delta y_{NP}} \left(T_N - T_P\right) \\ + \frac{\kappa_s A_s}{\delta y_{PS}} \left(T_P - T_S\right) - \frac{\kappa_t A_t}{\delta z_{TP}} \left(T_T - T_P\right) + \frac{\kappa_b A_b}{\delta z_{PB}} \left(T_P - T_B\right) - \left(S_u + S_P T_P\right) = 0 \end{aligned} \tag{3.16}$$

Rearranging the terms:

$$\begin{aligned} \left(\frac{\kappa_e A_e}{\delta x_{EP}} + \frac{\kappa_w A_w}{\delta x_{PW}} + \frac{\kappa_n A_n}{\delta y_{NP}} + \frac{\kappa_s A_s}{\delta y_{PS}} + \frac{\kappa_t A_t}{\delta z_{TP}} + \frac{\kappa_b A_b}{\delta z_{PB}} + \varrho c \frac{\Delta V}{\Delta t} - S_P\right) T_P = \\ \frac{\kappa_e A_e}{\delta x_{EP}} T_E + \frac{\kappa_w A_w}{\delta x_{PW}} T_W + \frac{\kappa_n A_n}{\delta y_{NP}} T_N + \frac{\kappa_s A_s}{\delta y_{PS}} T_S + \frac{\kappa_t A_t}{\delta z_{TP}} T_T + \frac{\kappa_b A_b}{\delta z_{PB}} T_B \end{aligned}$$

$$+ \varrho c \frac{\Delta V}{\Delta t} T_P^o + S_u \quad (3.17)$$

This entire equation will be condensed into Equation (3.18):

$$a_P T_P = a_W T_W + a_E T_E + a_N T_N + a_S T_S + a_T T_T + a_B T_B + a_P^o T_P^o + S_u \quad (3.18)$$

where:

$$a_W = \frac{\kappa_w A_w}{\delta x_{PW}} \quad (3.19a)$$

$$a_E = \frac{\kappa_e A_e}{\delta x_{EP}} \quad (3.19b)$$

$$a_N = \frac{\kappa_n A_n}{\delta y_{NP}} \quad (3.19c)$$

$$a_S = \frac{\kappa_s A_s}{\delta y_{PS}} \quad (3.19d)$$

$$a_T = \frac{\kappa_t A_t}{\delta z_{TP}} \quad (3.19e)$$

$$a_B = \frac{\kappa_b A_b}{\delta z_{PB}} \quad (3.19f)$$

$$a_P^o = \varrho c \frac{\Delta V}{\Delta t} \quad (3.19g)$$

$$a_P = a_W + a_E + a_N + a_S + a_T + a_B + a_P^o - S_P \quad (3.19h)$$

Finally, the algebraic system to solve the transient three-dimensional temperature field of the CubeSat is:

$$a_P T_P = \sum_{nb} a_{nb} T_{nb} + a_P^o T_P^o + S_u \quad (3.20)$$

where the coefficients a are the diffusive flux terms, P refers to the node of a finite volume surrounded by its neighboring nodes (nb), the superscript "o" refers to a previous (old) time level, and S_u is the coefficient of the linearized source term. For further details about the FVM, please refer to Versteeg and Malalasekera (2007). The iterative method to solve Equation (3.20) of this work is the TDMA (Tridiagonal Matrix Algorithm) (VERSTEEG; MALALASEKERA, 2007).

3.2.2.3 Boundary conditions in the FVM

The variables S_u and S_P introduces the boundary conditions, heat sinks, and sources, changing accordingly with the problem. For the heat transfer problem in CubeSat, the two boundary conditions are:

- Dirichlet (Prescribed temperature);

- Neumann (Flux prescribed);

In this work, both conditions will be used. The method bases on the frontier volume's balance of energy, a versatile technique for different scenarios that does not increase the number of volumes (MALISKA, 2004). Figure 34 illustrates the frontier volume and the terms applied for boundary conditions development.

Figure 34 – Frontier volume

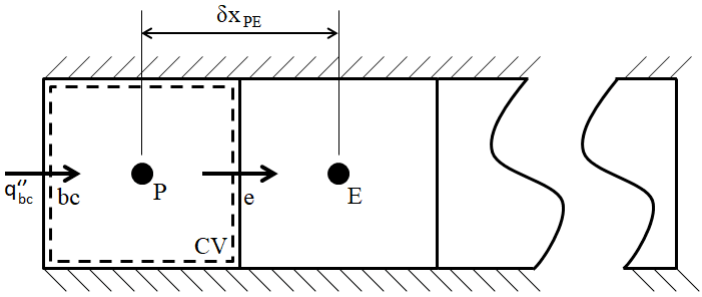

Source: Adapted from Maliska (2004)

Assuming fully implicit scheme, the balance in the frontier volume is:

$$\varrho c \frac{\Delta V}{\Delta t}\left(T_P - T_P^o\right) = q''_{bc} A_{bc} - \frac{\kappa_e A_e}{\delta x_{PE}}\left(T_P - T_E\right) \tag{3.21}$$

The heat flux (q''_{bc}) is the key parameter to introduce different boundary conditions, to be discussed below.

One possibility of boundary condition is the incoming heat flux by radiation ($q''_{r_{in}}$) on the volume's surface, as well as outgoing heat flux by radiation ($q''_{r_{out}}$), according to Figure 35.

Figure 35 – Volume at the border with heat exchange by radiation

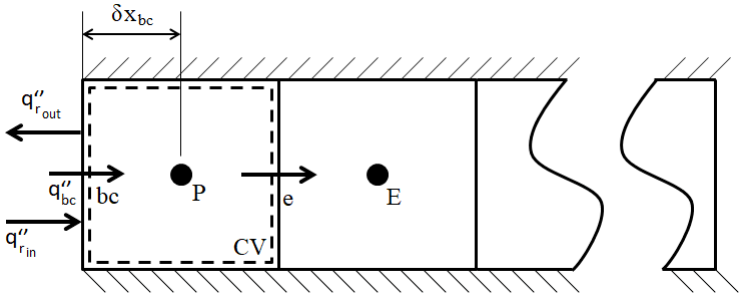

Source: The author

Therefore:

$$q''_{bc} = q''_{r_{in}} - q''_{r_{out}} = \kappa \frac{T_{bc} - T_P}{\delta x_{bc}} \tag{3.22}$$

Recognizing $q''_{r_{out}} = \varepsilon\sigma T_{bc}^4$, the previous equation becomes:

$$q''_{bc} = q''_{r_{in}} - \varepsilon\sigma T_{bc}^4 = \kappa\frac{T_{bc} - T_P}{\delta x_{bc}} \tag{3.23}$$

The idea here is to isolate the variable T_{bc}, however now it is raised to the fourth power and to the first power. To solve it, a linearization through the Taylor series around T_{bc}^* is performed in $q''_{r_{out}}$, where only the first term is kept, as follows:

$$q''_{r_{out}} \approx q''_{r_{out}}\left(T_{bc}^*\right) + \frac{dq''_{r_{out}}\left(T_{bc}^*\right)}{dT}\left(T_{bc} - T_{bc}^*\right) \tag{3.24}$$

$$q''_{r_{out}} \approx \varepsilon\sigma T_{bc}^{*^4} + 4\varepsilon\sigma T_{bc}^{*^3}\left(T_{bc} - T_{bc}^*\right) = -3\varepsilon\sigma T_{bc}^{*^4} + 4\varepsilon\sigma T_{bc}^{*^3} T_{bc} \tag{3.25}$$

Replacing it in Equation 3.22:

$$q''_{bc} = q''_{r_{in}} + 3\varepsilon\sigma T_{bc}^{*^4} - 4\varepsilon\sigma T_{bc}^{*^3} T_{bc} = \kappa\frac{T_{bc} - T_P}{\delta x_{bc}} \tag{3.26}$$

Isolating T_{bc}:

$$T_{bc} = \left(q''_{r_{in}} + 3\varepsilon\sigma T_{bc}^{*^4} + \frac{\kappa}{\delta x_{bc}} T_P\right)\left(\frac{\delta x_{bc}}{\kappa + 4\varepsilon\sigma\delta x_{bc} T_{bc}^{*^3}}\right) \tag{3.27}$$

Substituting the equation for T_{bc} into Equation 3.22:

$$q''_{bc} = \left[\left(q''_{r_{in}} + 3\varepsilon\sigma T_{bc}^{*^4}\right)\left(\frac{\kappa}{\kappa + 4\varepsilon\sigma\delta x_{bc} T_{bc}^{*^3}}\right) - \frac{4\kappa\varepsilon\sigma T_{bc}^{*^3}}{\kappa + 4\varepsilon\sigma\delta x_{bc} T_{bc}^{*^3}} T_P\right] \tag{3.28}$$

Replacing it into Equation 3.21:

$$\varrho c\frac{\Delta V}{\Delta t}\left(T_P - T_P^o\right) = \left[\left(q''_{r_{in}} + 3\varepsilon\sigma T_{bc}^{*^4}\right)\left(\frac{\kappa}{\kappa + 4\varepsilon\sigma\delta x_{bc} T_{bc}^{*^3}}\right) - \frac{4\kappa\varepsilon\sigma T_{bc}^{*^3}}{\kappa + 4\varepsilon\sigma\delta x_{bc} T_{bc}^{*^3}} T_P\right] A_{bc} - \frac{\kappa_e A_e}{\delta x_{PE}}\left(T_P - T_E\right) \tag{3.29}$$

Rearranging the terms:

$$\left(\frac{\kappa_e A_e}{\delta x_{PE}} + \varrho c\frac{\Delta V}{\Delta t} + \frac{4\kappa\varepsilon\sigma A_{bc} T_{bc}^{*^3}}{\kappa + 4\varepsilon\sigma\delta x_{bc} T_{bc}^{*^3}}\right) T_P = \frac{\kappa_e A_e}{\delta x_{PE}} T_E + \varrho c\frac{\Delta V}{\Delta t} T_P^0 + + \left(q''_{r_{in}} + 3\varepsilon\sigma T_{bc}^{*^4}\right)\left(\frac{\kappa A_{bc}}{\kappa + 4\varepsilon\sigma\delta x_{bc} T_{bc}^{*^3}}\right) \tag{3.30}$$

In the converged solution, $T^*_{bc} = T_{bc}$.

The second possibility of boundary condition comes from the multi-block grid, where the heat between grids is exchanged through conduction across their common faces, according to Figure 36. In this figure, node 2 is from the adjacent mesh.

Figure 36 – Volume at the border with heat exchange by conduction in the multi-block grid

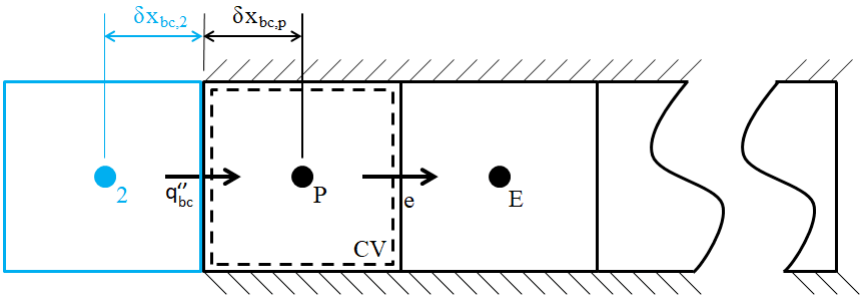

Source: The author

Therefore, the heat flux is:

$$q''_{bc} = \kappa_2 \frac{T_2 - T_{bc}}{\delta x_{bc,2}} = \kappa_p \frac{T_{bc} - T_P}{\delta x_{bc,p}} \tag{3.31}$$

Isolating the temperature at the boundary:

$$T_{bc} = \frac{\kappa_p \delta x_{bc,2} T_P + \kappa_2 \delta x_{bc,p} T_2}{\kappa_p \delta x_{bc,2} + \kappa_2 \delta x_{bc,p}} \tag{3.32}$$

Substituting T_{bc} in Equation (3.31):

$$q''_{bc} = \frac{\kappa_p \kappa_2}{\kappa_p \delta x_{bc,2} + \kappa_2 \delta x_{bc,p}} T_2 - \frac{\kappa_p \kappa_2}{\kappa_p \delta x_{bc,2} + \kappa_2 \delta x_{bc,p}} T_P \tag{3.33}$$

This heat flux q''_{bc} is then replaced in Equation (3.21):

$$\varrho c \frac{\Delta V}{\Delta t} (T_P - T^o_P) = \left[\frac{\kappa_p \kappa_2}{\kappa_p \delta x_{bc,2} + \kappa_2 \delta x_{bc,p}} T_2 - \frac{\kappa_p \kappa_2}{\kappa_p \delta x_{bc,2} + \kappa_2 \delta x_{bc,p}} T_P \right] A_{bc} - \frac{\kappa_e A_e}{\delta x_{PE}} (T_P - T_E) \tag{3.34}$$

Rearranging the terms:

$$\left(\frac{\kappa_e A_e}{\delta x_{PE}} + \varrho c \frac{\Delta V}{\Delta t} + \frac{\kappa_p \kappa_2 A_{bc}}{\kappa_p \delta x_{bc,2} + \kappa_2 \delta x_{bc,p}} \right) T_P = \frac{\kappa_e A_e}{\delta x_{PE}} T_E + \varrho c \frac{\Delta V}{\Delta t} T^o_P$$

$$+\frac{\kappa_p \kappa_2 A_{bc}}{\kappa_p \delta x_{bc,2} + \kappa_2 \delta x_{bc,p}} T_2 \quad (3.35)$$

For both conditions described above, the coefficients S_u and S_P are summarized in Table 4:

Table 4 – Coefficients of source term for each boundary condition

Boundary condition	S_u	S_P
Heat exchange by radiation	$\left(q''_{r_{in}} + 3\varepsilon\sigma T_{bc}^{*4}\right)\left(\frac{\kappa A_{bc}}{\kappa + 4\varepsilon\sigma\delta x_{bc} T_{bc}^{*3}}\right)$	$-\frac{4\kappa\varepsilon\sigma A_{bc} T_{bc}^{*3}}{\kappa + 4\varepsilon\sigma\delta x_{bc} T_{bc}^{*3}}$
Conduction between multi-block grids	$\frac{\kappa_p \kappa_2 A_{bc}}{\kappa_p \delta x_{bc,2} + \kappa_2 \delta x_{bc,p}} T_2$	$\frac{\kappa_p \kappa_2 A_{bc}}{\kappa_p \delta x_{bc,2} + \kappa_2 \delta x_{bc,p}}$

Source: The author

3.2.2.4 Internal heat transfer by radiation

In thermal radiation analysis, the heat exchange between surfaces must be considered simultaneously, no matter how far they are, leading to a complete enclosure analysis than an infinitesimal control volume. In this work, radiation's internal heat transfer will use the Gebhart Method (GEBHART, 1961; HOWELL; MENGUC; SIEGEL, 2010). The incident heat flux comes from all its surrounding neighbors for a cavity, even those not directly seen because of multi-reflections. To calculate the internal heat exchange, the following assumptions will be necessary:

- Each discretized surface is isothermal;
- Gray and diffuse surfaces;
- The energy leaving or reaching a surface is uniformly distributed, so the view factor between two surfaces is constant.

The heat transfer by radiation from surface i to j will be:

$$q_i = A_i \varepsilon_i \sum_{j=1}^{M} G_{i-j} \sigma \left(T_i^4 - T_j^4\right) \quad (3.36)$$

The term G_{i-j} is the absorption factor and represents the fraction of energy emitted by surface A_i that hits A_j and there it is absorbed, including direct (emission) and indirect (reflection) ways from all the surfaces M. The absorption factor has the reciprocity relation and the summation rule, given by Equation (3.37) and Equation (3.38), respectively.

$$\varepsilon_i A_i G_{i-j} = \varepsilon_j A_j G_{j-i} \quad (3.37)$$

$$\sum_{j=1}^{M} G_{i-j} = 1 \tag{3.38}$$

The absorption factor is calculated as:

$$hG = f \tag{3.39a}$$

$$G = \begin{bmatrix} G_{1-1} & G_{1-2} & \cdots & G_{1-M} \\ G_{2-1} & G_{2-2} & \cdots & G_{2-M} \\ \vdots & \vdots & \ddots & \vdots \\ G_{M-1} & G_{M-2} & \cdots & G_{M-M} \end{bmatrix} \tag{3.39b}$$

$$h = \begin{bmatrix} 1-\rho_1\widehat{F}_{1-1} & -\rho_2\widehat{F}_{1-2} & \cdots & -\rho_M\widehat{F}_{1-M} \\ -\rho_1\widehat{F}_{2-1} & 1-\rho_1\widehat{F}_{1-1} & \cdots & -\rho_M\widehat{F}_{2-M} \\ \vdots & \vdots & \ddots & \vdots \\ -\rho_1\widehat{F}_{M-1} & -\rho_2\widehat{F}_{M-2} & \cdots & 1-\rho_M\widehat{F}_{M-M} \end{bmatrix} \tag{3.39c}$$

$$f = \begin{bmatrix} \widehat{F}_{1-1}\varepsilon_1 & \widehat{F}_{1-2}\varepsilon_2 & \cdots & \widehat{F}_{1-M}\varepsilon_M \\ \widehat{F}_{2-1}\varepsilon_1 & \widehat{F}_{2-2}\varepsilon_2 & \cdots & \widehat{F}_{2-M}\varepsilon_M \\ \vdots & \vdots & \ddots & \vdots \\ \widehat{F}_{M-1}\varepsilon_1 & \widehat{F}_{M-2}\varepsilon_2 & \cdots & \widehat{F}_{M-M}\varepsilon_M \end{bmatrix} \tag{3.39d}$$

The term ρ is the reflectivity [-] and $\widehat{F}$ [-] is the normalized view factor.

By assuming that the radiative properties are independent of temperature, the Gebhart factors' matrix is solved before the FVM, and the values are recovered from a file in the memory. The computation of view factors with potential obstructing requires considerable CPU time, and for this reason, this process divides into two parts: determination of obstructions and then the view factor itself. These two parameters will be explained in the next section.

3.2.2.5 Obstruction

Internally, depending on the components' geometry and position, there may have surfaces that can not see directly each other, but they still exchange by radiation through multiple reflections. For such a case, an algorithm is necessary to verify the obstruction, here based on the work of WALTON (1986). The verification of obstructions is computationally costly, so the tests to confirm the obstruction are arranged to confirm it as earlier as possible. For the pair of surfaces i and j with obstructing views, the value $O(i,j) = -1$ will be attributed, while for the unobstructed pairs it will be $O(i,j) = 1$.

The first test, shown in Figure 37, uses the dot product between the normal vector of surface A_i, located at the center of that surface, and the vertices of surface A_j. If the result

is negative for all of them, it means that A_j is completely behind A_i, so they do not see each other, and there is an obstruction ($O\,(i,j) = -1$). They also do not see if the dot product is 0, a condition where the surfaces are coplanar. If the test is partially negative, there is some view between the surfaces, but this work assumes an obstruction. This condition will impact the estimation of view factors, as will be seen in the next section. The surfaces entirely see each other and assume $O(i,j) = 1$ only if the dot product is entirely positive.

Figure 37 – Test of the dot product to estimate the obstruction. Left: $O(i,j) = -1$; Middle: $O(i,j) = -1$; Right: $O(i,j) = 1$

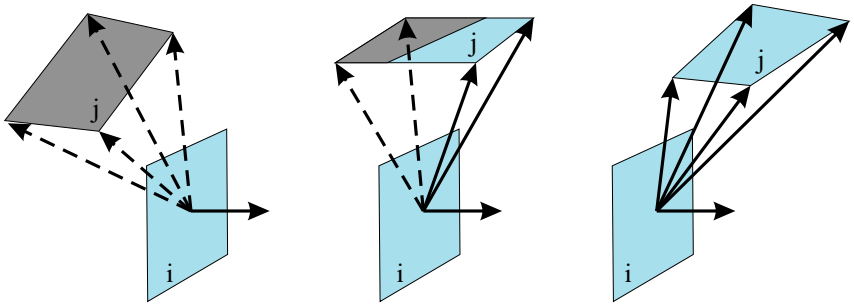

Source: The author

After this test, only the pairs with $O\,(i,j) = 1$ will continue to the next. Although surfaces i and j are in front of each other, there may have a third surface k blocking their views. This procedure is illustrated in Figure 38. A radius circumscribing the surface k (R_k) and the centroid of that surface (x_k, y_k, z_k) are determined. An unitary vector connecting the centroid of i and j is determined ($\mathbf{u}_{i,j}$), as well as a vector connecting the centroid of i and k ($\vec{V}_{i,k}$). The magnitude of the dot product $|\vec{V}_{i,k} \cdot \mathbf{u}_{i,j}|$ gives the projection of $\vec{V}_{i,k}$ into the direction of $\mathbf{u}_{i,j}$. The radius circumscribing surface i (R_i) and j (R_j) are also determined. Therefore, a representative radius R_{ijk}, at the height of k, from the cone englobing both surfaces i and j is:

$$R_{ijk} = R_i + \frac{|\vec{V}_{i,k} \cdot \mathbf{u}_{i,j}|}{|\vec{V}_j - \vec{V}_i|}\,(R_j - R_i) \tag{3.40}$$

The distance from the center of k up to the line connecting the center of i and j will be obtained by the magnitude of the cross product $D = |\vec{V}_{i,k} \times \mathbf{u}_{i,j}|$. Therefore, the surface k will not obstruct the view of i and j when:

$$O\,(i,j) = \begin{cases} 1, & D^2 > (R_{ijk} + R_k)^2 \\ \text{next test}, & \text{otherwise} \end{cases} \tag{3.41}$$

If the previous condition is not satisfied, there are still more tests to check whether k really blocks i and j, done through the dot product. The surfaces i and j are not blocked

Figure 38 – Test of the cone to estimate the obstruction

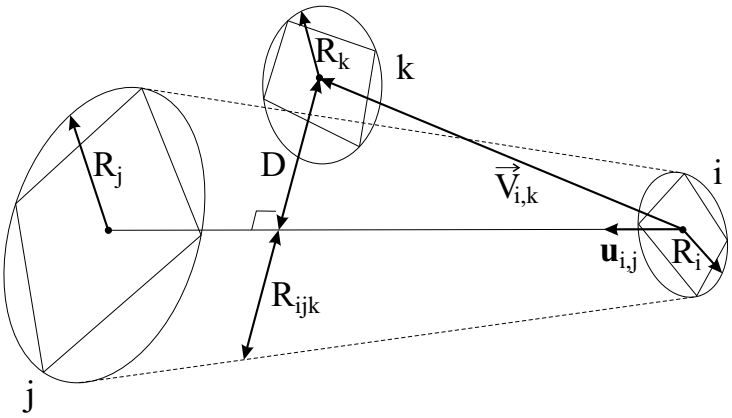

Source: Adapted from WALTON (1986)

($O(i,j) = 1$) according to the cases illustrated in Figure 39. If none of the conditions from Figure 39 are satisfied, they can not see each other.

Figure 39 – Final test of obstruction

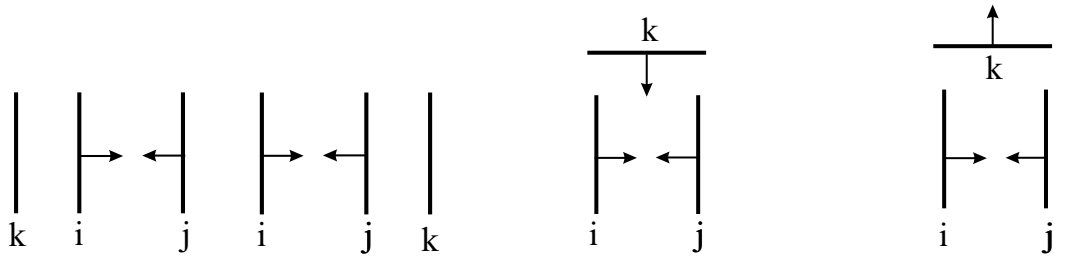

(a) k is behind i. (b) k is behind j. (c) i and j are in front of k. (d) i and j are behind of k.

Source: The author

Further actions may minimize errors in the obstruction determination, for example, accounting for partial shadowing. Also, the circumscribing surface's radius may overestimate the surfaces' actual size when their sides are not equal, as for rectangles. In this work, the circumscribing surfaces are given by the average length of the surface's sides, and no action will be performed for the accounting of partial shadows. The impact of these decisions will be discussed in the chapter of results.

3.2.2.6 View factor

The view factor between two infinitesimal surfaces dA_i e dA_j is the fraction of the radiation leaving surface i that is intercepted by surface j (BERGMAN et al., 2011). It is calculated by Equation (3.42) and illustrated in Figure 40.

- $dF_{dA_i - dA_j}$: diffuse energy leaving dA_i directly toward and intercepted by dA_j over the total diffuse energy leaving dA_i

Figure 40 – Radiative exchange between two surfaces

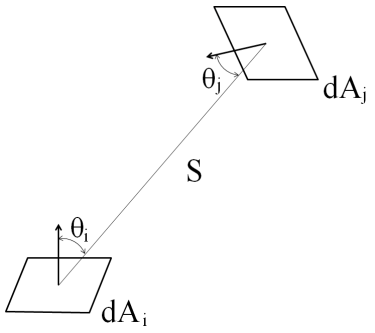

Source: Adapted from Bergman et al. (2011)

$$F_{A_i - A_j} = \frac{1}{A_i} \int_{A_i} \int_{A_j} \frac{\cos(\theta_i)\cos(\theta_j)}{\pi S^2} dA_j dA_i \tag{3.42}$$

After determining unobstructed surfaces, the view factor between them can be computed by several different techniques available in the literature. In this work, only parallel and perpendicular surfaces exist and they will be calculated exclusively for those surfaces that see each other, given by $O(i,j) = 1$. The remaining surfaces will have $F_{i,j} = 0$. For both conditions of orientations shown in Figure 41, the equation to compute the view factor from surface 1 to 2 is (EHLERT; SMITH, 1993):

$$F_{1-2} = \frac{1}{(x_2 - x_1)(y_2 - y_1)} \times \sum_{s=1}^{2} \sum_{r=1}^{2} \sum_{q=1}^{2} \sum_{p=1}^{2} (-1)^{(p+q+r+s)} U(x_p, y_q, \eta_r, \xi_s) \tag{3.43}$$

For parallel surfaces the function U is given by Equation (3.44), while for perpendicular surfaces it is the Equation (3.45). Figure 41a and Figure 41b illustrate the terms of these equations.

$$\begin{aligned} U = \frac{1}{2\pi} \Bigg(& (y-\eta) \left[(x-\xi)^2 + z^2 \right]^{1/2} \tan^{-1} \left(\frac{y-\eta}{\left[(x-\xi)^2 + z^2 \right]^{1/2}} \right) \\ & + (x-\xi) \left[(y-\eta)^2 + z^2 \right]^{1/2} \tan^{-1} \left[\frac{x-\xi}{\left[(y-\eta)^2 + z^2 \right]^{1/2}} \right] \\ & - \frac{z^2}{2} \ln \left[(x-\xi)^2 + (y-\eta)^2 + z^2 \right] \Bigg) \end{aligned} \tag{3.44}$$

$$U = \frac{1}{2\pi} \Bigg((y-\eta) \left(x^2 + \xi^2 \right)^{1/2} \tan^{-1}(B) - \frac{1}{4} \left[\left(x^2 + \xi^2 \right) \ln \left(1 + B^2 \right) \right.$$

$$- (y-\eta)^2 \ln\left(1+\frac{1}{B^2}\right)\Bigg] \quad (3.45)$$

where $B = (y-\eta) / (x^2+\xi^2)^{0.5}$.

Figure 41 – Diagrams to estimate the view factors

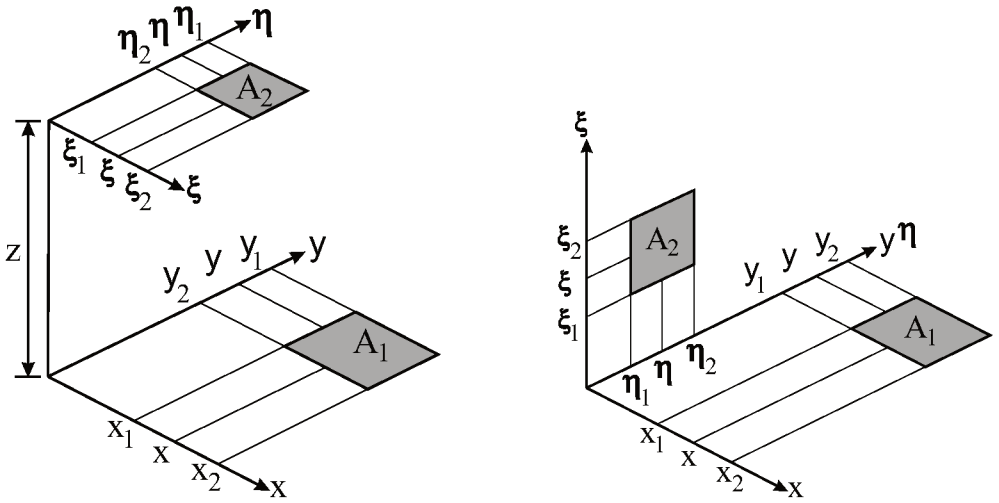

(a) Parallel surfaces. (b) Perpendicular surfaces.

Source: Ehlert and Smith (1993)

Independently of the surface's shape and orientation, the summation rule of view factors must be satisfied in an enclosure (BERGMAN et al., 2011). This condition would not be satisfied here because the obstruction computation assumes entirely blocked surfaces even when just a small fraction is under the shadow, as exemplified by Figure 42. The red surfaces are those considered under the shadow by the previous obstruction test, while the grays are those partially shadowed that go to the list of shadowed surfaces ($O(i,j) = -1$). This problem is minimized with refined mesh; however, it will still exist.

Figure 42 – The partial obstructions: coarse mesh (left); refined mesh (right)

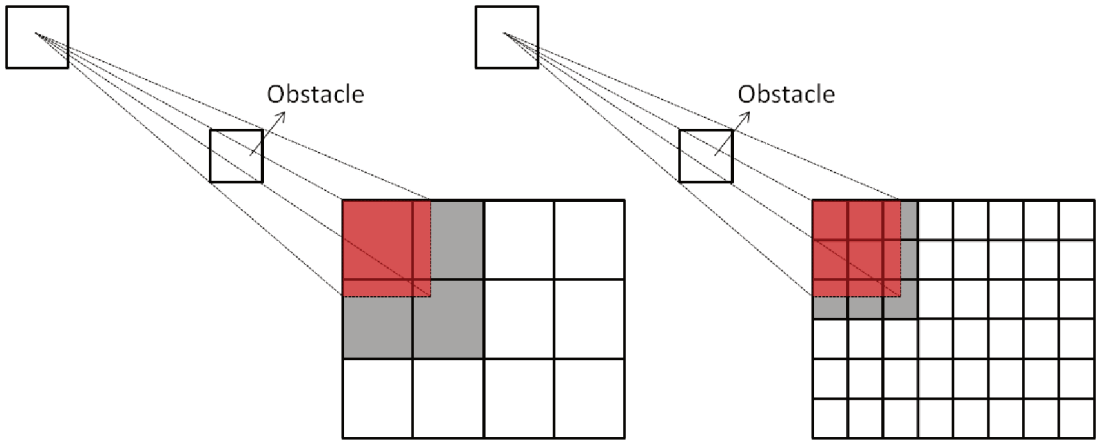

Source: The author

For this reason, a normalization is realized by dividing the analytical view factor obtained with Equation (3.43) by the sum of view factors obtained with surface i, as follows:

$$\widehat{F}_{i-j} = \frac{F_{i-j}}{\sum_{j=1}^{M} F_{i-j}} \tag{3.46}$$

Thus, $\widehat{F}_{i-j}$ satisfies the summation rule:

$$\sum_{j=1}^{M} \widehat{F}_{i-j} = 1 \tag{3.47}$$

3.3 CONSIDERATIONS

This chapter presented the formulation of two techniques able to solve the temperature field of CubeSats, namely the Lumped Parameter Method and Finite Volume Method. The first one has several idealizations and simplifies the conductive and internal radiative heat transfer in a single parameter Q_Z. On the other hand, the model based on the FVM computes the internal heat transfer by radiation through the Gebhart method and uses a procedure to compute the obstructing views between the surfaces, which requires significant computational resources.

Results from thermal simulations using these models for a CubeSat geometry will be presented in the next chapter, and a comparison of the outcomes from both models will be discussed.

4 RESULTS

This chapter starts by delineating the study cases. Later, the simulation's parameters are defined, including the geometry of a CubeSat 1U, its material properties, incoming radiation, convergence criteria, and the mesh independence test. Finally, the irradiance and thermal model will be used to simulate a CubeSat integrated to a heat pipe and a thermoelectric generator.

To assess the impact of inner boundary conditions, the following cases will be tested:

- E-0: All surfaces in the internal side of the CubeSat has emissivity equal to 0.0;
- E-1/2: All surfaces in the internal side of the CubeSat has emissivity equal to 0.5;
- E-1: All surfaces in the internal side of the CubeSat has emissivity equal to 1.0;

The extreme condition without internal radiation and maximum internal radiation are designated by E-0 and E-1, respectively. An intermediate configuration between these two theoretical limits will be simulated in the case E-1/2, where the internal surfaces have emissivity equal to 0.5.

4.1 THE DOMAIN OF FVM SIMULATION

The domain is discretized into a structured multi-block grid composed of a set of small hexahedral volumes, where the temperature and the heat fluxes are evaluated at the centroid and surfaces of the volume, respectively. The geometry represents a CubeSat 1U, according to Figure 43. It has the main external dimension of 10.0x10.0x10.0 cm, with six solar panels covering the outer side of the CubeSat (10.0x10.0x0.2 cm, in red), an internal structure with a cross-section of 0.5x0.5 cm in each bar (in green), a battery (6.0x6.0x0.9 cm, in magenta), four PCBs representing generic payloads (9.0x9.0x0.2 cm each, in light-blue), and bolts to connect the PCBs and the structure (with a cross-section of 0.5x0.5 cm each, in blue). In this work, both bolts and structure are the same material.

Each side of the CubeSat receives a number for its identification, as in the irradiance model. Notice that the solar panels cover the CubeSat's entire external surface, and the bolts provide a conductive thermal path between the sides 5 and 6 of the CubeSat. The battery is attached to the top of PCB_2. Figure 44 shows a schematic view of the internal parts, without the structure and bolts. There is one major cavity formed by the solar panels, while the PCBs and battery act as obstructions inside the cavity, all of them absorbing and emitting radiation.

Figure 43 – The mesh of FVM simulation

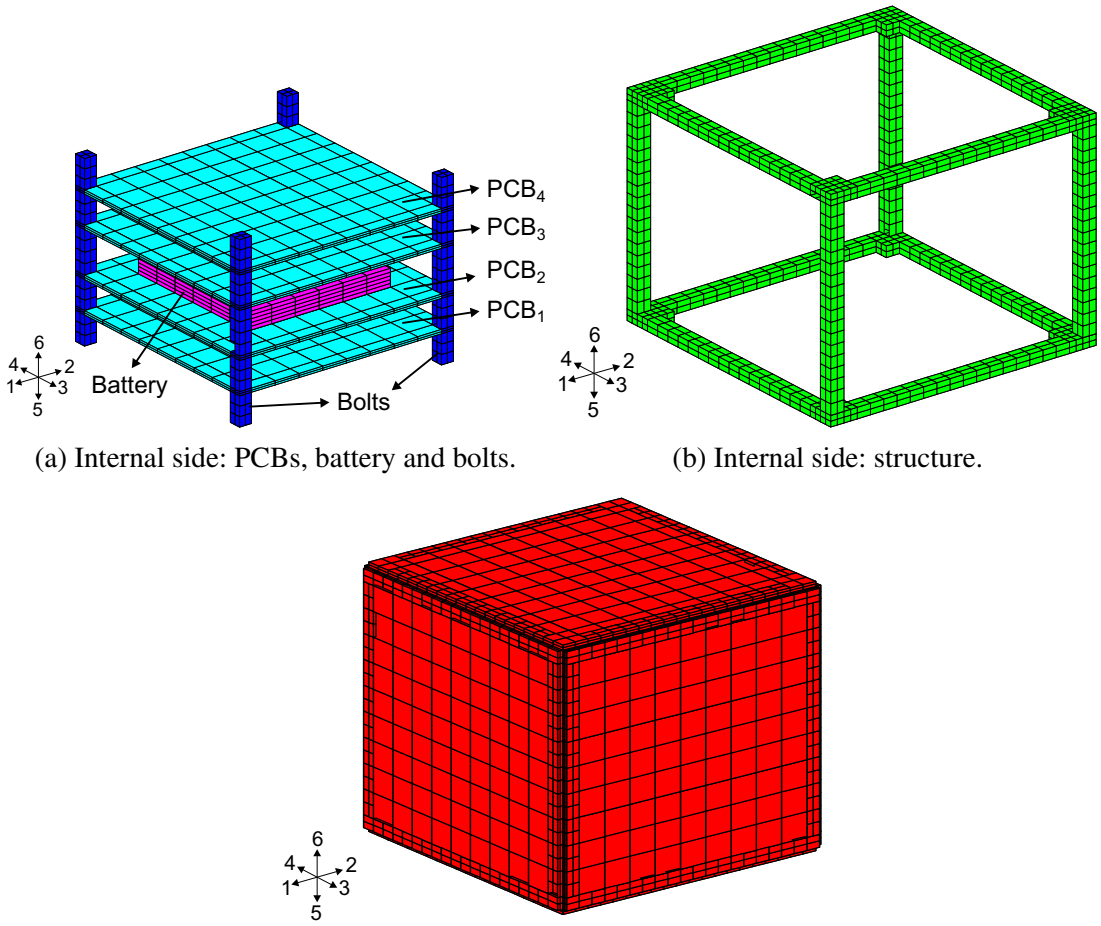

(a) Internal side: PCBs, battery and bolts.

(b) Internal side: structure.

(c) External side: solar panels.

Source: The author

Figure 44 – Diagram for the internal view

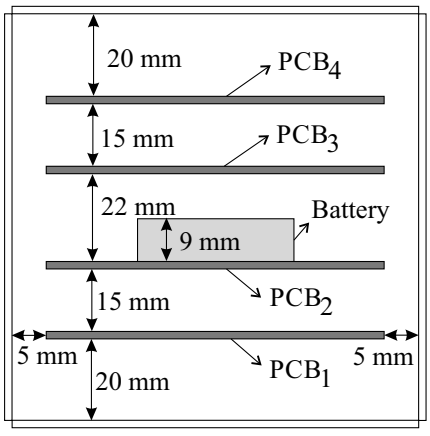

Source: The author

4.2 MATERIAL PROPERTIES

The literature regarding thermal simulations of CubeSats and satellites presents a wide range for the thermal and surface properties of the main parts, as shown in Table 5. While the

emissivity is for short-wave radiation, the absorptivity is for solar-wave radiation.

Table 5 – Thermal and surface properties of CubeSat's main parts

	Thermal property			**Surface property**	
Part	ϱ [kg/m^3]	c [J/kg.K]	κ [W/m.K]	ε [-]	α [-]
Solar panel	1840[1] 2810[1]	800[1] 862[2] 1150[7] 1600[4]	1.03[1]	0.60[5] 0.85[4]	0.68[5] 0.85[8] 0.91[4]
Structure	2810[3]	936[4,5] 960[1,6]	130[1] 150[2,3]	0.08[4,7] 0.79-0.88[8]	0.37[4,5] 0.25-0.91[6]
PCB	1840[7] 2400[1]	800[1] 1150[7]	0.25[9] 1.03[1]	0.22[7]	0.85[8]
Battery	2122[10] 2180[7] 2440[11]	933[10] 960[7] 1200[8] 1210[11] 1250[1]	12.5[11] 21[10] 36[7]	0.7[7]	-

Source: The author

The average values from previous table, and shown in Table 6, are used to compose the thermal properties of the simulation. Except for the external emissivity and absorptivity of solar panels, which are the only parts exposed to outer space, the surface properties of remaining internal components are ruled by the cases of study.

Table 6 – Thermal properties for the standard case

	Thermal property			**Surface property (external side only)**	
Part	ϱ [kg/m^3]	c [J/kg.K]	κ [W/m.K]	ε [-]	α [-]
Solar panel	2325	1103	1.03	0.72	0.77
Structure	2810	948	140	Defined according to the case study	
PCB	2120	975	0.64	Defined according to the case study	
Battery	2247	1110	23	Defined according to the case study	

Source: The author

1 (FILHO et al., 2020)
2 (ESCOBAR; DIAZ; ZAGAL, 2016)
3 (KARAM, 1998)
4 (REYES et al., 2020)
5 (BULUT; SOZBIR, 2015)
6 (MESEGUER; PÉREZ-GRANDE; SANZ-ANDRÉS, 2012)
7 (BONNICI et al., 2019)
8 (KOVÁCS; JÓZSA, 2018)
9 (CORPINO et al., 2015)
10 (WANG; JI; ZHU, 2021)
11 (YANG et al., 2020)

4.3 ATTITUDE AND ORBIT

The orbit scenario is coherent with TLE1 showed in Table 2. The CubeSat has an attitude called nadir, where the normal vector of surface 2 continuously faces the Earth's surface, as already shown in Figure 25.

4.4 CONVERGENCE CRITERIA AND MESH INDEPENDENCE TEST

For each timestep, set to 10 s, the convergence criteria is a normalized global residual smaller than 10^{-5} for the volumes of a mesh, 10^{-6} for the volumes in contact with a neighbor mesh, and a difference smaller than 10^{-2} in the balance of each surface exposed to internal or external heat transfer by radiation. The external boundary condition is cyclic, and the interest is in results independent of the initial condition. For this reason, an extra condition for the convergence of the result is a difference between the temperature field on the last instant of the orbit and that obtained in the first, within a margin of ± 1 K.

The simulations were implemented in MATLAB. They were run in a Ubuntu environment, in a computer with an Intel Core Xeon E5-2665 Processor (2.40 GHz), with 8 cores of 2 threads and 64 GB of RAM.

The overall features obtained with three meshes' refinements are indicated in Table 7. These results highlight the strong relation of computational cost with the grid's size. While the number of volumes of Mesh 1 is around six times smaller than Mesh 2, the total time to compute the obstruction is 27 times faster for Mesh 1 than Mesh 2, and 15 times faster to solve the temperature field. With Mesh 3, the total time to compute the obstruction is 16 times slower than Mesh 2 and five times slower to solve the temperature field than Mesh 2.

Table 7 – Mesh independence study

Parameter	Mesh 1	Mesh 2	Mesh 3
Number of volumes	829	5212	19098
Number of faces with internal heat transfer by radiation	982	2844	7174
Time to compute obstruction [h]	0.2	5.5	90.4
Time to solve the cyclic temperature field [h]	1.1	16.2	89.3

Source: The author

The sum of view factors before the normalization executed by Equation (3.46), for each discretized surface on the inner side of the CubeSat, are illustrated in the histogram of Figure 45. The x-axis shows the view factor sum, and the y-axis is the percentage of total surfaces from the mesh with that corresponding view factor sum. The theory states that the sum of view factor should be one for a cavity, but the determination of obstructions assumed in this work put

those partially blocked surfaces in the list of totally blocked surfaces. Because the view factor is calculated only between those unblocked surfaces, which did not necessarily form a complete cavity here, there may be insufficient pairs of surfaces to result in a sum of view factors equal to one. It explains the sum of view factor below 1 for some surfaces. Beyond that, the averaging procedure for the circumscribing surfaces may misinterpret an obstruction and overestimate the view factor in a given direction. It results in a sum of view factors above 1. These errors originated in the partial obstruction estimation are more evident with the coarsest Mesh 1 and reduce with the most refined Mesh 3, while the overestimation of the view factor sum is more pronounced with Mesh 3.

Figure 45 – The sum of view factor for each face of the internal side

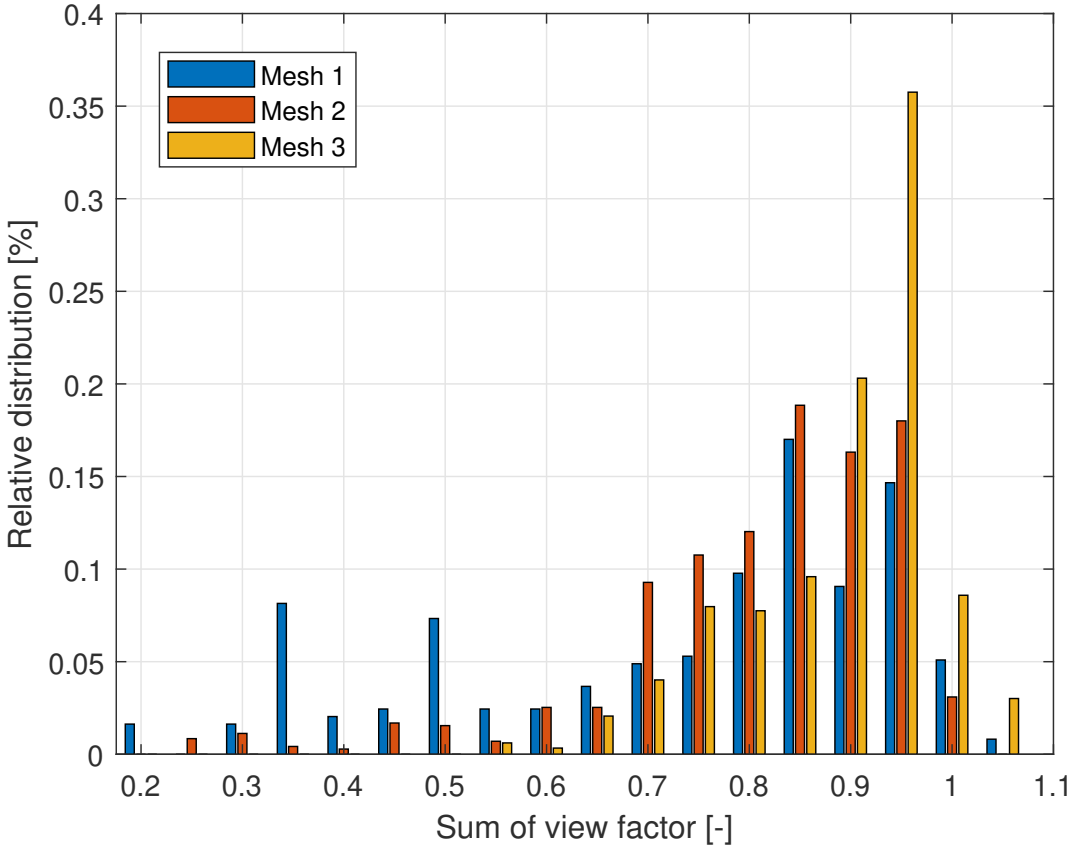

Source: The author

In terms of temperature of each main CubeSat's part, the maximum deviation from Mesh 3 to Mesh 2 was 0.8 K, while for Mesh 1 and Mesh 2 it was 4.3 K. This difference is obtained by comparing the central node of each main part of the CubeSat (solar panels, PCBs, and battery), so the average values of every parts are even below it. For these reasons, Mesh 2 will be used in the following results.

4.5 TEMPERATURE FIELDS

This section will bring the results and discussions about the three cases of internal radiation simulated with FVM: E-0 (internal emissivity is zero); E-1/2 (internal emissivity is 0.5); E-1 (internal emissivity is 1). A comparison between the outcomes of FVM and LPM will also be detailed.

4.5.1 Intermediate internal radiation (E-1/2)

The first result in Figure 46 illustrates the importance of simulating three-dimensional domains. These temperature fields are for t=1720 s, the maximum temperature gradient condition in the satellite, as will be seen later. Notice that the temperature range for each part is adjusted for better visualization. In this case, solar panel 4 receives more radiation than any other side (see Figure 25).

Figure 46 – Temperature field at t=1720 s, for case E-1/2

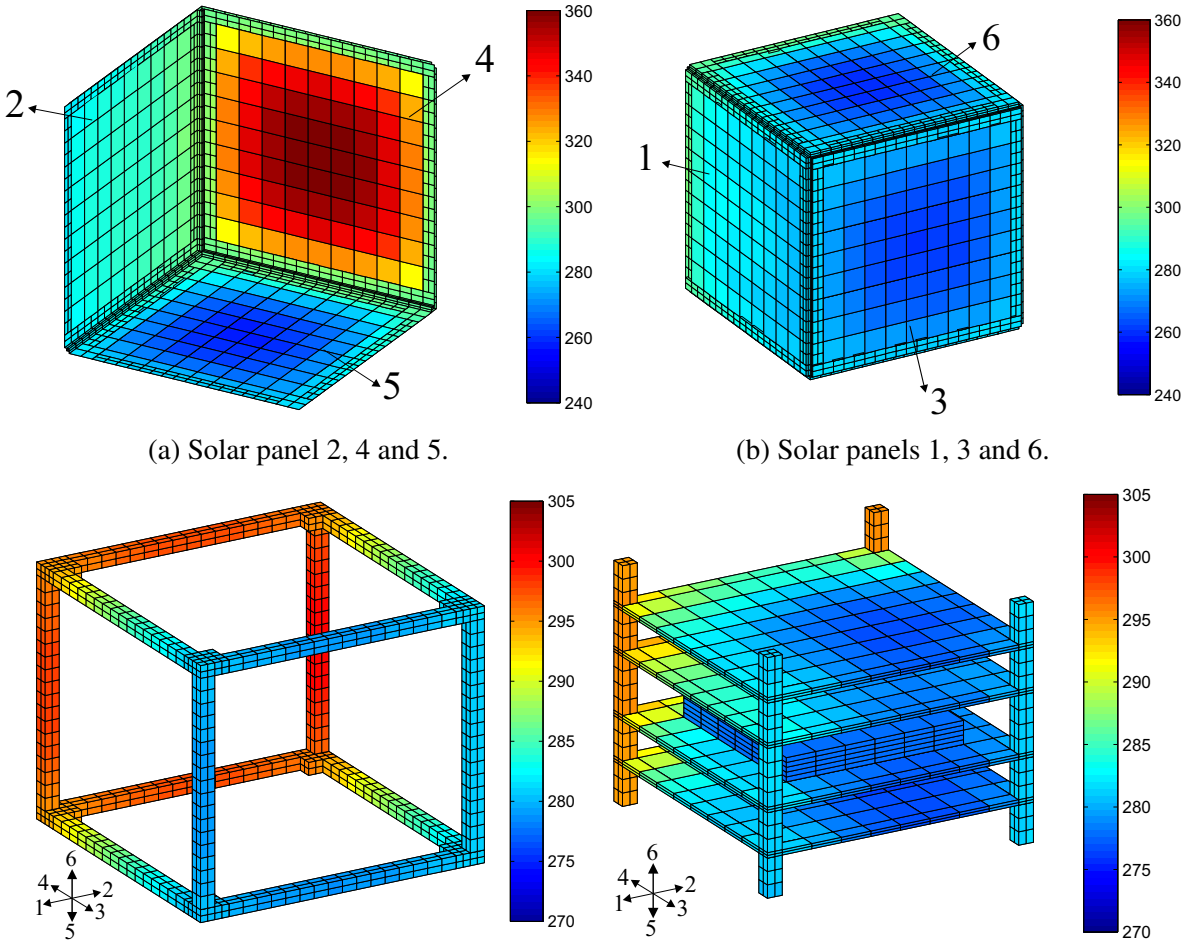

(a) Solar panel 2, 4 and 5.

(b) Solar panels 1, 3 and 6.

(c) Structure.

(d) Internal parts.

Source: The author

Due to the solar panel's low thermal conduction, there is a significant temperature gradient on it, resulting in a peak of temperature in the center and minimum values at the border,

considering only side 4. This distribution is explained by the fact that the internal structure, made of aluminum, is in contact with solar panel 4 only near its borders. For all of these fields, it is evident that a single point of temperature cannot represent the entire CubeSat's temperature field, neither of a single main part.

Figure 47 is valid for t=3880 s, the instant with the minimum temperature gradient among the main parts of the CubeSat and lowest temperature levels, obtained at the last instant before the CubeSat leaves the eclipse. In this case, the solar flux and albedo are absent, resting the Earth's emission as the only heat source for the satellite. Side 2 is normal to the Earth's surface, and side 1 is opposite to side 2, the reason for maximum and minimum temperature in these solar panels, respectively. The remaining sides are perpendicular to the Earth's surface and have a lower view factor to it when compared to side 2, which results in less heat flux from Earth in these surfaces and intermediate temperature levels on them.

Figure 47 – Temperature field at t=3880 s, for case E-1/2

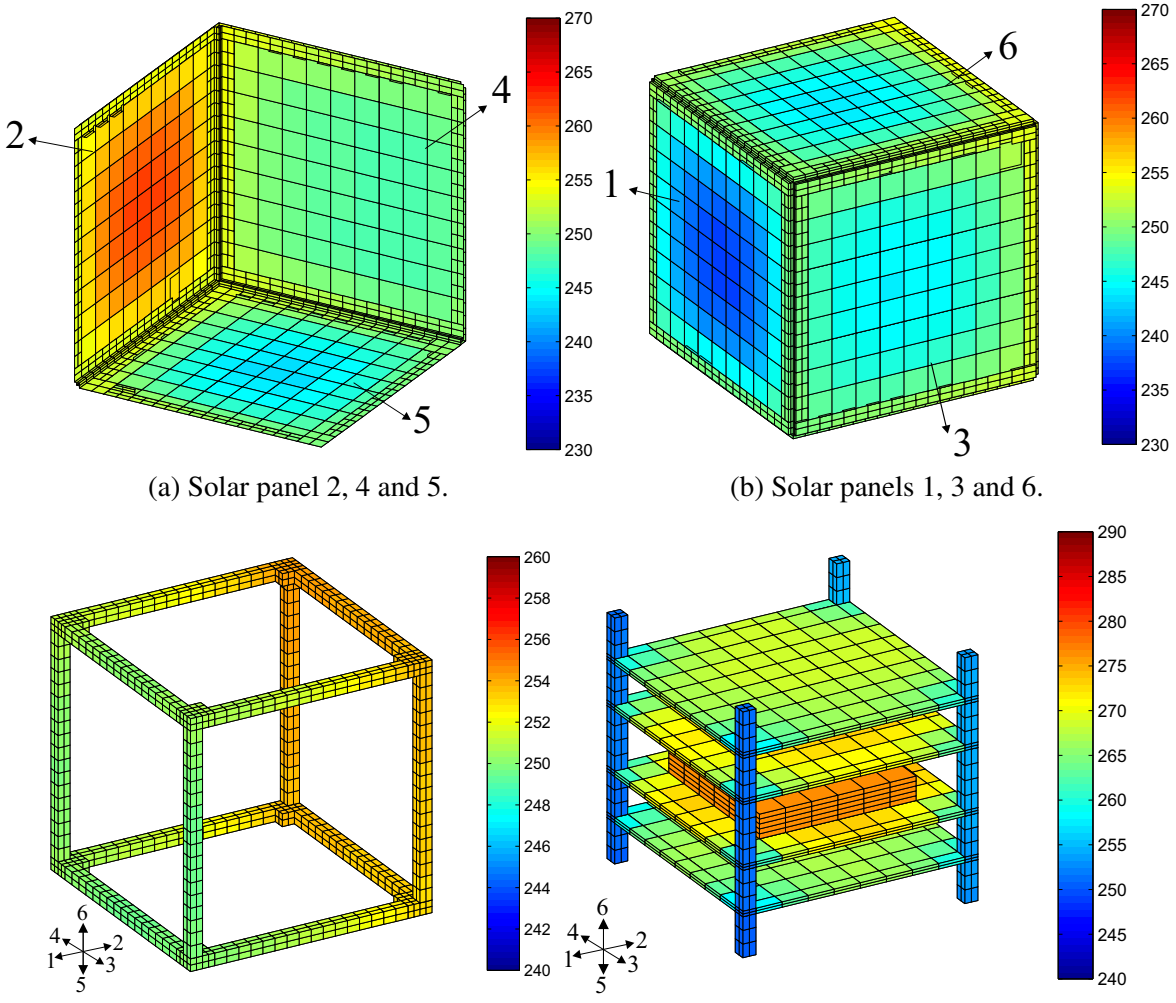

(a) Solar panel 2, 4 and 5.

(b) Solar panels 1, 3 and 6.

(c) Structure.

(d) Internal parts.

Source: The author

An approximate view of the temperature field along the entire orbit may be obtained by averaging the spatial distribution values on each main part, as shown in Figure 48, valid for the

case E-1/2.

Figure 48 – The average temperature of the main parts of the CubeSat for case E-1/2

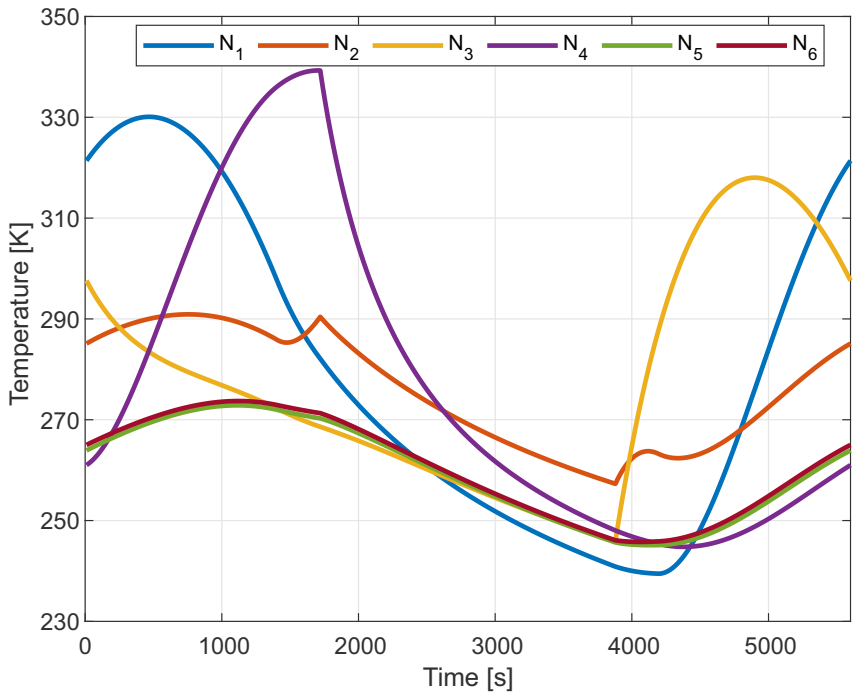

(a) Solar panels.

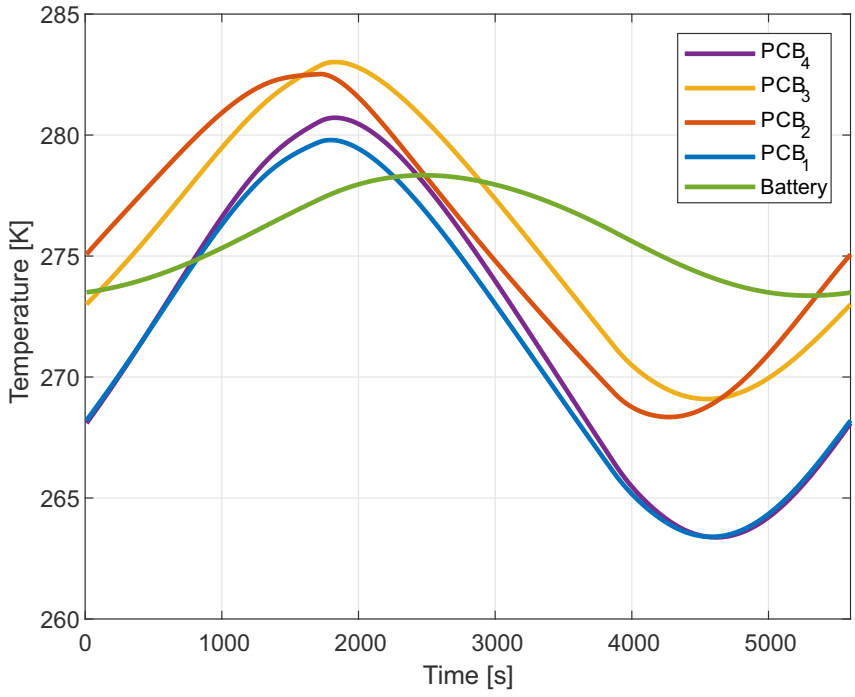

(b) PCBs and battery.

Source: The author

As cited above, at 1720 s occurs the maximum temperature gradient, which is the instant before the eclipse starts, while the minimum gradient is in the last instant of the eclipse, at 3880 s. The peak at 1720 s is around 340 K, 20 K colder than the observed in Figure 46a, resulting from the spatial averaging. As observed in Figure 25, side 1 receives more radiation in the beginning of

the orbit, resulting in maximum temperature for this side in that instant. However, the maximum overall temperature is achieved by side 4 because it is already warmer when the solar radiation starts to raise its temperature.

In comparison, side 3 has similar incoming radiation to side 4, but it is colder than side 4 when the solar flux heats it. Side 2 stays warmer than other sides near the end of the eclipse because it receives more radiation from the Earth due to its projection towards that source. The minimum value occurs on solar panel 1 because it does not receive any radiation from the Sun or the Earth during the eclipse, even entering the eclipse hotter than sides 3, 5, and 6. Sides 5 and 6 have the same thermal behavior because their projection towards the radiation sources are identical. These two surfaces do not have significant variations because they do not receive solar radiation, only albedo and emission from the Earth.

As observed in Figure 43a, the bolts of aluminum passing through the PCBs connect solar panels 5 to 6, serving as a thermally conductive path for inner parts. The internal components' temperature shown in Figure 48b oscillates less than the parts exposed to external radiation sources, and they are hotter than sides 5 and 6. The bottom PCB_1 and top PCB_4 have similar curves, always colder than the intermediate PCB_2 and PCB_3. These parts' location can explain the reason for it, as the influence of heat transfer by radiation from usually hotter sides 1, 2, 3, and 4 is greater in the intermediate PCB_2 and PCB_3. The peak of temperature occurs first at PCB_2, while the peak for PCB_1 and PCB_4 are the last, few seconds after PCB_3. These phase shifts increase among their minimum temperature values, but the order of occurrence remains. The hypotheses for the shift between them come from their different exposition towards the satellite's sides.

The temperature shift between PCB_2 and PCB_3 results from bigger thermal inertia of the battery on top of PCB_2. Interesting to notice an elevation of the battery's temperature even after several minutes of the eclipse beginning. The battery's temperature is strongly related to the heat transfer by conduction with PCB_2, so the battery's temperature keeps rising as long as the temperature of PCB_2 is higher than the battery's. The same conclusion is evident when the battery's temperature keeps falling after the eclipse and only raises if the temperature of PCB_2 is greater than the battery's. The small swing in the battery's temperature also can be explained by its greater thermal inertia (ϱc) than the PCBs.

In Figure 49 there are the temperature ranges, the average temperatures, and the temperatures at the central point (T_p) of each side and battery, obtained from the FVM simulation, based on case E-1/2. From this plot, it is evident that T_{ave} and T_p are just a partial view of the CubeSat's temperature profile, without the expressive temperature gradients resulting from the low thermal conduction of the solar panel, already discussed in previous graphs. In this same figure, the curves obtained with the LPM formulation are plotted for different thermal resistances Z (parameter in Equation (3.4)). The LPM uses the same thermal properties of Table 6 and dimensions of the FVM mesh's main parts but discards PCBs and bolts. Except for $Z = 0.00$,

where there is no heat exchange between the solar panels and battery, the curves obtained with LPM are within or very close to the extreme values obtained with FVM. With $Z = 0.05$, the LPM curves approximate to the values found in the center of the component (T_p), while $Z = 0.10$ approaches the average value T_{ave}. The interval between curves with $Z = 0.05$ and $Z = 1E4$ reproduces the temperature range of the FVM, with both curves interchangeably touching the upper and lower bounds. With $Z = 0.00$, the battery does not exchange heat and, for this reason, maintains its initial temperature of 273 K. The other values of Z resulted in greater oscillations for all the Z coefficients compared to T_{ave} or T_p.

The CubeSat's simplification by 7 points can still follow the temperature tendency obtained with the FVM, even with the oversimplification of the heat transfer by conduction and radiation in the term Z. While the FVM simulation takes around 16 hours to finish the simulation, the LPM simulation only takes a few seconds. Nevertheless, the three-dimensional effects, absent in the LPM, are essential to fully understand what is going on in the satellite.

Figure 49 – Comparison of LPM and FVM (E-1/2 case)

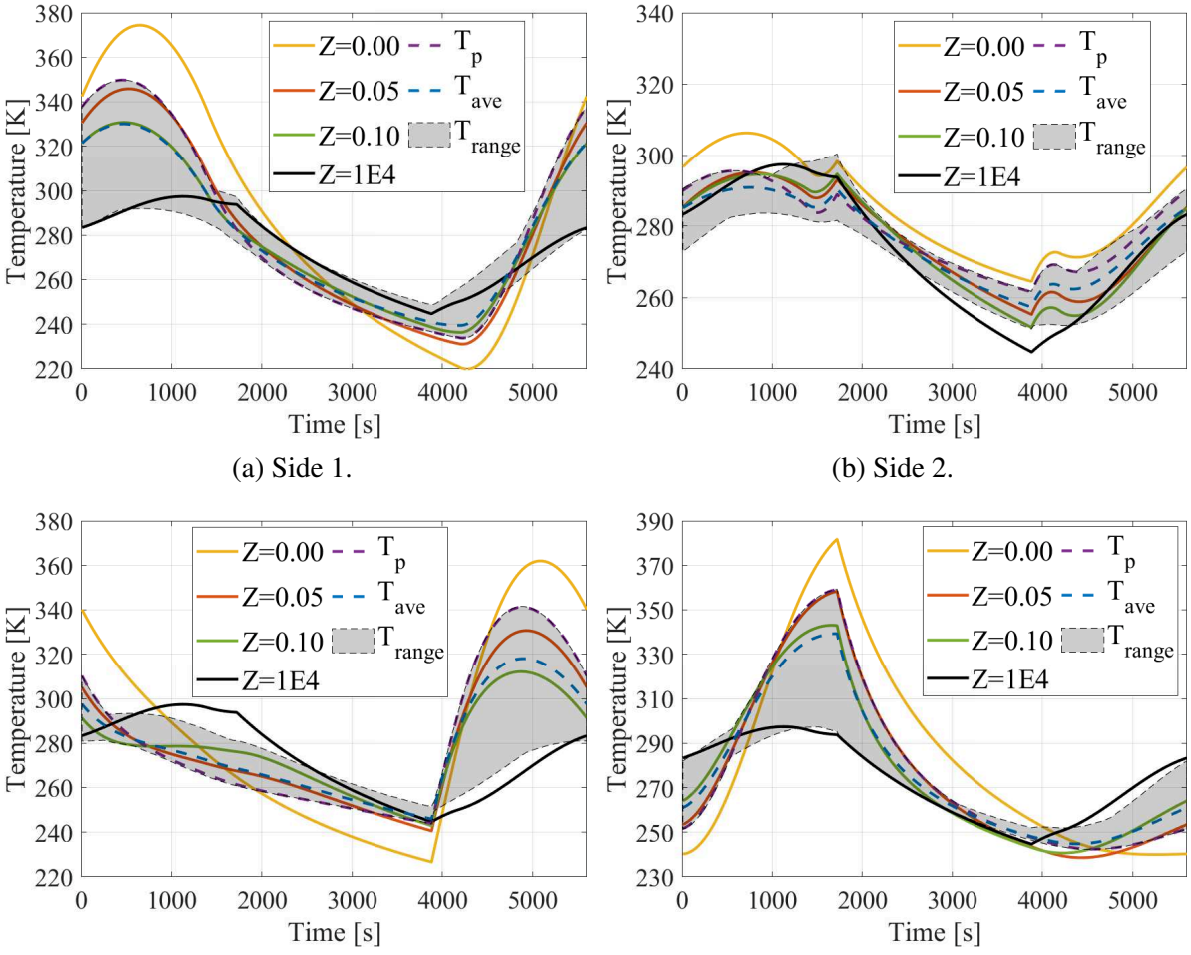

(a) Side 1.

(b) Side 2.

(c) Side 3.

(d) Side 4.

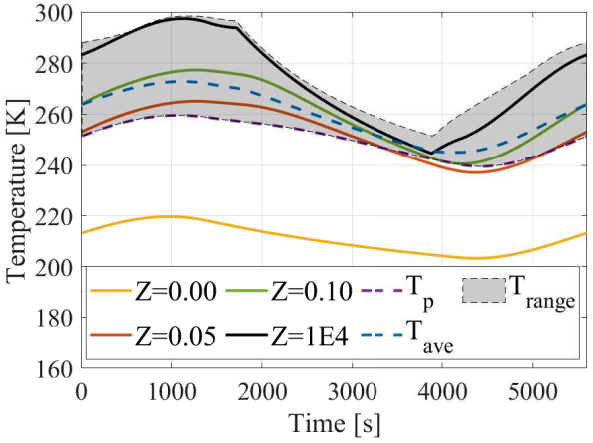

(e) Side 5.

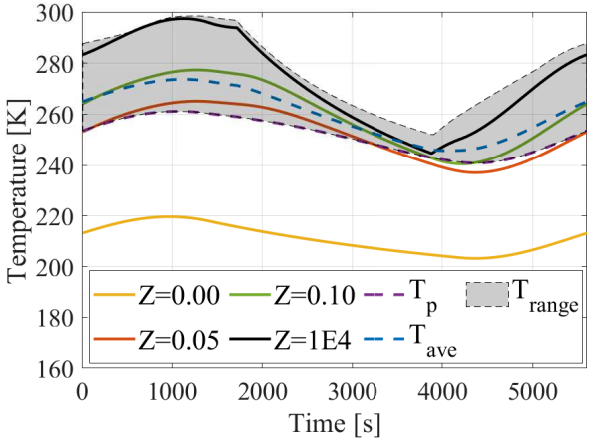

(f) Side 6.

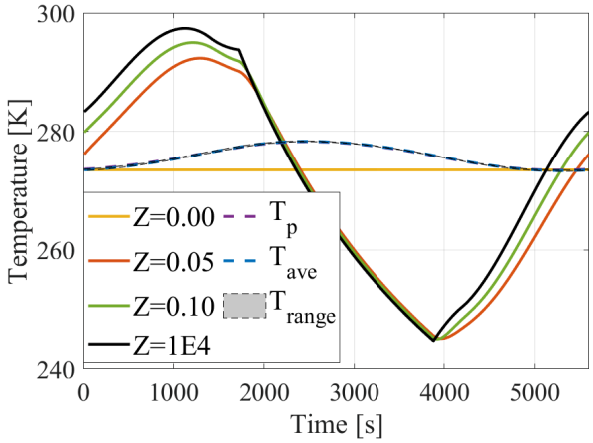

(g) Battery.

Source: The author

4.5.2 Zero internal radiation (E-0) and intermediate internal radiation (E-1/2) from the FVM

The results obtained in each main part of the CubeSat with zero internal radiative heat transfer (E-0) and those with intermediate internal heat exchange by radiation (E-1/2) are in Figure 50, both obtained with the Finite Volume Method. In these plots, both average (T_{ave}) and temperature range (T_{range}) are plotted. These figures show that around $\pm$15 K and $\pm$20 K of temperature difference exists in the average value and temperature range of the component, respectively, by changing from zero emissivity to 0.5. The values obtained with zero emissivity were overestimated in the hottest regions and underestimated in the coldest areas compared to the case with emissivity equal to 0.5. For those solar panels with moderate temperature, for example, sides 2, 5, and 6, the effect from changing the internal surface properties is less evident, although the zero emissivity results in lower minimum temperatures.

Considering the PCBs, the temperature ranges are quite close between E-0 and E-1/2 for the hottest levels outside the eclipse and the minimum temperatures inside the eclipse, shown in Figure 51. On the other hand, the zero emissivity case (E-0) underestimates the maximum levels of intermediate PCB_2 and PCB_3 inside the eclipse. Outside the eclipse, it underpredicts minimum

Figure 50 – Temperature range and average temperature of solar panels for the cases: E-1/2 (with internal heat transfer by radiation: $\varepsilon = 0.5$); E-0 (without internal heat transfer by radiation: $\varepsilon = 0$)

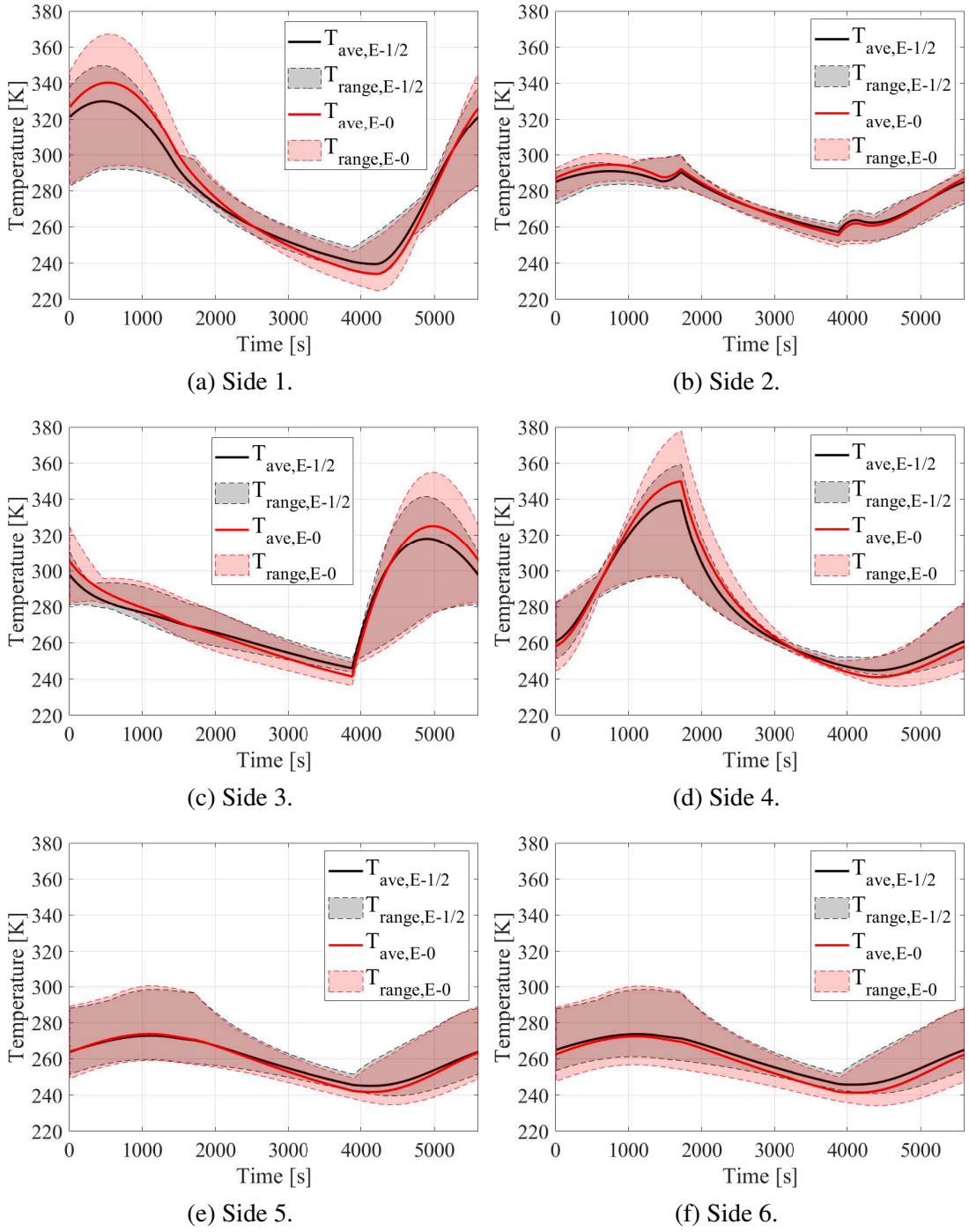

(a) Side 1.

(b) Side 2.

(c) Side 3.

(d) Side 4.

(e) Side 5.

(f) Side 6.

Source: The author

levels of PCB_1 and PCB_4, and almost always underestimates the lower limits of PCB_2 and PCB_3. The introduction of internal radiation increases the average temperature of intermediate PCB_2, PCB_3 and battery, so does the variation of temperature range of PCB_1 and PCB_4. It was expected because more heat could arrive on these internal parts when there is internal heat transfer by radiation, especially when the walls' temperature is hot. For the inside parts, the

cavity temperature is more important than a single wall, which explains the peak of temperature in the PCBs around 1100 s, before the CubeSat's maximum absolute temperature at 1720 s (solar panel 4). For both scenarios of internal boundary conditions, the temperature gradient in the battery is narrow, explained by its greater thermal conductivity (κ) when compared to the other parts.

Figure 51 – Temperature range and average temperature of internal parts for the cases: E-1/2 (with internal heat transfer by radiation: $\varepsilon = 0.5$); E-0 (without internal heat transfer by radiation: $\varepsilon = 0$)

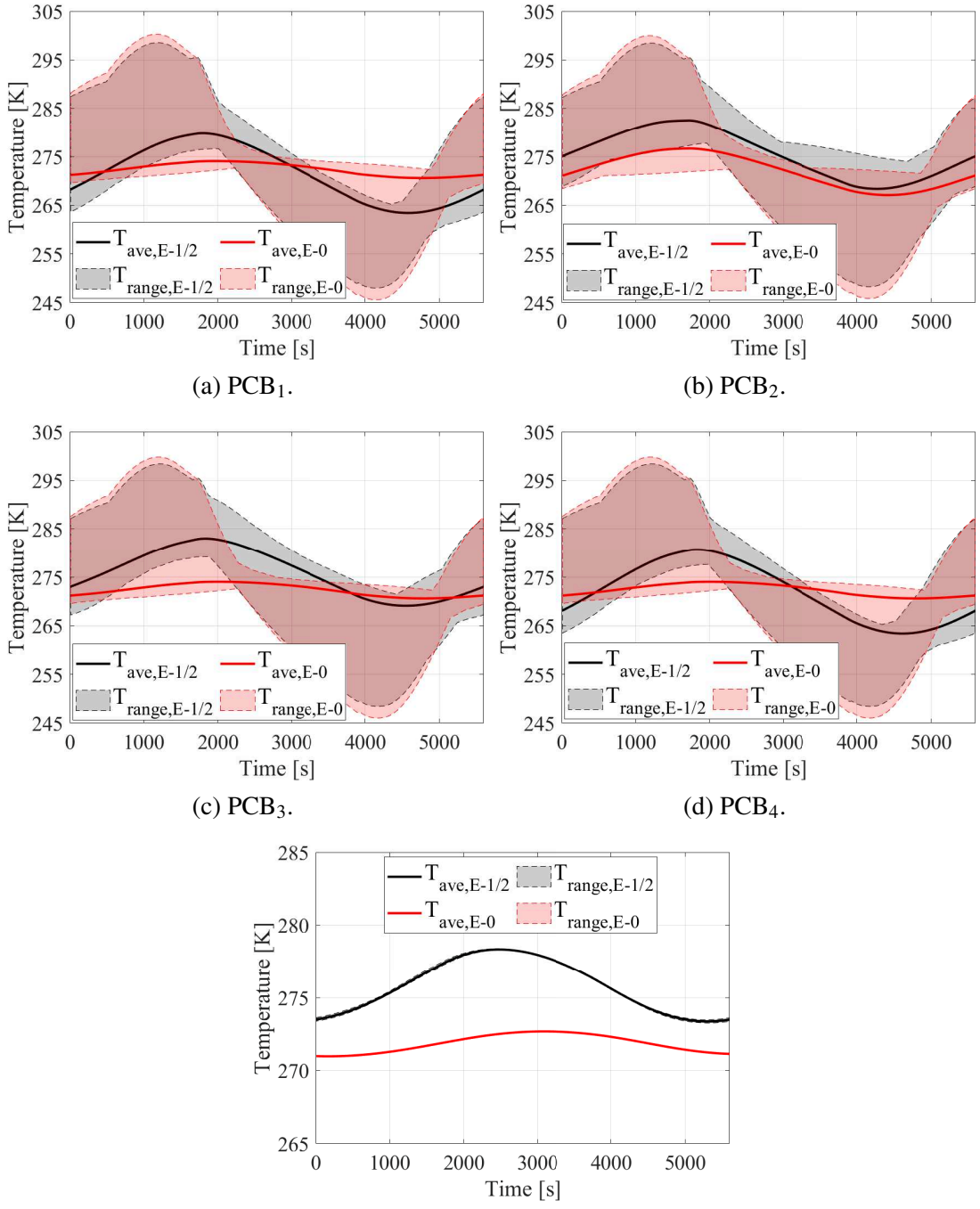

(a) PCB_1.

(b) PCB_2.

(c) PCB_3.

(d) PCB_4.

(e) Battery.

Source: The author

4.5.3 Maximum internal radiation (E-1) and intermediate internal radiation (E-1/2) from the FVM

Figure 52 shows the results of the case with maximum internal emissivity (E-1) together with the intermediate condition of emissivity (E-1/2), both from the Finite Volume Method.

Figure 52 – Temperature range and average temperature for the solar panels of cases: E-1/2 (with internal heat transfer by radiation: $\varepsilon = 0.5$); E-1 (with maximum internal heat transfer by radiation: $\varepsilon = 1$)

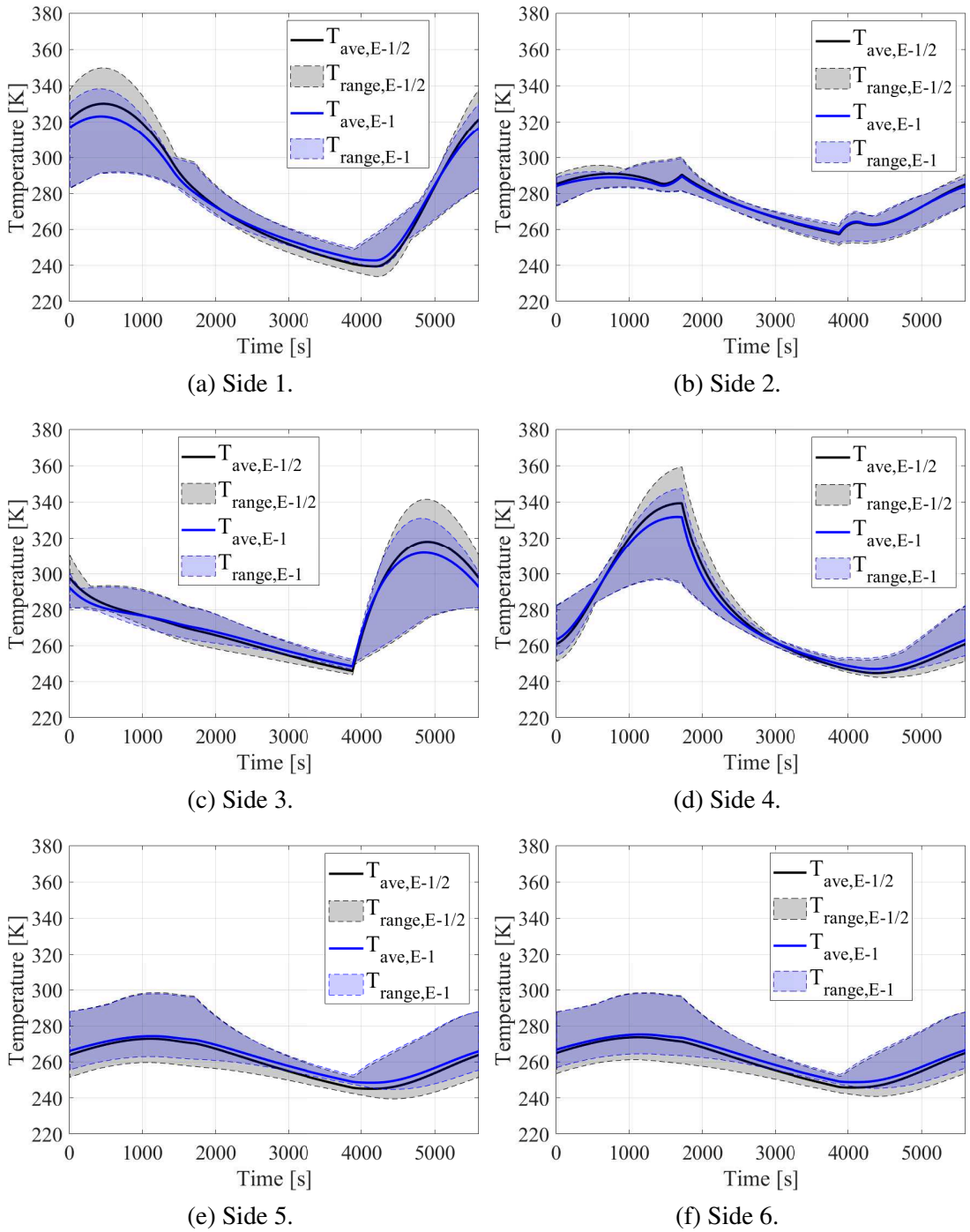

(a) Side 1.

(b) Side 2.

(c) Side 3.

(d) Side 4.

(e) Side 5.

(f) Side 6.

Source: The author

In general, the curves of E-1/2 and E-1 are closer than the pair E-1/2 and E-0. The temperature range of E-1 has an opposite behavior than case E-0, with extreme hot values being lower and extreme cold being greater than the results obtained with E-1/2.

When looking in Figure 53, with results for the internal parts of the CubeSat, there is and interesting additional increase of temperature in PCB_2 and PCB_3 around 1700 s and 5000 s.

Figure 53 – Temperature range and average temperature for the internal parts of cases: E-1/2 (with internal heat transfer by radiation: $\varepsilon = 0.5$); E-1 (with maximum internal heat transfer by radiation: $\varepsilon = 1$)

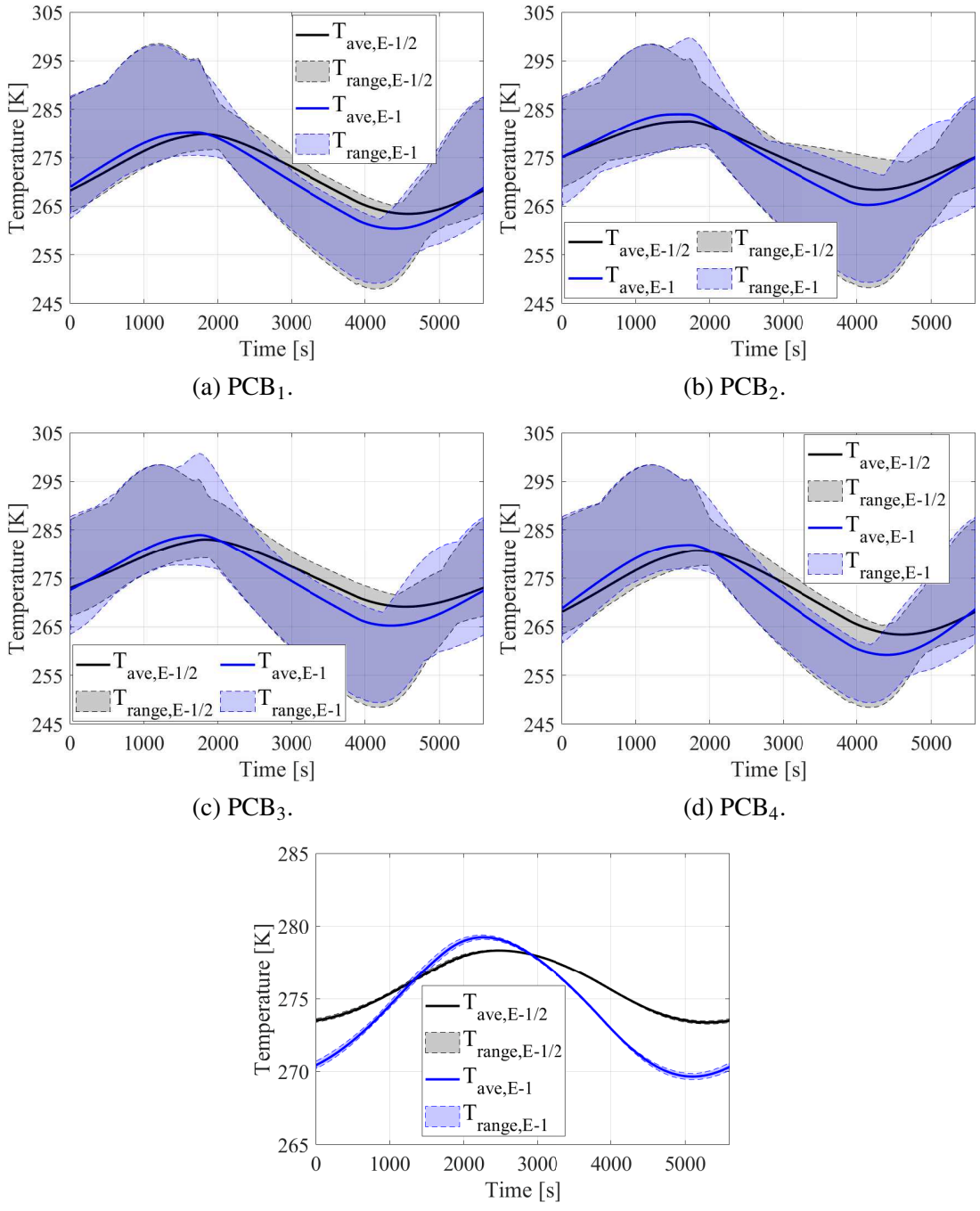

(a) PCB_1.

(b) PCB_2.

(c) PCB_3.

(d) PCB_4.

(e) Battery.

Source: The author

The probable cause of that is the greater influence of solar panels 4 and side 3, respectively, caused by the increase in the internal emissivity. The maximum temperature of PCBs in the eclipse with maximum emissivity (E-1) is generally below the maximum levels obtained with the intermediate emissivity (E-1/2). Both cases reproduce similar minimum levels in the PCBs outside the eclipse, except near after the eclipse. Even increasing the emissivity value, the battery's temperature still presents a low spatial and temporal temperature gradient, which evidences the stronger superiority of its heat transfer by conduction with PCB_2 than radiative processes.

4.5.4 Statistical distribution of results

Figure 54 summarizes the average fields of the entire orbit obtained with the FVM, for each part and case, into boxplot and average values (pink diamond). The non-symmetrical temperature distribution is more evident for solar panels with more significant temperature gradients (solar panels 1, 3, and 4). Since the quartile below the median is shorter than the above, the CubeSat spends most of the time closer to its minimum temperature value than its maximum.

Figure 54 – Temperature distribution of the main parts, obtained with FVM for each case of internal emissivity. The average value is the pink diamond and the red line is the median

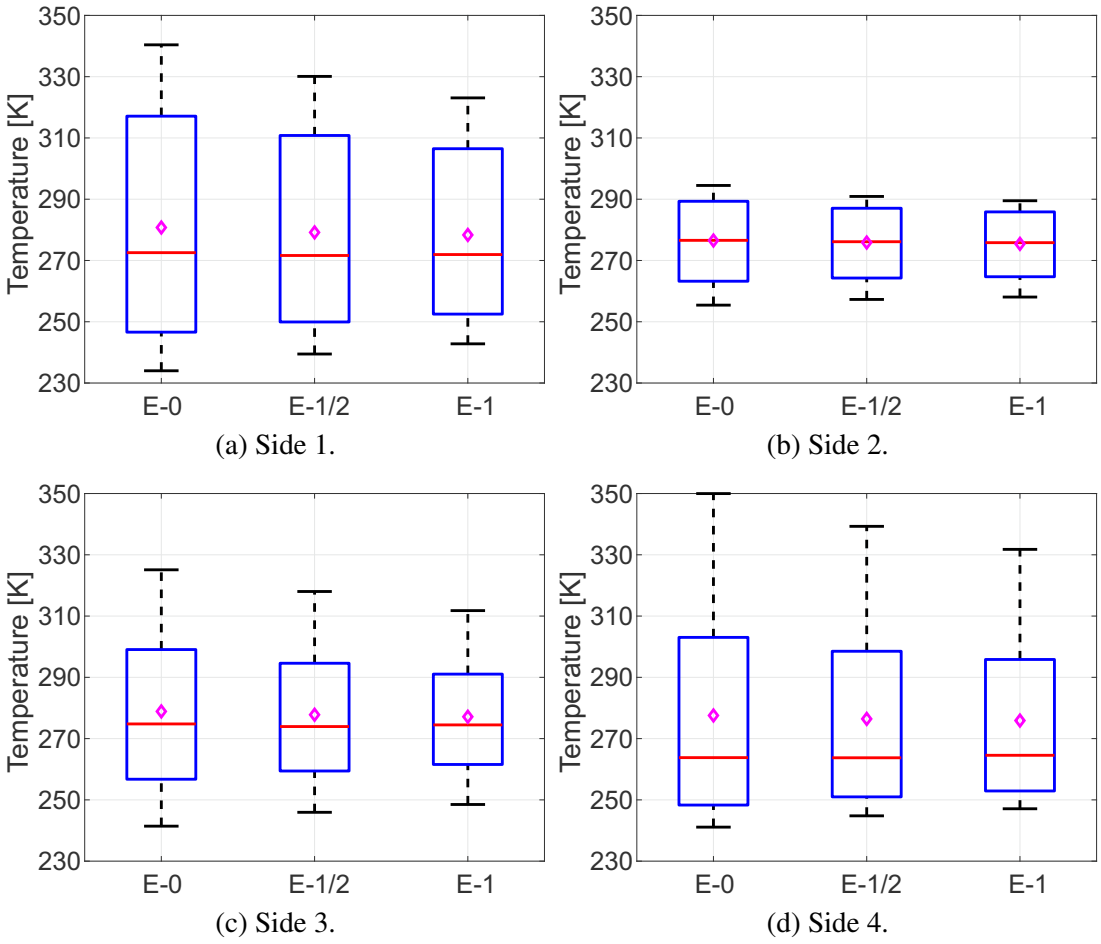

(a) Side 1.

(b) Side 2.

(c) Side 3.

(d) Side 4.

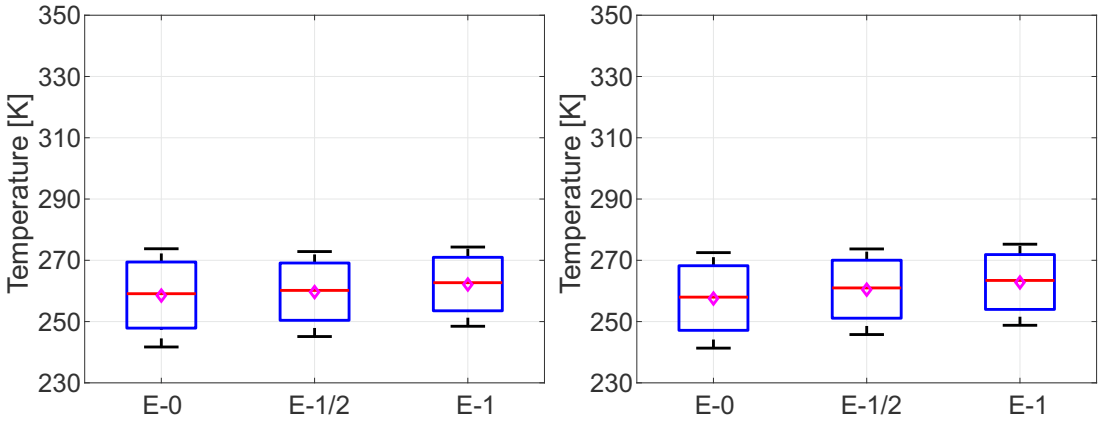

(e) Side 5. (f) Side 6.

Source: The author

As already observed, the case without internal heat transfer by radiation (E-0) has the greatest temperature differences, while the case of maximum internal emissivity (E-1) has the narrowest ranges. However, the average temperatures are essentially constant for the solar panels, with sides 5 and 6 having the minimum levels. The medians are lower than the panels' average with the most significant temperature gradients, namely panels 1, 3, and 4.

When the internal components are assessed, in Figure 55, the opposite happens. The zero emissivity condition creates smaller temperature gradients, while the upper and bounder values move away from each other as the increase in the emissivity enhances the internal heat transfer. The difference by assuming maximum emissivity ($\varepsilon = 1$) and minimum ($\varepsilon = 0$) may reach up to 10 K for the internal parts and around 20 K for the externals.

Figure 55 – Temperature distribution of the main parts, obtained with FVM for each case of internal emissivity. The average value is the pink diamond and the red line is the median

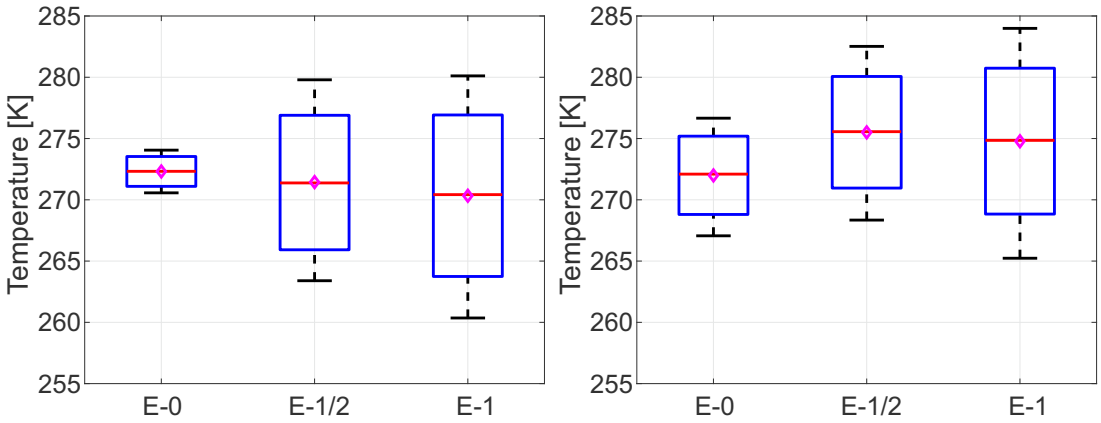

(a) PCB_1. (b) PCB_2.

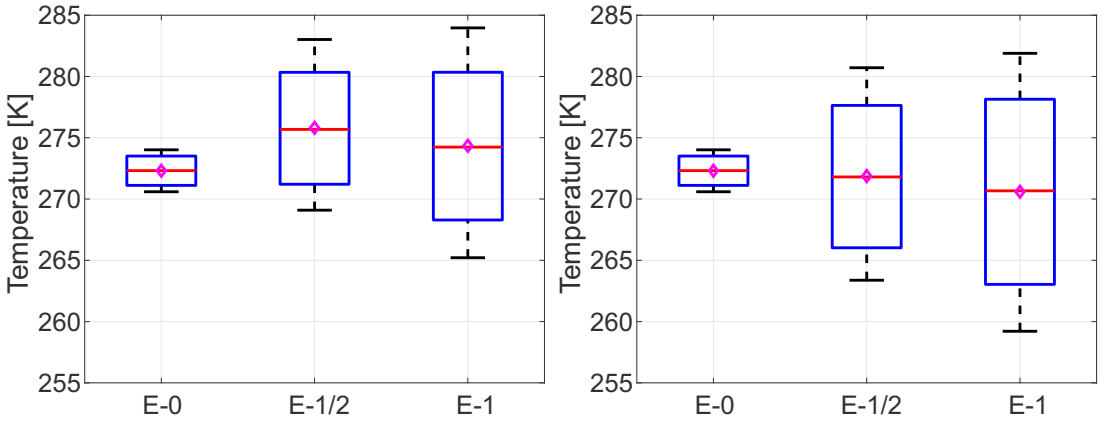

(c) PCB_3.

(d) PCB_4.

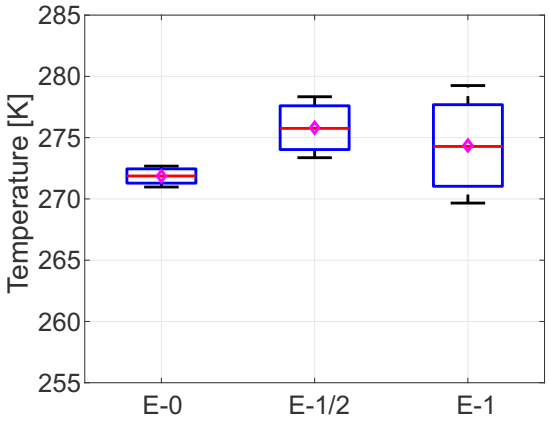

(e) Battery.

Source: The author

4.6 ILLUSTRATIVE APPLICATION

This section presents further applications of previous thermal and irradiance models, with introduction of additional elements in the simulation.

4.6.1 Heat pipes in CubeSats

Heat Pipe (HP) is a closed device that transports heat based on two-phase flow with high effective thermal conductivity, without electrical power and no moving parts. Accordingly to Peterson (1994), despite certain limitations, a heat pipe may be regarded as a synergistic engineering structure that is equivalent to a material having thermal conductivity, greatly exceeding that of any known metal. The main characteristics of general heat pipes are the high heat transfer under a relatively low-temperature gradient along the tube, operation in a micro-gravity environment, and a compact configuration, resulting in a far superior energy-to-weight ratio compared to pure metallic bars. These capabilities originate from the latent heat of the working fluid and capillary forces through the wicks (CHEN et al., 2016).

In a HP, there are three distinguished sections: evaporator, adiabatic, and condenser. Figure 56 shows these main parts. Usually made of a metallic material, the HP consists of a

sealed hollow tube with a capillary structure known as a wick in the internal walls, and a working fluid (GILMORE; DONABEDIAN, 2002; ZOHURI, 2016). The air in the tube is extracted to make a vacuum, and then a working fluid is inserted into it. HP works in a closed biphasic cycle, and only liquid and pure vapor coexist in a saturated condition. The heat source is connected in the evaporator section and the heat sink in the condenser section. When heat is added in the evaporator section, the fluid absorbs heat and begins to evaporate. The vapor then moves to the opposite side (condenser section) at colder and lower pressure, transporting with itself the latent heat. There, the fluid exchanges heat with the lower temperature of the region and become liquid again. The wick capillarities assist the return of fluid to the evaporator section, creating a loop (PAIVA, 2011). Due to its operation, the heat pipe is not a heat sink but a heat transfer device, and for this reason, it must be exposed to some external heat sink and heat source to work properly.

Figure 56 – Conventional heat pipe

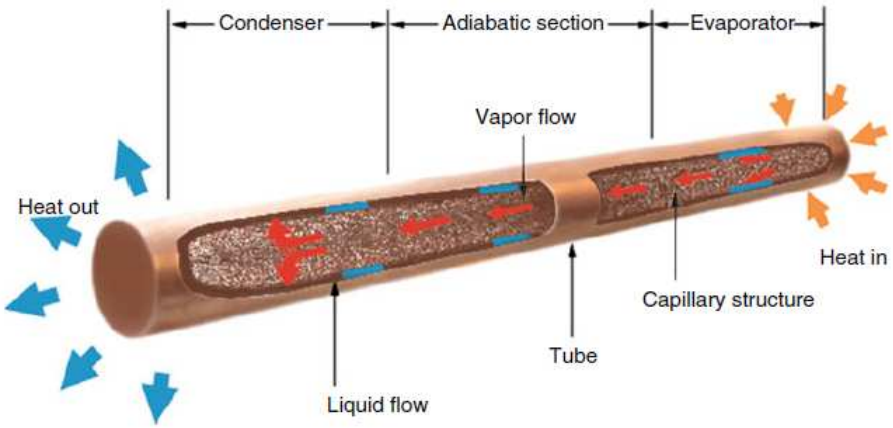

Source: Zohuri (2016)

To demonstrate the capacity of heat pipes for CubeSats missions through the proposed irradiance and thermal models, a simulation of the CubeSat 1U was run with a heat pipe connecting the opposite solar panels 3 and 4. In this case, the fluid flow was not solved, and a high thermal conduction coefficient was attributed to a solid bar made. The simulation has following parameters:

- The length (L) of adiabatic section has 90 mm;
- The length of the evaporator has 30 mm;
- The length of the condenser has 30 mm;
- The thermal contact resistance is neglected;
- The cross-section area (A) of the HP has 6x5 mm;
- The thermal conductivity (k) of the heat pipe is 10000 W/m.K;

- The thermal resistance (L/kA) of the HP is 0.33 K/W;
- The position and contact area of the heat pipe and solar panels are illustrated in Figure 57;
- The emissivity of internal surfaces is 0.5, including the HP;

Figure 57 – Schematic view of the simulation with heat pipe

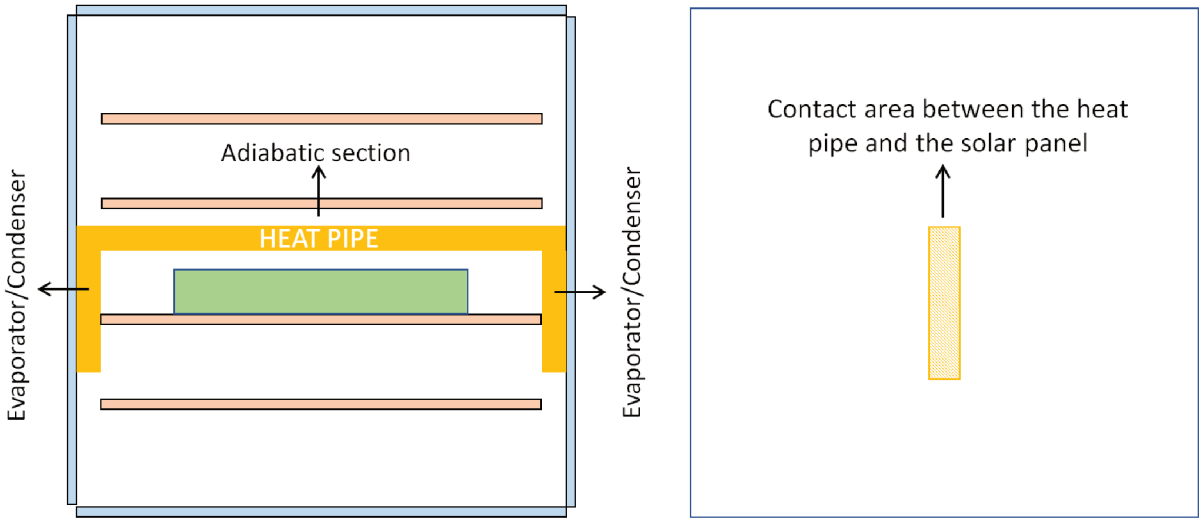

(a) The arrangement of the heat pipe. (b) Side view of heat pipe and solar panel.

Source: The author

Initially, the simulation was performed using the attitude of Nadir and orbit based on TLE1 (Table 2). Figure 58 shows the temperature in two different instants of the orbit. At t=1720 s, there is the biggest temperature difference between solar panels 4 and 3, with 4 as the hottest, while at 4720 s is the greatest temperature difference between solar panels 3 and 4, with 3 as the hottest. This situation evidences that for a satellite with spin, the evaporator and condenser sections of the heat pipe in this CubeSat change with time.

Figure 59 shows the average temperature on each solar panel along an orbit. Compared to the result without heat pipe (curves - -), the reduction in the temperature of warmer solar panels is noticeable, especially the solar panels with heat pipe (sides 4 and 3). These reductions happen because the panel opposite to the hottest always acts as a heat sink, and it rejects heat towards space.

Figure 60 shows the heat flux of an identical configuration of CubeSat and heat pipe from the previous case, for the same TLE1, but now with an attitude where three solar panels are equally exposed to the Sun (sides 2, 4, and 5), as already illustrated in Figure13e. The three opposite panels (sides 1, 3, and 6) are never exposed to the solar flux. Although the three sides 2, 4 and 5 are equally and constantly projected towards the Sun, they do not have the same curves because the albedo and infrared emission of the Earth act differently in each side. Despite the absence of direct solar radiation, the sides 1, 3 and 6 are exposed to albedo and infrared

Figure 58 – Temperature field for a CubeSat with a heat pipe connecting solar panels 3 and 4, under the attitude Nadir

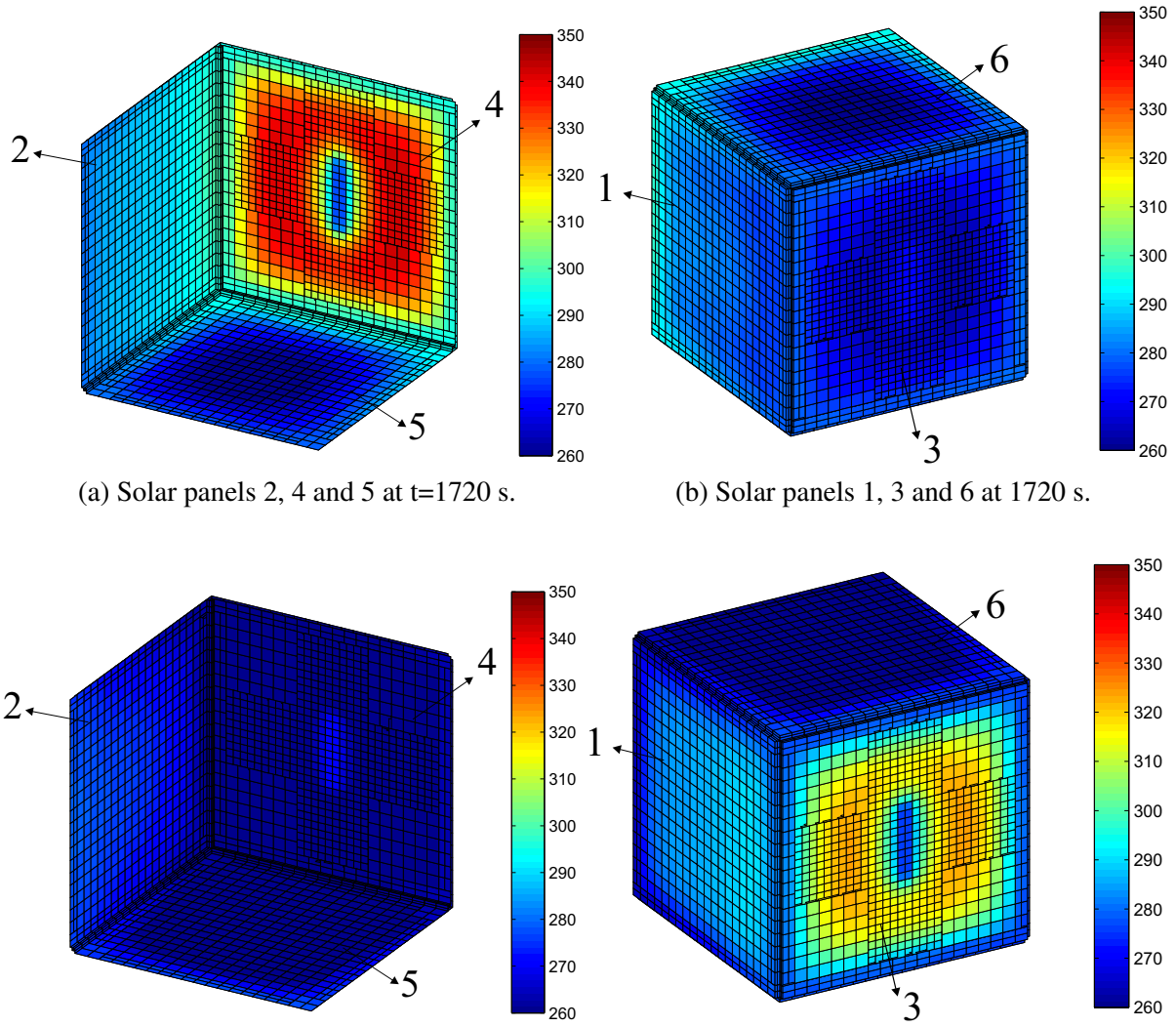

(a) Solar panels 2, 4 and 5 at t=1720 s.

(b) Solar panels 1, 3 and 6 at 1720 s.

(c) Solar panels 2, 4 and 5 at 4720 s.

(d) Solar panels 1, 3 and 6 at 4720 s.

Source: The author

radiation emitted by the Earth. Inside the eclipse, all the surfaces receive infrared radiation for some instants.

A view about the temperature field of this case is in Figure 61, for the last instant before the eclipse. Comparing to the Nadir case with HP (Figure 59), the maximum and minimum temperature levels are similar, but the temperature distribution are totally different. In this case, the three surfaces exposed to the Sun are hotter than those facing the outer space, as expected. Surface N_5 is highly warmer because at this instant it receives more albedo and infrared radiation from the Earth than surface N_2 and N_4. Again, the temperature gradient is evident, with the heat pipe's action more significant in the center of the hot solar panel 4 when compared to the same configuration without heat pipes (- -).

The impact in the average temperature of the solar panels are shown in Figure 62, for the case with the heat pipe (–) and without heat pipe (- -). In this case, the panels exposed to the

Figure 59 – The average temperature of the solar panels of CubeSat equipped with a heat pipe, for attitude Nadir. Curves (–) are for the simulation with heat pipe and curves (- -) are for the same case, but without heat pipes

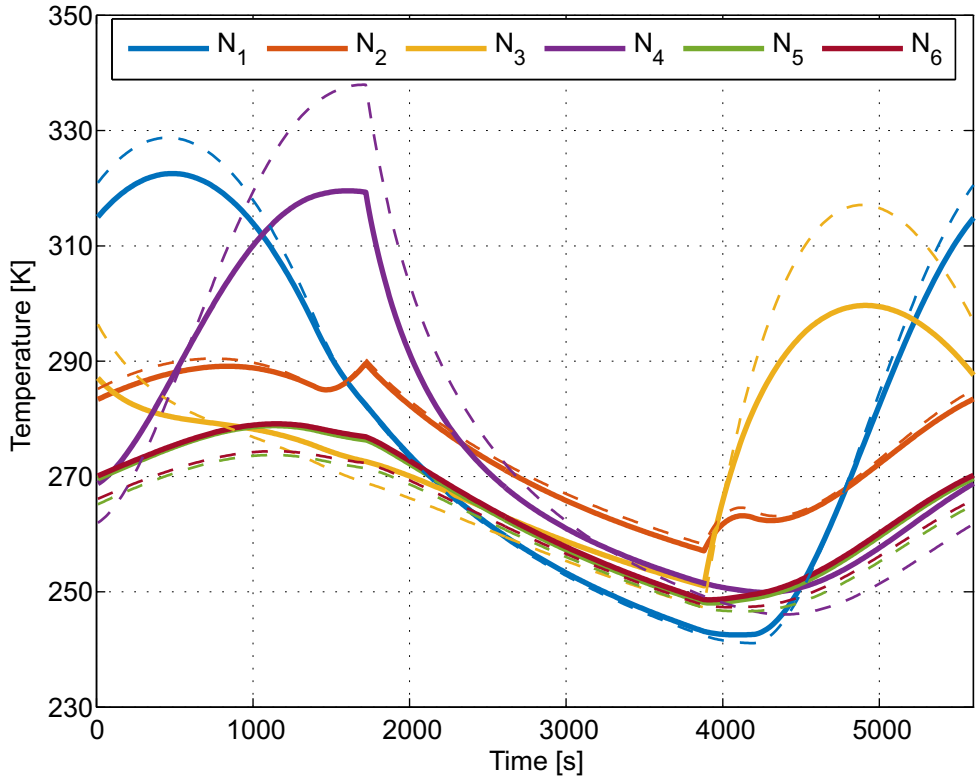

Source: The author

Sun have closer temperatures, and so do those opposed to them. The evaporator and condenser section of the heat pipe do not change of position, and they are always related to sides 4 and 3, respectively. The heat pipe's introduction still impacts the average temperatures; however, it is not too expressive as the previous case. In the portion of the plot after 3900 s, the side 4 has the greatest heat flux (Figure 60), however the presence of the heat pipe extracts heat from this panel and does not let it to be the hottest surface after the eclipse. For this attitude case, the temperature reduction is smaller than 10 K, while previous case it was around 20 K in some solar panels.

Therefore, from these two examples, the heat pipe simulated in this work can impact the temperature field of the CubeSat and is a potential solution to control the temperature and heat transfer between parts of the satellite.

4.6.2 Thermoelectric generator in a CubeSat

Since heat is a type of energy, the conversion of thermal into electrical energy is an exciting approach for improving energy efficiency in CubeSats. A technology used to transform heat into electrical energy is the Thermoelectric Generator (TEG), a mechanical device without moving parts that takes advantage of the Seebeck effect to obtain electrical energy from heat (LEE, 2016). Enormous spacecraft as Voyager, Pioneer, Galileo, Mars Science Laboratory, and

Figure 60 – Total irradiance flux for each side of the CubeSat. Orbit with TLE1, and attitude Sun_3

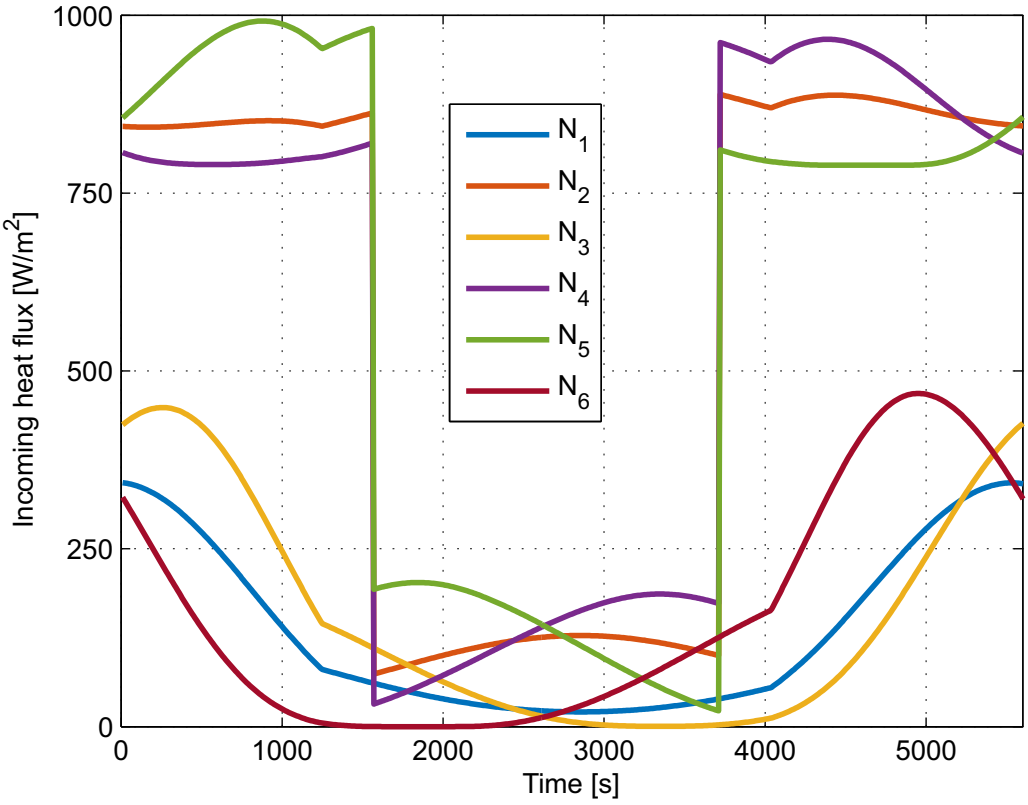

Source: The author

many others have already used this technology with satisfactory results.

Thermoelectric devices can convert thermal energy into electrical energy and vice-versa, a phenomenon quickly recognized when a thermocouple measures the temperature and translate the value into voltage. Figure 63 shows the main parts of a thermoelectric module. A TEG module usually consists of a number N_{TEG} of p-type and n-type semiconductor elements disposed electrically in series and thermally in parallel, both between a pair of high-thermal and low-electrical conductivity material often made of alumina or beryllia, forming a sandwich.

To perform the electrical simulation, the following items are assumed:

- Constant electrical properties;
- Equal length L in each p-type and n-type;
- Equal transverse area of p-type and n-type;
- Adiabatic boundary conditions on the laterals of the legs;
- Only the Seebeck effect;
- Constant Seebeck coefficient;

Figure 61 – Temperature field at t=1720 s for a CubeSat with a heat pipe connecting solar panels 3 and 4, for attitude Sun_3

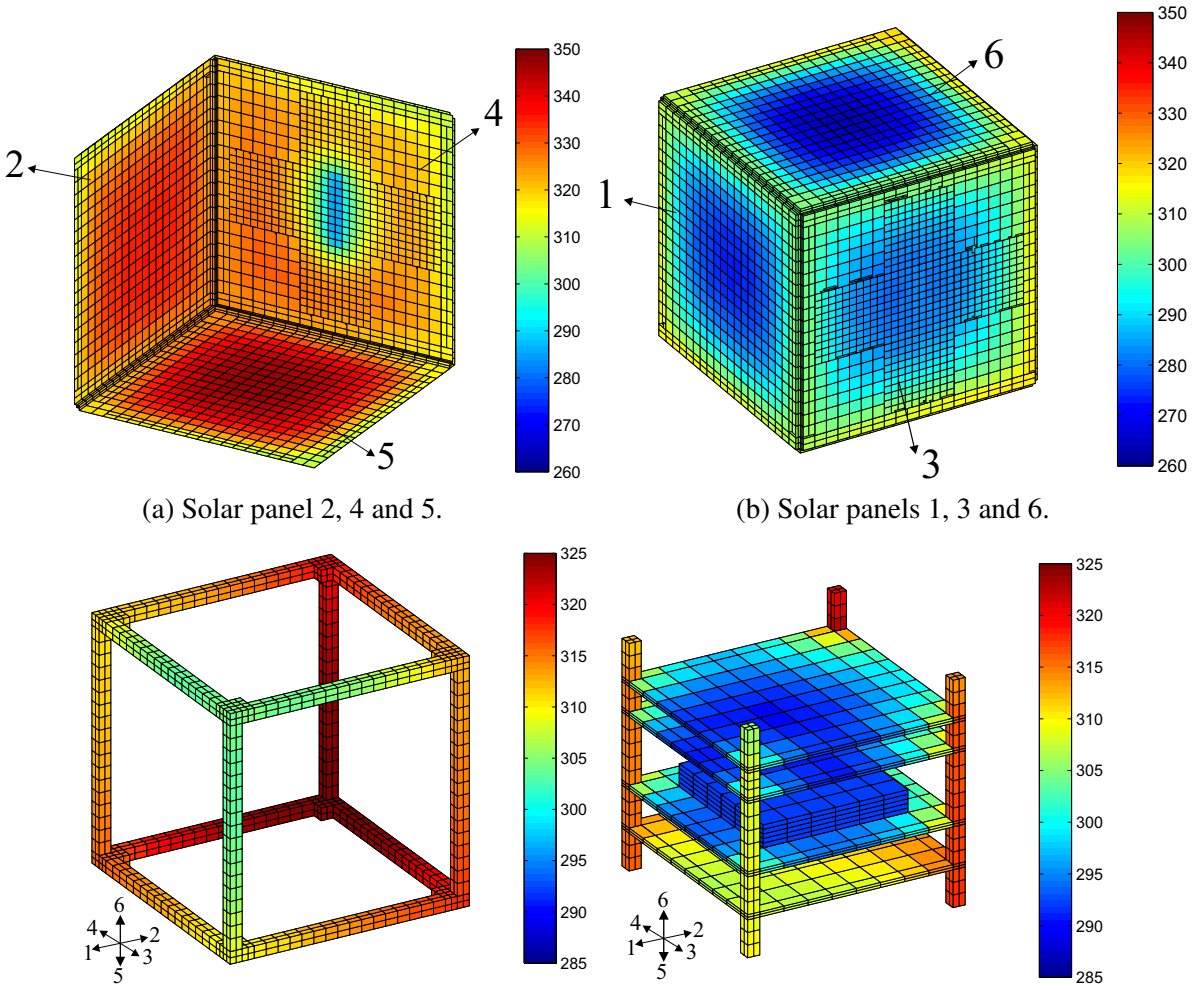

(a) Solar panel 2, 4 and 5.

(b) Solar panels 1, 3 and 6.

(c) Structure.

(d) Internal parts.

Source: The author

- Ideal thermal resistance;
- unidimensional heat transfer;
- The TEG is connected to an external load R_L.

For these assumption, the literature shows that (BORBA, 2018):

$$I_{TEG} = \frac{\alpha^* \left(T_H - T_C\right)}{R_L + R} \tag{4.1}$$

$$V_{TEG} = \frac{N_{TEG}\alpha^* \left(T_H - T_C\right)}{\frac{R_L}{R} + 1} \left(\frac{R_L}{R}\right) \tag{4.2}$$

$$W_{TEG} = \frac{N_{TEG}\alpha^{*2} \left(T_H - T_C\right)^2}{R} \frac{\frac{R_L}{R}}{\left(1 + \frac{R_L}{R}\right)^2} \tag{4.3}$$

Figure 62 – The average temperature of the solar panels of CubeSat equipped with a heat pipe, for attitude Sun_3; Curves (–) are for the simulation with heat pipe and curves (- -) are for the same case, but without heat pipes

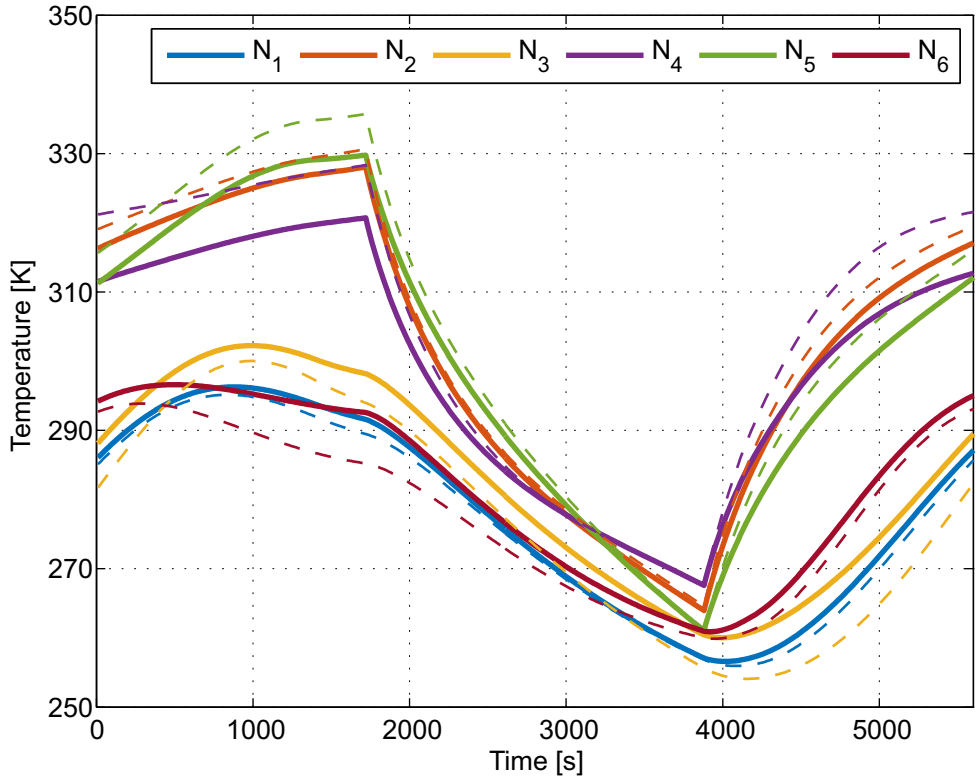

Source: The author

I_{TEG} is the current of generated by the TEG, α^* is the Seebeck coefficient, T_H is the temperature on the hot side of the TEG, T_C is the temperature in the cold side, R is the electrical resistance of the TEG, V_{TEG} is its voltage, and W_{TEG} its power.

To present a possibility of simulation from this irradiation and thermal model, a TEG was integrated in the CubeSat's geometry shown earlier and its electrical performance based on the temperature fields obtained through the simulation in the FVM. The TEG was attached to the inner side of the satellite, at the center of solar panel 4, and its parameters are:

The electrical results for the TEG are shown in Figure 64, for the attitude of Nadir and the orbit based on TLE1, and internal emissivity of 0.5 for all the surfaces, including the TEG.

It can be observed that the maximum current, voltage, and power are minimal, a consequence of the low-temperature difference between the sides of the TEG. While one face exchanges heat through conduction with solar panel 4, the other side is exposed to internal radiation heat transfer. For small areas and moderate temperatures, radiation is very limited, which could explain the poor performance of TEG.

As an attempt to improve the electrical outputs, a heat pipe was introduced in the simulation, and it connected one side of the TEG to the opposite solar panel 3. The results

Figure 63 – Main parts of a thermoelectric module

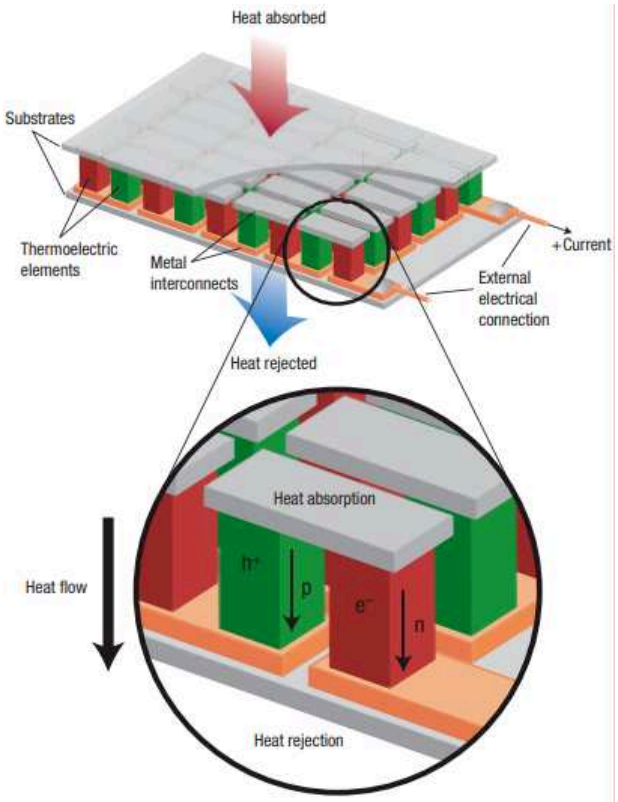

Source: Snyder and Toberer (2008)

Table 8 – Thermoelectric parameters

Variable	Value
Seebeck coefficient	215 μV/K
Thermal conductivity	1.6 W/mK
Number of semiconductor	241
Length	5 mm
Transversal area	30x30 mm^2
Load resistance	1 Ω
Resistance of the TEG	1 Ω

Source: Adapted from Ostrufka et al. (2019)

from this case are in Figure 65, where it is observed an improvement of around one order of magnitude in the current and voltage and two orders of magnitude in the power generation. However, simulation results indicate that they are still tiny, and CubeSat missions may not benefit from thermoelectric generators unless their heat source and rejection amplifies.

Figure 64 – Electrical outputs from a TEG's simulation in a CubeSat

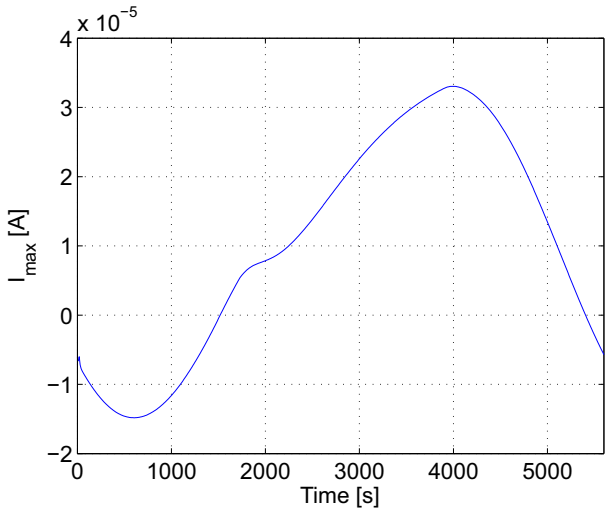

(a) Maximum current.

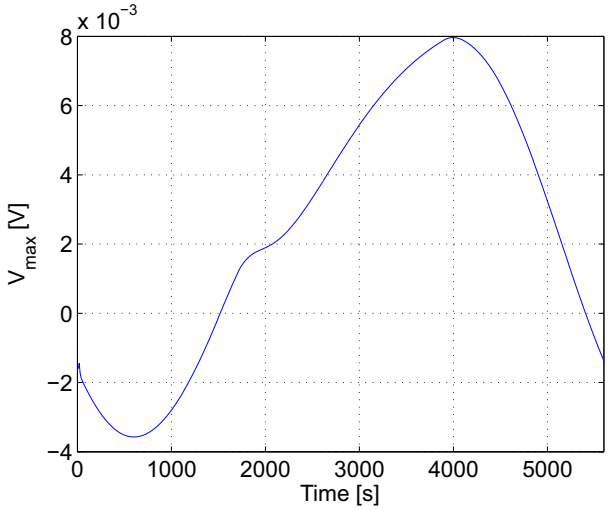

(b) Maximum voltage.

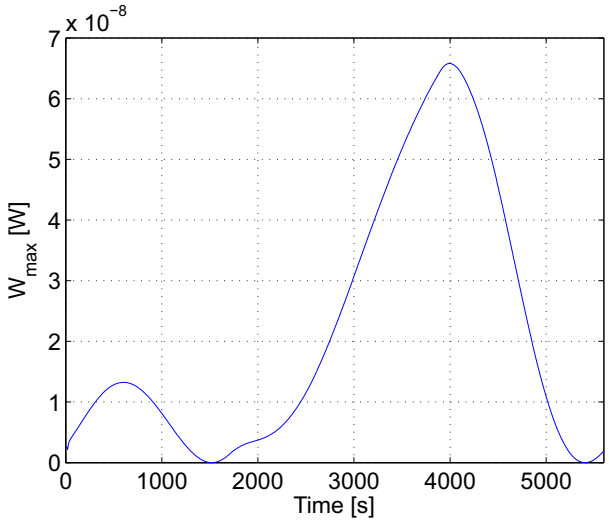

(c) Maximum power.

Source: The author

Figure 65 – Electrical outputs from a TEG's simulation connected to a heap pipe in a CubeSat

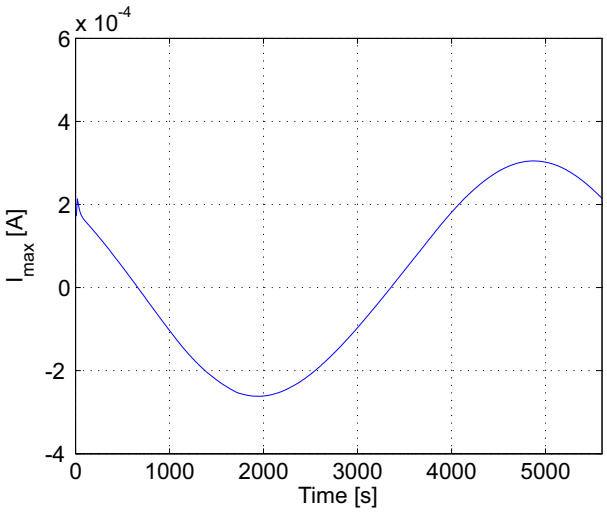

(a) Maximum current.

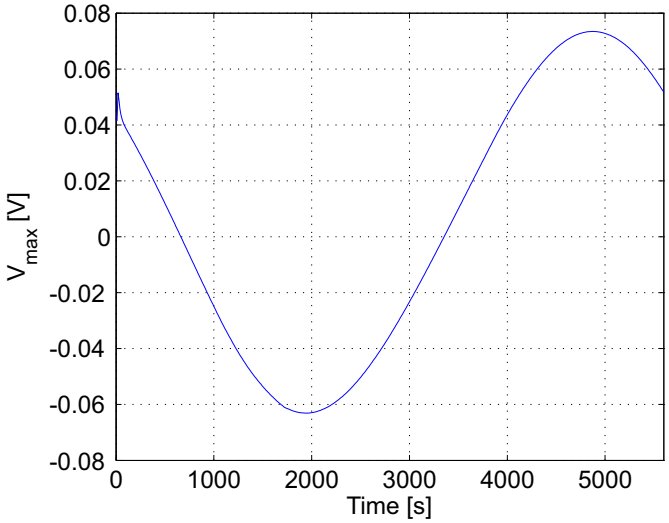

(b) Maximum voltage.

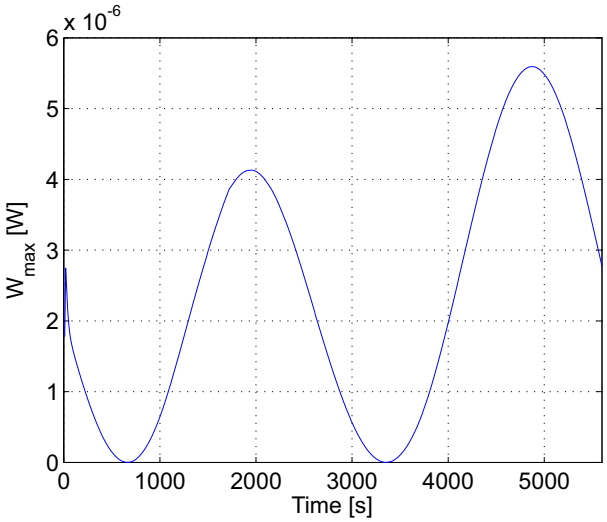

(c) Maximum power.

Source: The author

5 CONCLUSIONS AND FUTURE WORKS

In this thesis, irradiance and thermal models were developed as a framework for thermal simulation of CubeSats, a satellite's category with solid growth in the last years and great potential for expansion in the following years, so this work intends to serve as a support tool for these missions.

First, an irradiance model was implemented, which gives the external boundary conditions of the CubeSats' thermal problem for different scenarios of orbit and attitude. The inclusion of orbit perturbations was essential to simulate the orbit's dynamic along the satellite's operational cycle, and their results showed that they are responsible for changing the environmental conditions. A preliminary overview of irradiance field is obtained with β, the angle between the orbital plane and the Sun position. This angle is directly related to the orbit's fraction spent under the shadow of the Earth. The study of this angle and its impact in the irradiance fields are essential to comprehend the thermal conditions that the satellite will be exposed in orbit. The attitude is also another factor of substantial importance and rules the CubeSat's external surfaces' exposition towards the heat sources. The simulated cases illustrated that irradiation's diverse scenarios could be obtained for the same satellite, resulting in different thermal fields.

Then, a thermal simulation was built employing the Finite Volume Method (FVM), which accounted for the irradiance model to give the external boundary conditions, and included the internal heat transfer by radiation through the Gebhart Method. The CubeSat's internal cavity had printed circuit boards and batteries that partially blocked the view between them and the solar panels, reason for the inclusion of a method to predict these obstructions.

This work has simulated the irradiance and thermal scenarios dedicated to a typical CubeSat 1U, although this methodology can be extended to other CubeSat sizes without loss of generality. The results highlighted the importance of including the internal radiation in thermal problems of CubeSats.

The boundary condition of inner surfaces varied from zero emissivity (E-0) to an intermediate case with $\varepsilon = 0.5$ on each internal part (E-1/2), and maximum emissivity equal to one for all the internal surfaces (E-1). The inner boundary conditions impacted the temperature field of both internal and external parts. For the components exposed to outer space, the case without internal heat transfer by radiation (E-0) reproduced greater maximum levels outside the eclipse and colder minimum values in the eclipse than the case with the internal emissivity of 0.5 (E-1/2). For the case with internal zero emissivity (E-0), the internal parts receive less heat than case E-1/2 and have lower temperatures for most of the time. Case E-1 resulted in the shortest temperature peaks and gradients of the external parts, an expected result because the solar panels could exchange heat through their two opposite surfaces. By statistically comparing

the temperature distribution in each case, there is no significant variation among the entire orbit's average values, only in their upper and bounder limits.

The temperature field obtained with the FVM was compared to a Lumped Parameter Method (LPM), a simple and consequently fast formulation to collect results of heat transfer. The attribution of a single point for each main part of the satellite in the LPM was able to capture the overall behavior of FVM, and an adjustment in the thermal resistance coefficient (Z) could adhere to the range, central point, or average values obtained with FVM simulations. For $Z = 0.00$, valid for none heat transfer among the solar panels and the battery, the temperature levels are beyond the extreme values of the FVM. In contrast, $Z = 0.05$ and $Z = 1E4$ reproduce quite well the temperature range of the FVM, with both values of curves defining the superior and inferior extreme levels, depending on the instant of the orbit. With $Z = 0.05$ and $Z = 0.10$, the LPM approaches the central-point and average values of the FVM formulation, respectively. However, there are appreciable three-dimensional fields that can not be reproduced with the simple LPM approach.

The internal radiation boundary condition considered in this work can be helpful for other formulations, not necessarily FVM. Its inclusion may assist the validation of passive thermal controls centered on the surface emissions, such as paintings, coats, and Multi-Layer Insulation (MLI), although they did not exist in this work. Two possibilities of further analysis achievable with the current framework were illustrated. The preliminary results regarding heat pipes show its potential use for heat transfer between solar panels and temperature reduction, a positive solution to control components' temperature with overheating problems, like solar panels and batteries. The initial attempt to convert the heat from the satellite into electricity through the thermoelectric generator (TEG) did not result in appreciable power TEGs, but it illustrates another framework's potential.

To further validation of the framework presented here, one must rely on data that are not readily available. The temperature data is a fraction of the required information for complete validation because the heat transfer is affected by the CubeSat's design, its materials, orbit, attitude, and electrical operation modes. Therefore, it is understood that the validation of the models will become more comfortable with the advent of more CubeSat's launches, as more data are available in the literature.

As future work, the following are suggested:

- To minimize the error in the obstruction of partial shadowed surfaces. There are further techniques to deal with this problem, which maps these occurrences and uses geometry to calculate the fraction of a surface that is really obstructed;
- To add the heat dissipation of electronic components of the CubeSat based on the execution of tasks. The electrical operation of the CubeSat is not an ideal process, and heat is

generated in diverse parts of the satellite when electrical current passes by resistive materials;

- To use the irradiance and thermal simulation as a framework to test and evaluate the performance of passive and active thermal controls that are compatible with CubeSat missions, for example, heat pipes, phase-change material, electrical heater, and heat pumps.

BIBLIOGRAPHY

ANH, N. et al. Thermal radiation analysis for small satellites with single-node model using techniques of equivalent linearization. *Applied Thermal Engineering*, v. 94, p. 607 – 614, 2016. ISSN 1359-4311. Available from Internet: <http://www.sciencedirect.com/science/article/pii/S1359431115011989>.

ATALLAH, A. M. I. *A Implementation and Verification of a High-Precision Orbit Propagator*. Dissertação (Mestrado) — Cairo University, 2018.

AUNG, H. et al. Battery management system with state-of-charge and opportunistic state-of-health for a miniaturized satellite. *IEEE Transactions on Aerospace and Electronic Systems*, v. 56, n. 4, p. 2978–2989, 2020.

AURET, J.; STEYN, W. Design of an aerodynamic attitude control system for a cubesat. *62nd International Astronautical Congress 2011, IAC 2011*, v. 11, p. 9009–9017, 01 2011.

BATE, R.; MUELLER, D.; WHITE, J. *Fundamentals of Astrodynamics*. Dover Publications, 1971. (Dover Books on Aeronautical Engineering Series). ISBN 9780486600611. Available from Internet: <https://books.google.com.br/books?id=UtJK8cetqGkC>.

BEDNOVA, V.; YUMASHEV, M. Thermo-mechanical loads on a spacecraft in low earth orbits. *Acta Astronautica*, v. 150, p. 39 – 43, 2018. ISSN 0094-5765. Available from Internet: <http://www.sciencedirect.com/science/article/pii/S0094576518303497>.

BERG, L. K. et al. Fine-scale variability of observed and simulated surface albedo over the southern great plains. *Journal of Geophysical Research: Atmospheres*, v. 125, n. 7, p. e2019JD030559, 2020. Available from Internet: <https://agupubs.onlinelibrary.wiley.com/doi/abs/10.1029/2019JD030559>.

BERGMAN, T. et al. *Fundamentals of Heat and Mass Transfer*. Wiley, 2011. ISBN 9780470501979. Available from Internet: <https://books.google.com.br/books?id=vvyIoXEywMoC>.

BONNICI, M. et al. Analytical and numerical models for thermal related design of a new pico-satellite. *Applied Thermal Engineering*, v. 159, p. 113908, 2019. ISSN 1359-4311. Available from Internet: <http://www.sciencedirect.com/science/article/pii/S1359431118360733>.

BORBA, A. C. de. *Análise analítica e experimental de geradores termoelétricos aplicados à nanossatélites*. Dissertação (Mestrado) — Universidade Federal de Santa Catarina, 2018.

BRENNAN, M. et al. Effects of spectral albedo on solar photovoltaic devices. *Solar Energy Materials and Solar Cells*, v. 124, p. 111 – 116, 2014. ISSN 0927-0248. Available from Internet: <http://www.sciencedirect.com/science/article/pii/S0927024814000658>.

BULUT, M.; SOZBIR, N. Analytical investigation of a nanosatellite panel surface temperatures for different altitudes and panel combinations. *Applied Thermal Engineering*, v. 75, p. 1076 – 1083, 2015. ISSN 1359-4311. Available from Internet: <http://www.sciencedirect.com/science/article/pii/S1359431114009302>.

CAPDEROU, M. *Handbook of Satellite Orbits: From Kepler to GPS*. Springer International Publishing, 2014. (SpringerLink : Bücher). ISBN 9783319034164. Available from Internet: <https://books.google.com.br/books?id=1_68BAAAQBAJ>.

CHEN, X. et al. A review of small heat pipes for electronics. *Applied Thermal Engineering*, v. 96, p. 1 – 17, 2016. ISSN 1359-4311. Available from Internet: <http://www.sciencedirect.com/science/article/pii/S1359431115012946>.

CHIN, K. B. et al. Energy storage technologies for small satellite applications. *Proceedings of the IEEE*, v. 106, n. 3, p. 419–428, 2018.

CLARICOATS, J.; DAKKA, S. M. Design of power, propulsion, and thermal sub-systems for a 3u cubesat measuring earth's radiation imbalance. *Aerospace*, v. 5, n. 2, 2018. ISSN 2226-4310. Available from Internet: <https://www.mdpi.com/2226-4310/5/2/63>.

CORPINO, S. et al. Thermal design and analysis of a nanosatellite in low earth orbit. *Acta Astronautica*, v. 115, p. 247 – 261, 2015. ISSN 0094-5765. Available from Internet: <http://www.sciencedirect.com/science/article/pii/S0094576515001940>.

CORPINO, S.; STESINA, F. Verification of a CubeSat via hardware-in-the-loop simulation. *IEEE Transactions on Aerospace and Electronic Systems*, v. 50, n. 4, p. 2807–2818, 2014. ISSN 00189251.

CUI, Y.; MITOMI, Y.; TAKAMURA, T. An empirical anisotropy correction model for estimating land surface albedo for radiation budget studies. *Remote Sensing of Environment*, v. 113, n. 1, p. 24 – 39, 2009. ISSN 0034-4257. Available from Internet: <http://www.sciencedirect.com/science/article/pii/S0034425708002666>.

CURTIS, H. D. *Orbital Mechanics for Engineering Students*. Third. Boston: Butterworth-Heinemann, 2014. 751 p. ISBN 978-0-08-097747-8.

DEHBONEI, H.; LEE, S. R.; NEHRIR, H. Direct energy transfer for high efficiency photovoltaic energy systems part i: Concepts and hypothesis. *IEEE Transactions on Aerospace and Electronic Systems*, v. 45, n. 1, p. 31–45, 2009.

DIAZ, M. et al. New opportunities offered by cubesats for space research in latin america: The suchai project case. *Advances in Space Research*, v. 58, n. 10, p. 2134 – 2147, 2016. ISSN 0273-1177. Space and Geophysical Research related to Latin America - Part 2. Available from Internet: <http://www.sciencedirect.com/science/article/pii/S0273117716303106>.

EHLERT, J. R.; SMITH, T. F. View factors for perpendicular and parallel rectangular plates. *Journal of Thermophysics and Heat Transfer*, v. 7, n. 1, p. 173–175, 1993. Available from Internet: <https://doi.org/10.2514/3.11587>.

ESA/ESTEC. *Product and Quality Assurance Requirements for In-Orbit Demonstration CubeSat Projects*. 2013. <http://emits.sso.esa.int/emits-doc/ESTEC/AO8352_AD2_IOD_CubeSat_PQA_Reqts_Iss1_Rev1.pdf>.

ESCOBAR, E.; DIAZ, M.; ZAGAL, J. C. Evolutionary design of a satellite thermal control system: Real experiments for a cubesat mission. *Applied Thermal Engineering*, v. 105, p. 490 – 500, 2016. ISSN 1359-4311. Available from Internet: <http://www.sciencedirect.com/science/article/pii/S1359431116303167>.

FARHANI, F.; ANVARI, A. Effects of some parameters on thermal control of a leo satellite. *Journal of Space Science and Technology*, v. 7, n. 1, p. 13–24, 2014.

FILHO, E. M. et al. A comprehensive attitude formulation with spin for numerical model of irradiance for cubesats and picosats. *Applied Thermal Engineering*, v. 168, p. 114859, 2020. ISSN 1359-4311. Available from Internet: <http://www.sciencedirect.com/science/article/pii/S1359431119333459>.

FIREDEL, S. M. J. *Thermal Analysis of the CubeSat CP3 Satellite, Senior Project, San Luis Obispo, CA, USA (2011)*. 2011. Available from Internet: <https://digitalcommons.calpoly.edu/cgi/viewcontent.cgi?referer=https://scholar.google.com/&httpsredir=1&article=1054&context=aerosp>.

FORTESCUE, P.; SWINERD, G.; STARK, J. *Spacecraft Systems Engineering*. Wiley, 2011. ISBN 9781119978367. Available from Internet: <https://books.google.com.br/books?id=cCYP0rVR_IEC>.

GEBHART, B. Surface temperature calculations in radiant surroundings of arbitrary complexity—for gray, diffuse radiation. *International Journal of Heat and Mass Transfer*, v. 3, n. 4, p. 341 – 346, 1961. ISSN 0017-9310. Available from Internet: <http://www.sciencedirect.com/science/article/pii/0017931061900485>.

GILMORE, D.; DONABEDIAN, M. *Spacecraft Thermal Control Handbook: Fundamental technologies*. Aerospace Press, 2002. (Spacecraft Thermal Control Handbook). ISBN 9781884989117. Available from Internet: <https://books.google.com.br/books?id=-GYGlwG8PkUC>.

GOODE, P. R. et al. Earthshine observations of the earth's reflectance. *Geophysical Research Letters*, v. 28, n. 9, p. 1671–1674, 2001. Available from Internet: <https://agupubs.onlinelibrary.wiley.com/doi/abs/10.1029/2000GL012580>.

HANEVEER, M. R. *Orbital Lifetime Predictions: An assessment of model-based ballistic coefficient estimations and adjustment for temporal drag coefficient variations*. Dissertação (Mestrado) — Delft University of Technology, 2017.

HEIDT, M. et al. Cubesat: A new generation of picosatellite for education and industry low-cost space experimentation. 01 2000.

HOWELL, J.; MENGUC, M.; SIEGEL, R. *Thermal Radiation Heat Transfer, 5th Edition*. CRC Press, 2010. ISBN 9781439894552. Available from Internet: <https://books.google.com.br/books?id=FBjSBQAAQBAJ>.

KARAM, R. *Satellite Thermal Control for Systems Engineers*. American Institute of Aeronautics & Astronautics, 1998. (Progress in astronautics and aeronautics). ISBN 9781600864339. Available from Internet: <https://books.google.com.br/books?id=bzD4_hxupI4C>.

KIESBYE, J. et al. Hardware-in-the-loop and software-in-the-loop testing of the move-ii cubesat. *Aerospace*, v. 6, n. 12, 2019. ISSN 2226-4310. Available from Internet: <https://www.mdpi.com/2226-4310/6/12/130>.

KNAP, V.; VESTERGAARD, L. K.; STROE, D.-I. A review of battery technology in cubesats and small satellite solutions. *Energies*, v. 13, n. 16, 2020. ISSN 1996-1073. Available from Internet: <https://www.mdpi.com/1996-1073/13/16/4097>.

KOVÁCS, R.; JÓZSA, V. Thermal analysis of the smog-1 pocketqube satellite. *Applied Thermal Engineering*, v. 139, p. 506 – 513, 2018. ISSN 1359-4311. Available from Internet: <http://www.sciencedirect.com/science/article/pii/S1359431117350913>.

KRAMER, H. J. *SwissCube*. 2019. Acessed: 13-04-2019. Available from Internet: <https://directory.eoportal.org/web/eoportal/satellite-missions/s/swisscube>.

KRAMER, H. J. *ZACUBE-1 (South Africa CubeSat-1) / TshepisoSat*. 2019. Acessed: 07-05-2019. Available from Internet: <https://directory.eoportal.org/web/eoportal/satellite-missions/v-w-x-y-z/zacube-1>.

KRAUSE, F. C. et al. Implementation of commercial Li-ion cells on the MarCO deep space CubeSats. *Journal of Power Sources*, v. 449, p. 227544, feb 2020. ISSN 03787753. Available from Internet: <https://linkinghub.elsevier.com/retrieve/pii/S037877531931537X>.

KULU, E. *Nanosatellite and CubeSat Database*. 2019. Acessed: 07-05-2019. Available from Internet: <https://www.nanosats.eu>.

KULU, E. *Nanosats Database*. 2020. Available from Internet: <www.nanosats.eu>.

LANGER, M.; BOUWMEESTER, J. Reliability of cubesats-statistical data, developers' beliefs and the way forward. In: *2016 30th Annual AIAA/USU Conference on Small Satellites, SSC16-X-2*. [S.l.: s.n.], 2016. p. 1–12.

LEE, H. *Thermoelectrics: Design and Materials*. Wiley, 2016. ISBN 9781118848951. Available from Internet: <https://books.google.com.br/books?id=RWT_DAAAQBAJ>.

LEE, S. et al. Analysis the unsteady-state temperature distribution of micro-satellite under stabilization effects. In: HSIAO, F.-B. (Ed.). *Microsatellites as Research Tools*. Pergamon, 1999, (COSPAR Colloquia Series, v. 10). p. 324 – 332. Available from Internet: <http://www.sciencedirect.com/science/article/pii/S0964274999800419>.

LI, S.; WANG, Y.; ZHANG, H. e. a. Thermal analysis and validation of gf-4 remote sensing camera. *Journal of Thermal Science*, v. 29, n. 1, p. 992–1000, 2020.

LYLE, R.; LEACH, J.; SHUBIN, L. *Earth albedo and emitted radiation*. [S.l.], 1971.

MAHOOTI, M. *NRLMSISE00 Atmospheric Density Model*. 2010. <https://www.mathworks.com/matlabcentral/fileexchange/54673-nrlmsise00-atmospheric-density-model>. MATLAB Central File Exchange. Retrieved October 10.

MALISKA, C. *Transferência de Calor e Mecânica dos Fluidos Computacional*. [S.l.: s.n.], 2004. ISBN 978-85-216-1396.

MARCELINO, G. M. et al. A Critical Embedded System Challenge: The FloripaSat-1 Mission. *IEEE Latin America Transactions*, v. 18, n. 02, p. 249–256, feb 2020. ISSN 1548-0992. Available from Internet: <https://ieeexplore.ieee.org/document/9085277/>.

MASON, J. P. et al. Cubesat on-orbit temperature comparison to thermal-balance-tuned-model predictions. *Journal of Thermophysics and Heat Transfer*, v. 32, n. 1, p. 237–255, 2018. Available from Internet: <https://doi.org/10.2514/1.T5169>.

MCCLAIN, W.; VALLADO, D. *Fundamentals of Astrodynamics and Applications*. Springer Netherlands, 2001. (Space Technology Library). ISBN 9780792369035. Available from Internet: <https://books.google.com.br/books?id=PJLlWzMBKjkC>.

MESEGUER, J.; PÉREZ-GRANDE, I.; SANZ-ANDRÉS, A. *Spacecraft Thermal Control*. Woodhead Publishing, 2012. ISBN 978-1-84569-996-3. Available from Internet: <https://www.sciencedirect.com/book/9781845699963/spacecraft-thermal-control>.

MOUKALLED, F.; MANGANI, L.; DARWISH, M. *The Finite Volume Method in Computational Fluid Dynamics: An Advanced Introduction with OpenFOAM® and Matlab®*. [S.l.]: Springer, 2015. ISBN 978-3-319-16873-9.

NASA. *CubeSat 101: Basic Concepts and Processes for First-Time CubeSat Developers*. 2019. Acessed: 07-05-2019. Available from Internet: <https://www.nasa.gov/sites/default/files/atoms/files/nasa_csli_cubesat_101_508.pdf>.

NASA. *Definition of Two-line Element Set Coordinate System*. 2020. <https://spaceflight.nasa.gov/realdata/sightings/SSapplications/Post/JavaSSOP/SSOP_Help/tle_def.html>.

NASA. *What are SmallSats and CubeSats?* 2021. Available from Internet: <https://www.nasa.gov/content/what-are-smallsats-and-cubesats>.

OSTRUFKA, A. et al. Experimental evaluation of thermoelectric generators for nanosatellites application. *Acta Astronautica*, v. 162, p. 32 – 40, 2019. ISSN 0094-5765. Available from Internet: <http://www.sciencedirect.com/science/article/pii/S0094576519302097>.

PADGEN, M. R. et al. The ecamsat fluidic system to study antibiotic resistance in low earth orbit: Development and lessons learned from space flight. *Acta Astronautica*, v. 173, p. 449 – 459, 2020. ISSN 0094-5765. Available from Internet: <http://www.sciencedirect.com/science/article/pii/S009457652030093X>.

PAIVA, K. V. *Desenvolvimento de novas tecnologias para minitubos de calor: Análise teórica e experimental*. Tese (Doutorado) — Department of Mechanical Engineering, 2011.

PARK, D.; MIYATA, K.; NAGANO, H. Thermal design and validation of radiation detector for the chubusat-2 micro-satellite with high-thermal-conductive graphite sheets. *Acta Astronautica*, v. 136, p. 387 – 394, 2017. ISSN 0094-5765. Available from Internet: <http://www.sciencedirect.com/science/article/pii/S0094576516310645>.

PÉREZ-GRANDE, I. et al. Analytical study of the thermal behaviour and stability of a small satellite. *Applied Thermal Engineering*, v. 29, n. 11, p. 2567 – 2573, 2009. ISSN 1359-4311. Available from Internet: <http://www.sciencedirect.com/science/article/pii/S1359431108005036>.

PETERSON, G. *An introduction to heat pipes: modeling, testing, and applications*. Wiley, 1994. (Wiley series in thermal management of microelectronic & electronic systems). ISBN 9780471305125. Available from Internet: <https://books.google.com.br/books?id=-dVSAAAAMAAJ>.

PHAM, M. D. et al. Gain-scheduled extended kalman filter for nanosatellite attitude determination system. *IEEE Transactions on Aerospace and Electronic Systems*, v. 51, n. 2, p. 1017–1028, 2015.

PICONE, J. M. et al. Nrlmsise-00 empirical model of the atmosphere: Statistical comparisons and scientific issues. *Journal of Geophysical Research: Space Physics*, v. 107, n. A12, p. SIA 15–1–SIA 15–16, 2002. Available from Internet: <https://agupubs.onlinelibrary.wiley.com/doi/abs/10.1029/2002JA009430>.

POGHOSYAN, A.; GOLKAR, A. Cubesat evolution: Analyzing cubesat capabilities for conducting science missions. *Progress in Aerospace Sciences*, v. 88, p. 59 – 83, 2017. ISSN 0376-0421. Available from Internet: <http://www.sciencedirect.com/science/article/pii/S0376042116300951>.

POSIELEK, T. An energy management approach for satellites. *Proceedings of the International Astronautical Congress, IAC*, v. 2018-October, 2018. ISSN 00741795.

QIAO, L.; RIZOS, C.; DEMPSTER, A. G. Analysis and comparison of cubesat lifetime. In: CITESEER. *2013 Proceedings of the 12th Australian Space Conference*. [S.l.], 2013. p. 249–260.

RAIF, M.; WALTER, U.; BOUWMEESTER, J. Dynamic system simulation of small satellite projects. *Acta Astronautica*, v. 67, n. 9, p. 1138 – 1156, 2010. ISSN 0094-5765. Available from Internet: <http://www.sciencedirect.com/science/article/pii/S0094576510002298>.

REYES, L. A. et al. Thermal modeling of ciiiasat nanosatellite: A tool for thermal barrier coating selection. *Applied Thermal Engineering*, v. 166, p. 114651, 2020. ISSN 1359-4311. Available from Internet: <http://www.sciencedirect.com/science/article/pii/S135943111933902X>.

RICHMOND, J. *Adaptive Thermal Modeling Architecture For Small Satellite Applications*. Tese (Doutorado) — Massachusetts Institute of Technology, Dept. of Aeronautics and Astronautics, 2010.

RODRIGUEZ-SOLANO, C. J.; HUGENTOBLER, U.; STEIGENBERGER, P. Impact of albedo radiation on gps satellites. In: KENYON, S.; PACINO, M. C.; MARTI, U. (Ed.). *Geodesy for Planet Earth*. Berlin, Heidelberg: Springer Berlin Heidelberg, 2012. p. 113–119. ISBN 978-3-642-20338-1.

ROLDUGIN, D.; TESTANI, P. Spin-stabilized satellite magnetic attitude control scheme without initial detumbling. *Acta Astronautica*, v. 94, n. 1, p. 446 – 454, 2014. ISSN 0094-5765. Available from Internet: <http://www.sciencedirect.com/science/article/pii/S0094576513000234>.

ROMÁN, M. O. et al. Assessing the coupling between surface albedo derived from modis and the fraction of diffuse skylight over spatially-characterized landscapes. *Remote Sensing of Environment*, v. 114, n. 4, p. 738 – 760, 2010. ISSN 0034-4257. Available from Internet: <http://www.sciencedirect.com/science/article/pii/S0034425709003393>.

SCHAUB, H.; JUNKINS, J. *Analytical Mechanics of Space Systems*. American Institute of Aeronautics and Astronautics, Incorporated, 2014. (AIAA education series). ISBN 9781624102400. Available from Internet: <https://books.google.com.br/books?id=JD3MngEACAAJ>.

SCHOOLCRAFT, J.; KLESH, A.; WERNE, T. MarCO: Interplanetary Mission Development on a CubeSat Scale. In: *Space Operations: Contributions from the Global Community*. Cham: Springer International Publishing, 2017. p. 221–231. Available from Internet: <http://link.springer.com/10.1007/978-3-319-51941-8{_}.>

SEBASTIAN, J. T.; BABY, V. Y. Numerical investigation of thermal energy storage panel using nanoparticle enhanced phase-change material for micro satellites. In: *International Research Journal of Engineering and Technology*. [S.l.: s.n.], 2018.

SELVA, D.; KREJCI, D. A survey and assessment of the capabilities of cubesats for earth observation. *Acta Astronautica*, v. 74, p. 50 – 68, 2012. ISSN 0094-5765. Available from Internet: <http://www.sciencedirect.com/science/article/pii/S0094576511003742>.

SHUSTER, S. P. *A Survey and Performance Analysis of Orbit Propagators for LEO, GEO, and Highly Elliptical Orbits*. Dissertação (Mestrado) — Utah State University, 2017.

SLONGO, L. K. et al. Energy-driven scheduling algorithm for nanosatellite energy harvesting maximization. *Acta Astronautica*, v. 147, p. 141–151, 2018. ISSN 00945765.

SNYDER, G. J.; TOBERER, E. S. *Complex thermoelectric materials*. 2008.

SOUZA, L. J. et al. Overview of past, present and future brazilian small satellites missions. In: *IV IAA Latin America Cubesat Workshop*. [S.l.: s.n.], 2020. IAA LACW, Virtual.

SPACELAB. *FloripaSat-I: Critical Design Review*. 2017. Technical Report.

TSAI, J.-R. Overview of satellite thermal analytical model. *Journal of Spacecraft and Rockets*, v. 41, n. 1, p. 120–125, 2004. Available from Internet: <https://doi.org/10.2514/1.9273>.

VALLADO, D.; FINKLEMAN, D. A critical assessment of satellite drag and atmospheric density modeling. *Acta Astronautica*, v. 95, 02 2014.

VERSTEEG, H.; MALALASEKERA, W. *An Introduction to Computational Fluid Dynamics: The Finite Volume Method*. Pearson Education Limited, 2007. ISBN 9780131274983. Available from Internet: <https://books.google.com.br/books?id=RvBZ-UMpGzIC>.

WALTON, G. N. *Algorithms for calculating radiation view factors between plane convex polygons with obstructions*. 1986. NBSIR 86-3463.

WANG, S.; JI, S.; ZHU, Y. A comparative study of cooling schemes for laminated lithium-ion batteries. *Applied Thermal Engineering*, v. 182, p. 116040, 2021. ISSN 1359-4311. Available from Internet: <http://www.sciencedirect.com/science/article/pii/S1359431120335213>.

WOELLERT, K. et al. Cubesats: Cost-effective science and technology platforms for emerging and developing nations. *Advances in Space Research*, v. 47, n. 4, p. 663–684, 2011. ISSN 0273-1177.

XIAO, B. et al. Fault-tolerant attitude stabilization for satellites without rate sensor. *IEEE Transactions on Industrial Electronics*, v. 62, n. 11, p. 7191–7202, 2015.

XING, Y. et al. Relative position and attitude estimation for satellite formation with coupled translational and rotational dynamics. *Acta Astronautica*, v. 67, n. 3, p. 455 – 467, 2010. ISSN 0094-5765. Available from Internet: <http://www.sciencedirect.com/science/article/pii/S0094576510001190>.

YANG, X. et al. Effect of ambient dissipation condition on thermal behavior of a lithium-ion battery using a 3d multi-partition model. *Applied Thermal Engineering*, v. 178, p. 115634, 2020. ISSN 1359-4311. Available from Internet: <http://www.sciencedirect.com/science/article/pii/S1359431120331161>.

ZHENG, C. et al. Numerical investigation on the thermal performance of alpha magnetic spectrometer main radiators under the operation of international space station. *Numerical Heat Transfer, Part A: Applications*, Taylor & Francis, v. 77, n. 5, p. 538–558, 2020.

ZOHURI, B. *Heat Pipe Design and Technology: Modern Applications for Practical Thermal Management*. Springer International Publishing, 2016. ISBN 9783319298412. Available from Internet: <https://books.google.com.br/books?id=XUsWDAAAQBAJ>.

Appendix

In this section, there is a brief review about publications whose central objective was not the irradiance or thermal field of CubeSats, but in some extent, they have applied the models demonstrated in the thesis.

This paper presents an experimental study of a thermoelectric generator (TEG) for electric energy generation through temperature gradients from solar panels in CubeSats. The generation capacity is analyzed for different positioning configurations of the TEG relative to each CubeSat's surface. A preliminary version of the irradiance model is used to generate the heat flux for the thermal problem, which is solved using the commercial software Ansys/CFX. The temperature fields are the input to run the experimental setup, where the amount of power generated was measured.

E. M. Filho, L. O. Seman, C. A. Rigo, V. P. Nicolau, R. G. Ovejero, V. R. Q. Leithardt, Irradiation flux modelling for thermal–electrical simulation of CubeSats: Orbit, attitude and radiation integration, Energies 13 (2020). URL: <https://www.mdpi.com/1996-1073/13/24/6691>

E. Morsch Filho, V. Paulo Nicolau, K. V. Paiva, T. S. Possamai, A comprehensive attitude formulation with spin for numerical model of irradiance for cubesats and picosats, Applied Thermal Engineering 168 (2020) 114859, <https://doi.org/10.1016/j.applthermaleng.2019.114859>;

The influence of attitude in the heat transfer of CubeSat is addressed in this paper. The irradiance model is a previous version of the actual irradiance model of this thesis, without orbital perturbations, and the impact of the satellite's spin is assessed for attitudes of nadir, de-tumbling, high speed, arbitrary motion, and maximum exposition to the Sun, for orbits with and without an eclipse. The results showed that low spins are associated with the most significant temperature gradients due to the unequal distribution of heat fluxes. High angular speed homogenizes the temperature, especially for a spin around three axes. In general, for a high spin, temperatures are nearly constant and appropriate for typical operational temperatures. Data collect from CubeSats in orbit are compared with the numerical values, and satisfactory agreement is observed, despite differences in the designs and geometries.

C. A. Rigo, L. O. Seman, E. Camponogara, E. Morsch Filho, E. A. Bezerra, Task scheduling for optimal power management and quality-of-service assurance in CubeSats, Acta Astronautica 179 (2021) 550 – 560. URL: <https://doi.org/10.1016/j.actaastro.2020.11.016>

Despite subject to many constraints, task scheduling is ultimately restricted by the amount of power available at any given moment. In this paper, the total tasks to be executed by a satellite are constrained to the available power at any moment of the orbit. The transient power input depends on the solar cells' operation, so an analytical model estimates the irradiance field according to orbit parameters and attitude from a previous version of the thesis's actual irradiance model. Several simulations considering three satellite sizes with different orbits and task parameters are used to demonstrate the methodology's applicability.

S. Vega Martinez, E. M. Filho, L. O. Seman, E. A. Bezerra, V. P. Nicolau, R. G. Ovejero, V. R. Q. Leithardt, An integrated thermal-electrical model for simulations of battery behavior in cubesats, Applied Sciences 11(2021). URL:<https://doi.org/10.3390/app11041554>

This work presents an integrated thermal-electrical simulation model that considers the battery and photovoltaic panels' thermal and electrical effects for each instant of time, in a given orbit and attitude from a CubeSat 1U. A previous version of the actual irradiance model and the same Lumped Parameter Method presented in the thesis are used to solve the heat transfer. The irradiance also provides the input for the electrical generation of energy in the solar panels. The proposed integrated model can estimate the temperature and energy conditions of the battery. The performance of photovoltaic panels is affected by the irradiance and temperature fields along the orbit. The integrated model can take into account, for example, the battery temperature control through a heater and variations of the power profile of the Energy Power System (EPS) of the CubeSat.

Rigo, C. A.; Seman, L. O.; Camponogara, E.; Morsch Filho, E.; Bezerra, E. A.. A nanosatellite task scheduling framework to improve mission value using fuzzy constraints. Expert Systems with Applications (2021), doi:<https://doi.org/10.1016/j.eswa.2021.114784>;

Task scheduling is an effective approach to increase the value of a satellite mission, which leads to improved resource management and quality of service. This work maximizes the number of tasks performed in nanosatellite missions through a robust and realistic framework for optimal offline scheduling. The irradiance model of the thesis is used in this paper to generate the transient power input from the Two-Line Element (TLE) data of the CubeSat FloripaSat-I and Nadir's attitude. Successive orbits with eclipses are used to predict the power input generated in photovoltaic panels. The work has improved the state-of-the-art in nanosatellite scheduling by incorporating a realistic battery model and strategies for battery lifetime extension, and provides a novel methodology for multi-orbit scheduling.